UNIVERSITY OF CALIFORNIA,
IRVINE

Molecular Dynamics Studies Regarding the Role of Dibutyl Phosphoric Acid on Supramolecular Assembly in Solvent Extraction Systems

DISSERTATION

submitted in partial satisfaction of the requirements
for the degree of

DOCTOR OF PHILOSOPHY

in Materials Science and Engineering

by

Ted Young Tae Yoo

Dissertation Committee:
Professor Mikael Nilsson, Chair
Professor Elizabeth Read
Professor Craig Martens

2019

DEDICATION

O Giants of Old,
Turn not in your great slumber.
Troth, I come worthy.

TABLE OF CONTENTS

LIST OF FIGURES

LIST OF TABLES

ACKNOWLEDGMENTS

I would like to formally thank the following...

Professors Mikael Nilsson and Hung Nguyen, who have accepted me into their groups, have expressed confidence in my labors, and have provided pivotal guidance.

My qualifying and dissertation committee, whose probing questions have bettered my work.

Fellow lab members whom have endured my bombardment of questions.

The next generation of leadership for Brews and Brains at UCI, whose committed engagement have put my mind at ease.

Loh Down on Science Media Labs for allowing me to develop as a communicator.

My yoga buddies and Muay Thai sparring partners who have contributed to a spirited pursuit of physical health.

The U.S. Department of Energy, which through the Nuclear Energy University Program, NEUP contract No. NE0008288, funded this work.

Chapter 2 reprinted with permission of Springer Science+Business Media, LLC, part of Springer Nature 2018.

Chapter 3 reprinted (adapted) with permission from Yoo, T.; Nguyen, H. D.; Nilsson, M. Molecular Dynamics Investigations of Dibutyl-phosphoric Acid-Parameterization and Dimerization. The Journal of Physical Chemistry B 2018, 122, 12040-12048, PMID: 30431277. Copyright 2018 American Chemical Society.

Finally, and most importantly, my dearest friends and nihilism crew. I love you all, even though it doesn't mean anything.

CURRICULUM VITAE

Ted Young Tae Yoo

EDUCATION

Doctor of Philosophy in Materials Science and Engineering **2019**
University of California Irvine *Irvine, CA*

Bachelor of Science in Physics **2013**
California State Polytechnic University Pomona *Pomona, CA*

Associate of Arts in Culinary Arts **2009**
Le Cordon Bleu *Pasadena, CA*

RESEARCH EXPERIENCE

Graduate Research Assistant **2014–2019**
University of California, Irvine *Irvine, California*

Undergraduate Research Assistant **2012–2014**
University of California, Irvine *Irvine, California*

TEACHING EXPERIENCE

Teaching Assistant **2014–2019 intermittent**
University of California Irvine *Irvine, CA*

Adjunct Professor **2013–2014**
California State Polytechic University Pomona *Pomona, CA*

Private Tutor **2012–2014**
Greater Los Angeles Area, CA

REFEREED JOURNAL PUBLICATIONS

Molecular Dynamics Investigations of Dibutyl-phosphoric Acid—Parameterization and Dimerization. **2018**
The Journal of Physical Chemistry B, 122(50), 1214-1223.

Determinations of Dipole Moments for Liquid–Liquid Extraction Reagents **2018**
Journal of Solution Chemistry, 47(7), 12040-12048.

Site percolation on lattices with low average coordination numbers. **2014**
Journal of Statistical Mechanics: Theory and Experiment, 2014(6), P06014.

Percolation thresholds on three-dimensional lattices with three nearest neighbors. **2013**
Journal of Statistical Mechanics: Theory and Experiment, 2013(05), P05014.

PROFESSIONAL DEVELOPMENT

Vice President **2014–2019**
Brews and Brains at UCI University of California Irvine

Writer **2018–2019**
Loh Down on Science Media Lab University of California Irvine

Managing Editor **2019–2019**
Loh Down on Science Media Lab University of California Irvine

ABSTRACT OF THE DISSERTATION

Molecular Dynamics Studies Regarding the Role of Dibutyl Phosphoric Acid on Supramolecular Assembly in Solvent Extraction Systems

By

Ted Young Tae Yoo

Doctor of Philosophy in Materials Science and Engineering

University of California, Irvine, 2019

Professor Mikael Nilsson, Chair

The management of radioactive waste is an important question to answer as the necessity of carbon emissions free power generation becomes a ever more critical facet of poverty reduction. One possible remedy is to utilize solvent extraction (SX) to treat nuclear power plant waste for use reuse. Di-butyl phosphate (HDBP) is a degradation product of tri-butyl phosphate (TBP), often produced due to the acidic and radioactive conditions within many SX processes. Its formation contributes to the creation of supra-molecular structures of extraction agents even before organic phases come into contact with any metal ion. These structures are critical to the selectivity and the efficiency of solvent extraction processes. Despite their importance, much theoretical work remains to better understand the nature of these aggregates. This dissertation describes the study of HDBP and its contributing aggregate structures through molecular dynamics in order to contribute to a further theoretical knowledge of aggregation phenomenon in SX contexts.

LIST OF ABBREVIATIONS

CN	Coordination number
FF	Force field
MD	Molecular dynamics
PMF	Potential of mean force
RDF	Radial distribution function, g(r)
VDW	Van der Waals
HDBP	Dibutyl phosphoric acid
HDEHP	Bis-2-ethylhexyl phosphoric acid
TBP	Tri-butyl phosphate
DA	Hydrogen bond donor-acceptor pair
HB	Hydrogen bond; hydrogen bonded; hydrogen bonding
OPB	Out of plane bend
PDA	Pseudo-dihedral angle
OPPO	Oxygen-phosphorus-phosphous-oxygen PMF
O-O	Oxygen-oxygen PMF

Chapter 1

Introduction and Background

1.1 Future Energy Needs and Nuclear Power

1.1.1 Energy, Poverty, and Anthropogenic Climate Change

The discovery of electricity represented a tremendous technological leap forward. The versatility and efficiency of electricity has greatly empowered mankind's potential for work. It allows the construction and use of the numerous contemporary accouterments at grand scales. The consumer goods and services that hallmark advanced economies improve and lengthen lives. Electricity thus has become of necessary importance to maintaining a high standard of living.

A stable energy infrastructure is similarly critical for developing nations. This is because striving for a high standard of living is in itself an energy intensive endeavor. To this end, the United Nation's (UN) 2030 Agenda for Sustainable Development describes 17 Sustainable Development Goals[1]. Shown in Figure 1.1, the goals are designed to build up a developing nation such that it may sustainably fulfill Maslow's hierarchy of needs for her citizens. Goals 1 - 6 deal with the lower tiers of Maslow's pyramid by addressing immediate concerns around safety and entitlement systems. Goals 8 - 17 addresses the upper tiers, improving life by creating a stable and productive economy. In the middle is goal 7, which is affordable and clean energy. The placement and language of this goal is conspicuous. It pins together a nation's immediate material needs and a future of self-sustainability.[2]

But careful attention must be paid to methods of energy generation. The burning of fuels is the largest contributor of greenhouse gas emissions[3]. With atmospheric CO_2 concentrations now above 400 parts per million[4], Earth has entered an unprecedented geological era. Figure 1.2 shows ice core data dating back 800,000 years. Atmospheric CO_2 concentrations have previously never been above 300 ppm[5]. Our current era is

Figure 1.1: The 17 Sustainable Development Goals as spelled out by the UN. These goals serve as the framework to rid the world of poverty by the year 2030.

dubbed the Anthropocene, named for humankind's now permanent mark upon its native planet. The exact start of this age is still up for contentious debate. But one undeniably key characteristic of the Anthropocene is the anomalously high concentration of atmospheric CO_2 due to anthropogenic activity. It is projected that "business as usual" policies will bring concentrations up as high as 900 ppm by the 21st century's end[6]. This brings forth a myriad of problems which are directly at odds with the Sustainable Development Goals.

As of time of writing, anthropogenic climate change is already negatively impacting biodiversity. For example, by law of partial pressures, increased atmospheric CO_2 acidifies the world's oceans. This is already causing global scale collapse of coral reefs[8]. The full

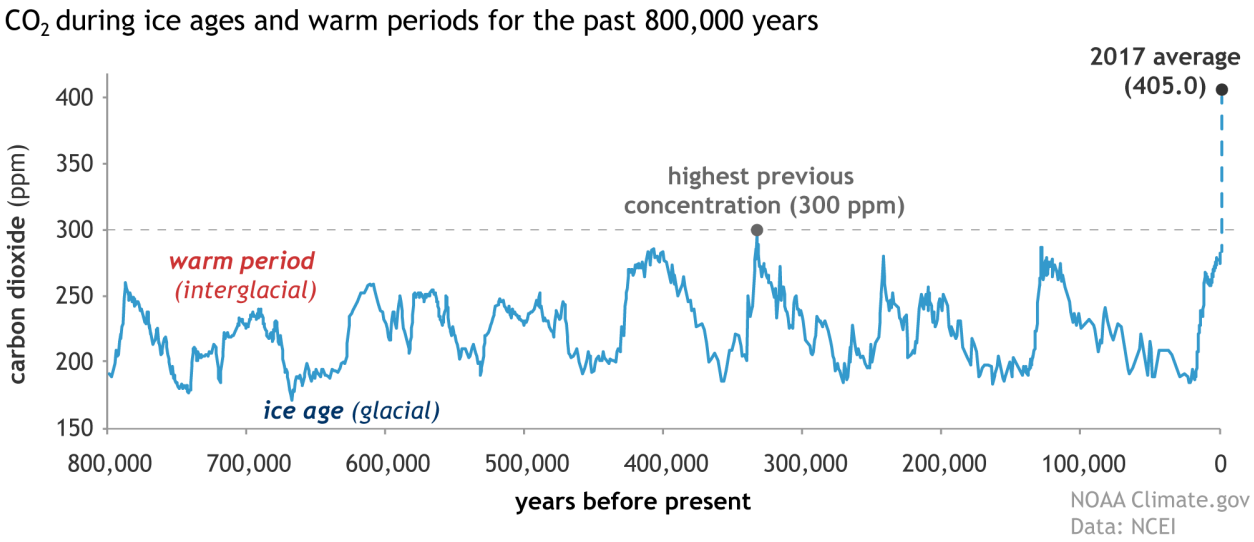

Figure 1.2: Atmospheric CO_2 concentrations determined from ice core samples.[7] Over 800,000 years of geological history, concentrations have never been higher than 300 ppm until now.

scope of this and similar effects are difficult to measure, but they are often devastating to local flora and fauna. Aside from the obvious existential peril, climate change will also negatively impact economies. This is because economic productivity relies on productive ecosystems, and diverse ecosystems are generally more productive than non-diverse ones[9, 10]. Diminishing biodiversity is therefore an issue working against sustainable development from multiple angles.

Further, incidences of extreme weather is on the rise[11, 12]. This includes prolonged drought, excessive rain, abnormally hot heat waves, and cold snaps. All of these events take a direct toll on human life. For example, a heat wave in France, August 2003 resulted in 14,802 deaths[13]. In 2018, Australia saw record breaking temperatures which resulted in 10% increase in ambulance calls, and a similar increase in mortality rate. Simultaneously, the North American continent saw record breaking lows, as it was battered by what was known as the "bomb cyclone."[14] Heating and cooling represents a particular conundrum. In the US, it accounts for nearly half of all energy consumed[15]. Increased use of such environmental control systems is expected with changing weather

patterns, creating greater energy demand. This potentially puts humanity further into a climate pitfall. This becomes especially problematic as developing nations begin to see widespread use of such systems.

Extreme weather conditions will also stress food and water resources. This sets the stage for civil strife and violent conflict[16, 17]. While it is difficult to link climate change directly to the start of any particular armed conflict, focused quantitative studies have produced reliable causal associations. To quote one such study from Hsiang et al.[18]:

> *Deviations from normal precipitation and mild temperatures systematically increase the risk of conflict, often substantially. This relationship is apparent across spatial scales ranging from a single building to the globe and at temporal scales ranging from an anomalous hour to an anomalous millennium. Our meta-analysis of studies that examine populations in the post-1950 era suggests that the magnitude of climate's influence on modern conflict is both substantial and highly statistically significant ($P < 0.001$). Each 1-SD change in climate toward warmer temperatures or more extreme rainfall increases the frequency of interpersonal violence by 4% and intergroup conflict by 14% (median estimates).*

In an increasingly globalized society, the consequences of such conflicts are rarely localized to their theaters of battle. The displacement of people, either through war, changes in local climate, or both, creates a refugee crisis. The additional demand for resources put upon the absorbing nation is itself often a source of contention. A good review of modern migration episodes through the 1900's to the present, as well as their specific environmental causes, can be found in work by Reuveny[19]. Of particular note from this study is the magnitude of displacement described, which can reach tens of millions of people.

But for those without the means of migration, people may be left in a failed state. Such people are prime targets for recruitment by armed non-state groups. And, the lack of a stable state allows for their operations to remain unmolested. Terrorist organizations such as ISIS and Boko Haram thus benefit from a fragile environment brought upon by

climate change[20]. Additionally, increasingly frequent extreme weather events hampers US military efforts to meet these threats and provide humanitarian aid. A 2019 report by the Department of Defense states that many military complexes are at direct risk due to recurrent flooding, drought, desertification, wildfires, and thawing permafrost[21].

Both the development and maintenance of high standards of living require energy. An agile energy sector which can quickly and cheaply increase capacity is therefore critical. But perhaps more so is the pollutants released along the way. Pollutants that actively work against our quest for improvement. With careful consideration, it is possible to increase human prosperity without jeopardizing our own safety and survival.

1.1.2 The Role and Impacts of Nuclear Power

Nuclear power is the largest source of non-CO_2 emitting energy. Widespread implementation could make a positive impact towards a sustainable energy strategy. The abundance of fuel and the round the clock operation of a nuclear power plant simplifies the task of increasing power grid capacity[22]. However, public entities world wide have labored to increase the political capital necessary for widespread adoption of nuclear power. One such concern revolves around safety, both of the plant itself and of its waste products.

Opinions of safety are often derived from the most recent high profile incident, more so than existing evidence. Despite this, such evidence will be provided in Table 1.1. This table describes the death-print of various energy generation methods[23]. This data is cumulative from the earliest records to 2016. Death toll estimates are based on known toxicities of pollutants and their released concentrations from corresponding generation methods. It also factors in direct deaths caused accidents. It is seen that nuclear energy has the lowest human cost out of any other type of power plant. This is despite the inclusion

of cancer related deaths due to inadvertent release of radioactive material and factoring in all of history's high profile nuclear accidents.

energy source	deaths per trillion kWh	% electricity generated	% energy generated
coal	100,000	41	
oil	36,000	4	33
bio-fuel/biomass	24,000	2	21
natural gas	4,000	22	
hydro	1,400	16	
solar	440	1	
wind	150	2	
nuclear	90	11	

Table 1.1: 2016 energy death-print

The lack of deaths per energy unit can be attributed to two things, high energy density and the fact that waste products can be stored. In comparison, fossil fuel burning generators vent their waste into the atmosphere. Along with greenhouse gas emissions, this means sulfur dioxide, nitrogen oxides, hazardous particulate matter, and heavy metals. For example, effluent fly ash, a result of burning coal, releases various radionuclides which have otherwise been locked away in the earth. The emitted radiation is greater than that of radioactive waste stored in casks, and is far less contained[24]. While modern scrubbers can greatly reduce the release of pollutants, their widespread usage can only be assured in developed nations with strong regulations[23]. Developing nations which lack the political capital required to enforce the use of scrubbers in coal plants are often also dependent on fossil fuels for their energy needs. The pollution caused by this particular irony is responsible for around 19,880 excess deaths per year in Southeast Asia[25]. Altogether, historical estimates suggest 1.84 million air pollution deaths have been prevented since the adoption of nuclear power[26].

While it is worth taking the time to point out human foibles such that one may better understand themselves, this work is interested in technological solutions behind the production of high level radioactive waste. Produced waste from nuclear power

plants is another barrier to the widespread adoption of nuclear power. The United States alone possesses 90,000 metric tons of waste awaiting disposal[27]. Currently, there is no consensus on where this waste is to be stored. Nuclear power plant waste is toxic and radioactive. This complicates the endeavor of finding a resting point for this waste.

Advanced nuclear fuel cycles can directly address this issue. Recycling spent fuel greatly increases uranium economy and reduces the volume of high level waste. Solvent extraction (SX) is a common and scalable process for reclaiming uranium from used fuel to incorporate it and reuse it in mixed oxide fuel (MOX)[28]. While the exact composition of spent fuel will vary based on reactor design, the vast majority of waste is yet unburned uranium. As seen in Figure 1.3, roughly 96% of the volume of waste can be recycled.

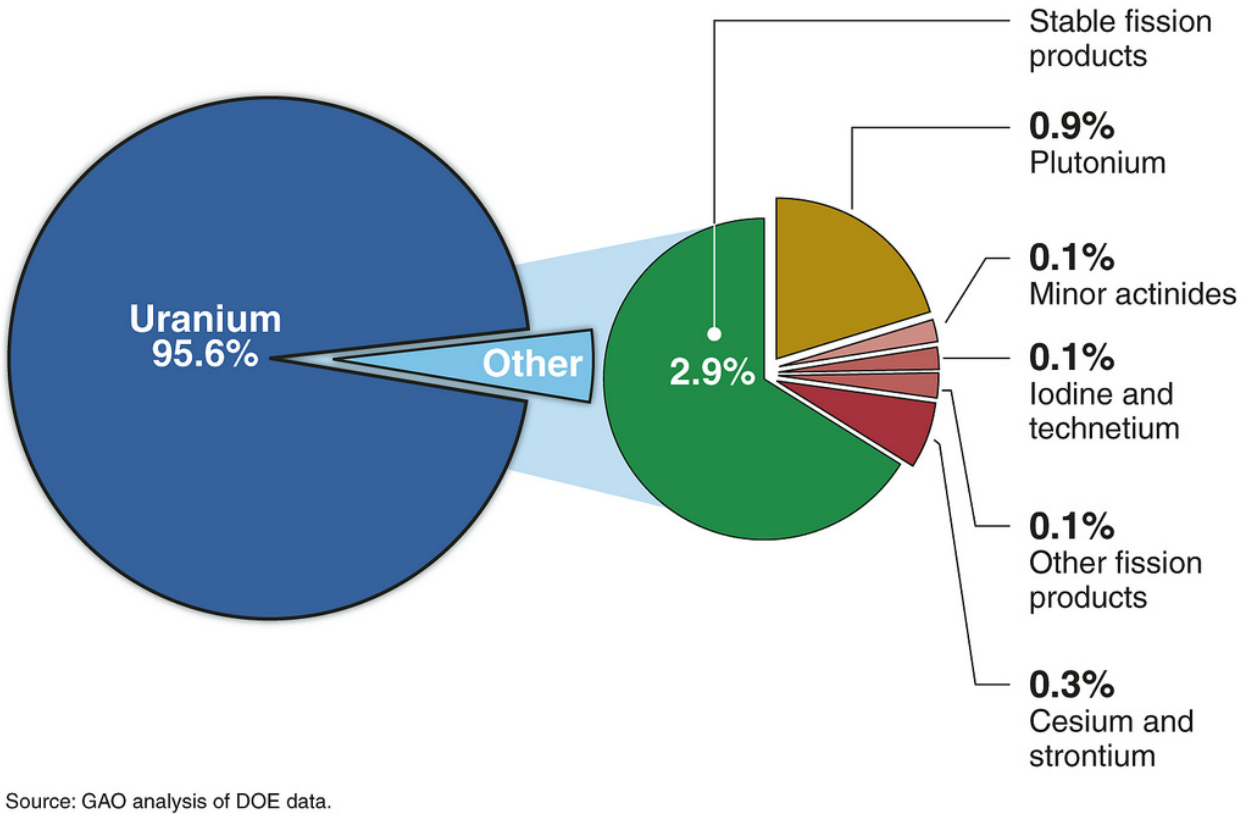

Figure 1.3: The typical composition of spent nuclear fuel after 10 years of cooling.[29]

However promising it may be, it is currently estimated that reprocessing spent fuel will be 25% more expensive than letting waste exist in limbo[29]. Cost may potentially be

remedied with the advent of new technologies. But new developments are predicated on the new discoveries that lead to them. Therefore, this dissertation will discuss experiments and molecular dynamics (MD) simulations that have been performed to better understand chemistries behind SX.

1.2 Theoretical Background

1.2.1 Overview of Solvent Extraction

The other names of SX are liquid-liquid extraction and partitioning. It is a method of separating materials by means of exploiting its relative solubilities in two immiscible phases[30]. These two phases are the organic and aqueous. Typically, transfer of one or more species of materials go from the aqueous to the organic. The phases are vigorously mixed together, bringing the extracting agents in the organic phase into contact with target compound in the other phase. The ligands then bind electrostatically in a reaction that is driven by free energy. The solution is then left to settle and the organic phase separates from the aqueous, bringing along with it its bound material.

The organic phase consists of an aliphatic compound, which is the extractant, in a non-polar diluent. Typical processes will use kerosene, which is an inert hydrocarbon that is cheaply derived from refined petroleum. However, dodecane is often preferred in a laboratory setting, owed to its ease of purification of low cost. The aqueous phase contains the target compounds to be separated, which has been dissolved in an acidic solution, usually highly concentrated nitric acid.

The gold standard for the reprocessing of nuclear fuel is the PUREX process[31]. It utilizes the extractant is tri-butyl phosphate (TBP), which is known to be selective for

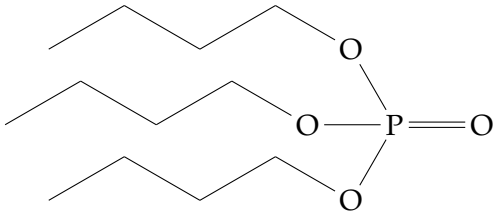

Figure 1.4: The schematic diagram of TBP which is most notably used in the PUREX process.

tetravalent and hexavalent metal cations. A diagram of TBP is shown in Figure 1.4. However, because of the highly acidic and radioactive environment within the process, TBP can undergo degradation into an acidic substance. A common degradation product is dibutyl phopshate (HDBP)[32]. This chemical much less selective than TBP, and will coextract many elements other than the desired target.

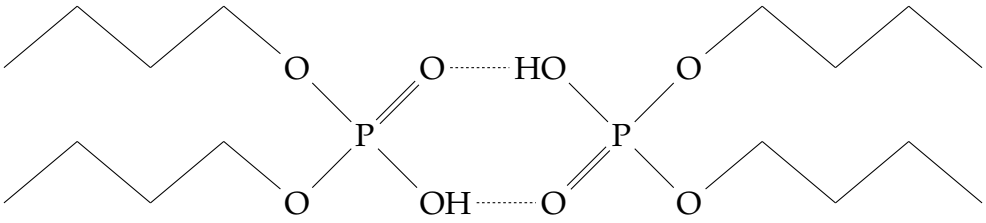

Figure 1.5: The schematic diagram of two HDBP molecules in the head-to-tail conformation. The acidic phosphate head forms two hydrogen bonds, creating an 8-membered ring between them.

1.2.2 Effects of Supra-molecular Assembly

In addition to metal-ligand complexes, the ligands themselves form ordered structures. For example, acidic organo-phosphates, such as HDBP, are known to strongly associate via hydrogen bonding[33, 34, 35]. Mono-acidic organophosphates will dimerize by orienting their polar heads to face each other[36]. The resulting structure is held together by two hydrogen bonds (HB) that form an 8-membered ring[33]. This is made possible as each phosphate possesses both donor and acceptor atoms at it's polar head. Current literature suggests that HDBP in dilute solutions with non-polar organic solvent

will predominantly exist in this conformation. A schematic representation of this can be seen in Figure 1.5.

Under certain conditions, acidic chemical species may aggregate and contribute to a larger structural hierarchy.[37, 38, 39, 40, 41]. These structures range from the small aforementioned dimers, to larger scale aggregates. A representation of scale can be found in Figure 1.6. Under particular conditions, such as excessive particulates in the feed stock, an undesirable third phase may be formed. Such large aggregates cause process disruptions and even potential criticality events as fissile materials begin to concentrate within the third phase[42, 43, 44, 45, 46].

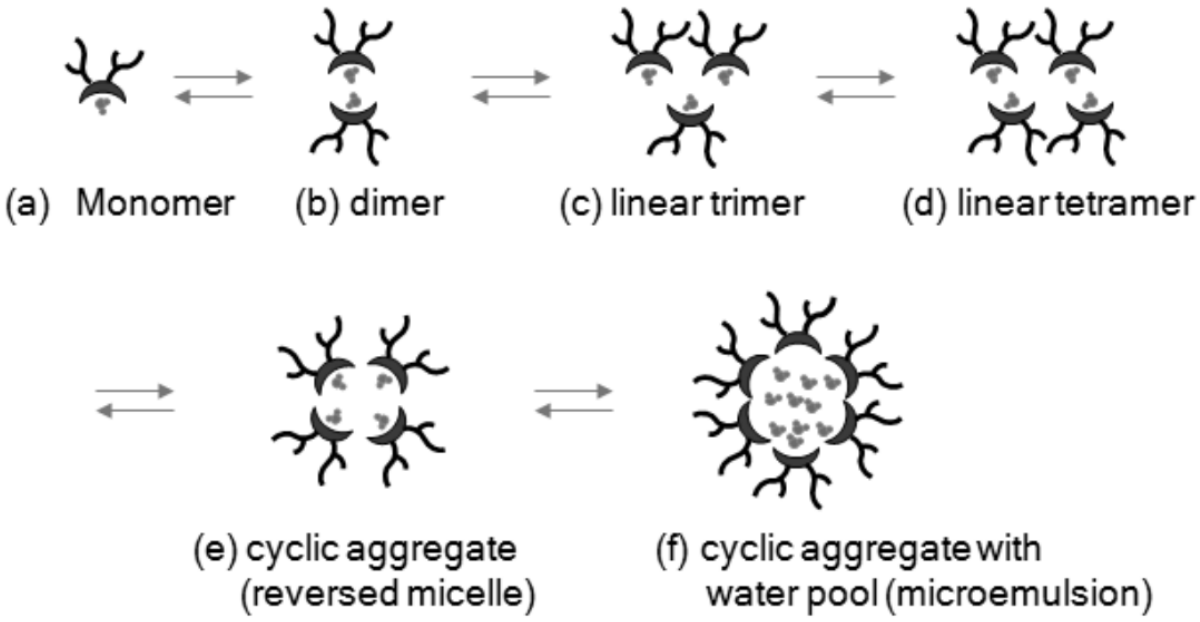

Figure 1.6: A representative diagram of the structural hierarchy of aggregates. Figure adapted from[47].

How these aggregates grow and how they effect extraction is still an area which needs extensive study[47]. What is known is that these hydrogen bonded aggregates are important to extraction. For example it is known that bis-2-ethylhexyl phosphoric acid (HDEHP), which is another degradation product of TBP, is selective to different first row transition metals based on temperature[39]. This is said to be due to the differ-

ent oligomeric structures in the organic phase. Such complexes are sensitive to metal concentration and temperature[48].

For these aggregates to coordinate to a metal ion, they must first break their hydrogen bonds[36]. This allows for the ligand to deprotonate and neutralize the charge of the metal-ligand complex. Weakening the hydrogen bond energy can make for a stronger extractant. E.g. di-alkyl phosphinates are less efficient extracting agents compared to di-alkyl phosphates. The added oxygens draw electrons away from the acceptor oxygen and weakens the hydrogen bond, which in turn makes it easer to break.[47]

Despite this initial energy barrier, these hydrogen bonded structures play a crucial role in extraction. Further weakening of hydrogen bond interactions by adding thiols results in monomers dominating the organic phase[49]. The addition of a depolymerizing agent resulted in a four order of magnitude decrease in the extraction of trivalent lanthanides using HDEHP.[50]

1.2.3 Molecular Dynamics Studies

While experimental data can show the effects of aggregation, direct probes into how they assemble can be difficult. In such cases, molecular dynamics (MD) is a useful tool for studying the molecular level drivers behind aggregate formation. This is because real-space data of atoms is readily available, it being stored in memory. Such a luxury is available only to crystallographers working in systems exhibiting greater order than liquids. Access to position and velocity can potentially give direct vision into the machinations behind phenomenon such as aggregation.

It does however come at a cost. The accuracy of MD models have to be heavily validated and cross referenced with existing experimental data. *In silica* observations must

match that of *in vitro* with a high degree of confidence in order to readily take advantage of the predictive ability simulations provide. The usefulness of the combination of simulation and experiment has been demonstrated in many previous works regarding TBP[51, 52, 53]. Such works have been able to determine the various aggregate species of TBP in a non-polar solvent. By rigorously matching simulation behavior with experimental data, simulation can describe with a high level of confidence molecular behaviors which would otherwise be impossible to see experimentally.

Despite the fact that HDBP is heavily implicated in the assembly of supra-molecular structures, it has received far less attention than TBP. This may be due to the fact that the acidic head creates complications in, not only its behavior, but the development of a reliable model as well. Further, existing computational studies of HDBP and similar compounds typically center around its coordination with metals[54], or its behavior post contact with a non-metal loaded aqueous phase[55]. This may perhaps be due to studies focusing on supra-molecular structures on their own, which do not occur without the aid of water or nitric acid[56]. It is possible that study of HDBP itself may provide insights into the role aggregation plays in SX.

1.3 Overview of Scope

This dissertation will describe molecular dynamics studies on the aggregation behavior of HDBP via hydrogen bonding. The purpose is to better understand the particular role HDBP plays in the formation of supra-molecular assemblies. This will be accomplished by simulating dry HDBP containing organic phases. Examinations described here will first focus on the necessary groundwork to perform such studies. Then, attention will be on the molecular structures that precede contact with an aqueous phase.

1.3.1 Determination of Dipole Moments

Chapter 2 describes work on an apparatus to quickly and cheaply determine dipole moments of extractants. Values for dipole moments of many extractants do not exist, but are necessary for the refinement of accurate force fields. Thus, a liquid capacitance cell was designed. Using Debye's relations, dipole moments of HDBP and octyl(phenyl)-N,N-diisobutylcarbamoylmethylphosphine oxide were measured for the first time. Further, these values have been compared to that calculated by DFT. Good agreement was found.

1.3.2 Parameterization and Examination of HDBP Dimers

Chapter 3 describes the process of refining the FF for HDBP. Default General Amber Force Field (GAFF) parameters was used as a starting point. This new FF better represents the real life behavior of HDBP by more closely matching several critical properties. The refinements are described. Further, a PMF study was undertaken to characterize the head-to-tail cyclic dimer, which is understood to be a meta-stable conformation. This PMF was then used to quantify HB distance and angle cutoffs, which is an important determination for qualifying HB aggregates.

1.3.3 Behavior of HDBP in Non-polar Solvent

With the new FF in hand, Chapter 4 discusses the behavior of HDBP in solution as observed through MD simulations. A PMF study was undertaken in order to better understand the role of hydrogen bonds on the aggregation of HDBP. This is a compliment to the PMF study mentioned in Chapter 3. Further, HDBP was simulated in a non-polar solvent in a range of concentrations. These solutions can be considered to be the dry pre-aqueous contact organic phase. The hierarchy of aggregate structures was obtained.

The distribution of aggregate sizes was quantified, and calculated as a function of free energy.

1.3.4 Phase Transitions in HDBP

Finally, Chapter 5 describes the behavior of HDBP in low concentrations. By examining distribution of aggregate species, network topology of hydrogen bonded structure, and calculating diffusion, interesting behavior has emerged. What could be described as a phase transition brought upon by changes in concentration have been observed.

Chapter 2

Determination of Dipole Moments

2.1 Introduction

2.1.1 Background

The dipole moment of a molecule is an important property that provides telling structural information regarding the short-range order emerging from non-bonded interactions with neighboring species [57]. The electric field of a molecule often becomes perturbed by the external field applied by neighboring molecules. These dipole–dipole interactions can then cause the formation of ordered structures which can affect both kinetics and thermodynamics of all molecular species in solution. For this reason, the dipole moment is often a critical parameter that is important for the development of semi-empirical models[58, 59].

In solvent extraction (SX) systems, ordered structures exist across a hierarchy of sizes. They range from simple binary aggregates, to reverse micelles, or even third-phase formation, where a stable emulsion appears in a layer between the organic and aqueous phase. This undesirable third phase often causes process upsets and possible criticality events in the case of nuclear fuel treatment[42, 43, 44, 45, 46]. The transition from small to larger aggregates may have an effect on the selectivity, synergism, and efficiency of metal ion extraction[47]. Even though aggregate formation is prevalent in a multitude of SX systems, a detailed understanding of their effect on extraction has yet to be realized. It is likely that physicochemical properties of the phases, where dipole moments play a critical role, are important for understanding SX systems.

Dipole moment is also a critical factor in the proper development of molecular dynamics force fields[60]. Successful simulation of any system depends on the accurate representation of the physico-chemical properties of all involved molecular species. Hence, a molecule whose dipole moment matches known experimental values allows

for direct comparison between in silica and in vitro experiments. Other properties that are often considered include density and heat of vaporization[61]. Once the force field parameters are established, more elaborate simulations are allowed to predict observable effects such as the formation of aggregates and metal ion extraction.

Dipole moments are typically measured using dielectric spectroscopy[62, 63]. However, the cost of these instruments may be a barrier to certain research groups engaged in model development. Other methods for determining dipole moments include measurements of solvatochromic shifts[64], useful for molecules that exhibit suitable spectroscopic properties. A thorough understanding of the frequency response of the relative permittivity of a material may not be necessary for the development of accurate molecular dynamics models. Thus, a simple "no-frills" solution that allows for quick and precise measurements of the dipole moment would be preferred in these cases. For example, Gilani et al. used a cylindrical dielectric cell coupled with a digibridge to estimate the dipole moment of various compounds [65, 66].

In this work, a liquid capacitance cell (LCC) was developed, allowing for the measurements of the relative permittivity of solutions of low polarity. This measurement is key in the calculation of the dipole moment of a polar solute dissolved, at low concentration, in a non-polar solvent. The LCC was designed and machined in house, and is of considerably less cost than a dedicated instrument while its accuracy is on par with that of commercial devices.

The construction of the LCC will be discussed and the dipole moments of one organic diluent and three common liquid–liquid extraction reagents are presented. These chemical compounds are 1-octanol, tributyl phosphate (TBP), dibutyl phosphoric acid (HDBP), and octyl(phenyl)-N,N-diisobutylcarbamoylmethylphosphine oxide (CMPO) as shown in Figure 2.1. In addition, the dipole moments of these substances have been predicted using density functional theory (DFT), and their values are reported for comparison.

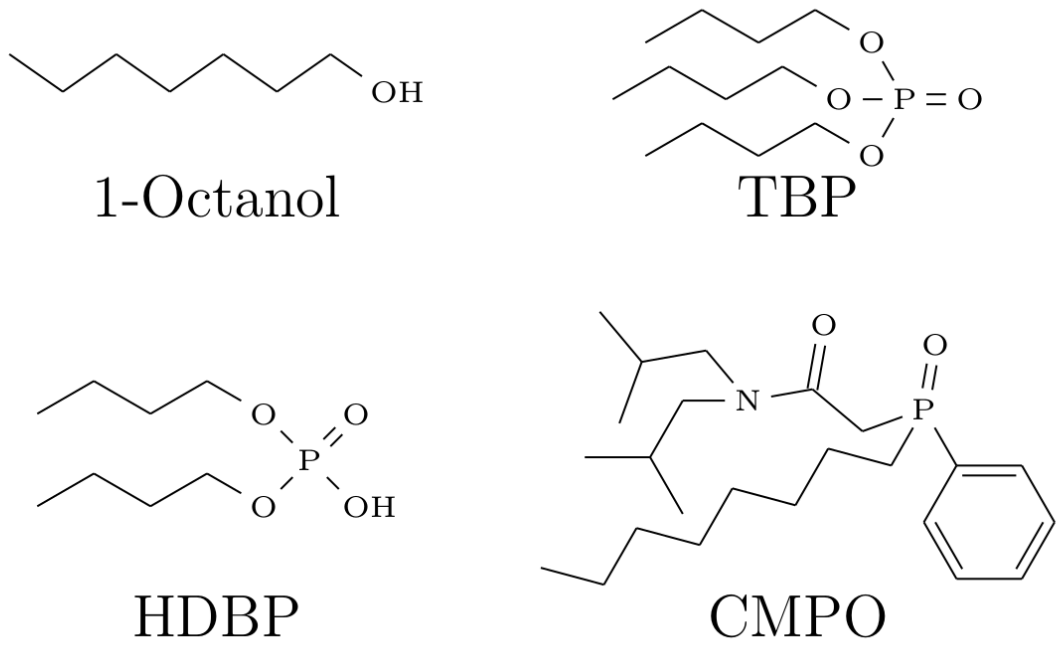

Figure 2.1: The chemical structures of the substances studied in this work; 1-octanol and TBP were used for verification purposes.

2.1.2 Theoretical Basis

In theories laid out by Debye, the case of dilute solutions of polar molecules in a non-polar solvent was considered[57]. According to these theories, the dielectric constant and index of refraction of the solution is related to the dipole moment of a polar solute. Guggenheim reformulated and simplified Debye's equations, as shown in Equation2.1[67]:

$$\left(\frac{\epsilon - 1}{\epsilon + 2} - \frac{n^2 - 1}{n^2 + 2}\right) = \frac{4\pi N_A \mu^2}{9kT} C \tag{2.1}$$

where ϵ, is the relative permittivity; n, the index of refraction; N_A, Avogadro's number; k,

Boltzmann constant; T, temperature in Kelvin; μ, dipole moment; and C, the concentration. Guggenheim showed that the left-hand side of the equation is linearly related to the concentration[67]. The dipole moment can be determined from the slope by factoring out the known constants. In the remainder of the manuscript, the left side of Equation 2.1 will be referred to as the relative difference between dielectric constant and index of refraction.

The procedure for using this relation is spelled out in the work by Janini et al.[68] based on the theoretical explanations by Buckingham[69]. In short, a series of dilute solutions are prepared, then the index of refraction and relative permittivity are measured as a function of the concentration. For the study presented in this manuscript, the in-house LCC was used to determine values for the relative permittivity.

As long as the solutions are not conductive, the relative permittivity is easily measured by probing its dielectric properties. A substance sandwiched between the electrodes of a capacitor will cause the total capacitance to increase. The ratio of this increase over vacuum is the dielectric constant:

$$\epsilon = \frac{C_x}{C_0} \tag{2.2}$$

where C_x is the capacitance with the dielectric, and C_0 the capacitance with air as the dielectric. Strictly speaking, C_0 represents permittivity of vacuum. The small difference between the dielectric constant of the two media (air vs. vacuum) is not relevant in most practical applications, this work included. The idea behind measuring dielectric constant is simple: take a parallel plate capacitor, fill the cavity between with liquid, and then measure the new capacitance.

2.1.3 Design of the Liquid Capacitance Cell

The LCC is pictured in Figure 2.2. It consists of a straightforward construction of three concentric tubes made of stainless steel. The tubes of largest and smallest diameter were aligned to a common axis and welded onto a plate. This is the base of the cell and serves the dual purpose of both liquid-containing vessel and electrode. The middle diameter tube slides between inner walls of the base and acts as the second electrode. A lip was welded to this tube in order to prevent it from falling completely into the space between the base and thus avoids contact with the base plate. A spacer made from poly-ether-ether-ketone (PEEK), a known insulator that possesses non-reactive properties, keeps the two constructions electrically isolated. Small dowels on each piece allows for alligator clips to easily attach to the electrodes. Finally, the assembled LCC was placed in a Faraday cage made from steel wire mesh (chicken wire) to reduce noise in the measurements. However, it was found that the Faraday cage was not strictly necessary.

There were three considerations when choosing the dimensions of the cell: maximizing the dry capacitance, minimizing the volume, and availability of materials. A larger capacitance will always be preferable since the sensitivity to changing relative permittivity increases linearly with dry cell capacitance. The Tenma 72-8150 multimeter, used in this study, possesses an accuracy of ±0.5% in the capacitance range relevant for this work. Hence, a base capacitance of 200 pF or more for the LCC would provide an instrumental accuracy of approximately 1 pF of the dry cell capacitance. This should allow small changes in capacitance to be discerned.

The most straightforward way to increase capacitance is to increase the surface area of the cell. However, this would increase the total volume of the cell, resulting in an increase in the amount of sample necessary for the measurement. Decreasing the separation between the two electrodes is not practical either. It is possible that a sufficiently high

Figure 2.2: The liquid capacitance cell is shown disassembled. Fluid is held within the cylindrical shell to the left. The middle cylindrical piece slides between the gap of the shell, making a capacitor. The two metal parts are all solid constructions. The PEEK spacer is shown to the right

concentration of polar molecules may cause a short circuit. This may happen more easily if the separation is small, or if the solute is highly polar. Given that the solutions should be of low concentration, this should generally not be a problem.

Finally, by using tubes of existing industry standard dimensions the construction cost was significantly reduced. However, the final design for the LCC has roughly a 50% greater plate separation than originally planned. Milling new tubes of non-standard sizes would have increased the cost by an order of magnitude.

The end product was determined to have a dry capacitance of 219 ± 2 pF and a

sample volume of 56 ± 1 mL, based on repeat measurements. The base of the LCC is 100 mm in height, has an inner diameter of 47.5 mm, and an outer diameter of 63.5 mm. The second electrode has an inner diameter of 53.5 mm. The outer most pipe of the base electrode has a wall width of 1.75 mm and the other pipes are 1.5 mm thick. CAD files can be provided by request to the authors. All metal surfaces were cleaned with an ethanol wash and sonicated, both before and after welding. After each use, the cell was cleaned with ethanol and air dried.

2.2 Experimental Methods

2.2.1 Chemicals Used and Sample Preparation

TBP, HDBP, and 1-octanol were purchased from Sigma-Aldrich at 99, 98, and 98% purity respectively. CMPO was purchased at > 95% purity from Marshallton Labs. The solvents were anhydrous grade octane or dodecane, purchased from Sigma-Aldrich. All substances were used without further purification.

For each tested substance, a number of solutions (100 mL each) of increasing concentration of a reagent in a solvent were prepared using volumetric flasks. Solutions of 1-octanol dissolved in n-octane were prepared as a validation standard with known dipole moment[70, 71]. TBP was included as a second validation, as the dipole moment has been previously reported[70, 72, 73]. Solutions were prepared be weighing out a suitable amount using an analytical balance (Mettler Toledo XS105d) and diluting them to 100 mL using a volumetric flask (±0.08 mL accuracy).

2.2.2 Analysis of Samples

Part of each prepared solution was transferred to the assembled capacitance cell. The slit in the lip of the middle ring allows for the solution to be introduced into the cell and for the liquid level to be controlled. The multi-meter was connected to the metal dowels on each electrode of the LCC via alligator clips. Modern off-the-shelf multi-meters are precise enough for the purposes of this study[74]. A Tenma 72-8150 multimeter was used for this study and the measurement drift was corrected by re-zeroing the device after each measurement.

An aliquot of each solution was taken for measurements of the refractive index using an Abbe-3L refractometer (Milton Roy Company) with an accuracy of ±0.0001. This device is a bench-top two prism refractometer equipped with a tungsten lamp. Calibration was performed using the manufacturer's supplied standards. A thermometer built into the prism assembly was used to determine the measurement temperature.

All reported values are the averages of four measurements. The temperature was not controlled, either for the LCC or the refractometer. However, all measurements were taken in the same room where the temperature was measured and maintained at $20 \pm 1^{\circ}$ C.

2.2.3 Computational Methods

DFT calculations utilized Gaussian09[75] on a local computing cluster. The dipole moment was found by optimizing molecular geometries using the 6-31G* basis set. A single molecule was optimized in vacuum, which closely represents conditions in an ideal gas phase. The initial molecular structures were generated using a SMILES string translator[76]. Structures were then piped into the molecular dynamics software package AMBER14[77] for a preliminary round of energy minimization. This structure was then

optimized using Gaussian09 until convergence to a solution. Finally, the vibrational modes were calculated. All final structures were found to have real vibrational modes, signifying that a satisfactory solution for the molecular geometry has been reached. Only one molecular conformation was analyzed in this way.

2.3 Results and Discussion

Data collected using the LLC and the refractometer, and calculated using Equation 2.1, are shown below in Table 2.1. The uncertainties for the concentrations are estimated based on the accuracy of the balance and the volumetric glassware used in the lab. The uncertainties for the conductivity and refractive index are based on four repeat measurements or the accuracy of the instrument, whichever is larger. The uncertainties in the dielectric constant were determined by standard error propagation techniques.

It is shown in Figure 2.3 that the relative difference between dielectric constant and index of refraction (the left-hand side of Equation 2.1) is linearly proportional to the concentration of the reagents as predicted by Debye's theory. 1-Octanol and TBP were used for validation purposes and are plotted based on the data from Table 2.1 in the top panels in Figure 2.3. The bottom two panels in Figure 2.3 show plots of the concentration of HDBP and CMPO in n-dodecane versus the left-hand side of Equation 2.1. Again, the points are well represented by a linear fit.

Based on the plots in Figure 2.3 it is clear that all tested concentrations stay within the linear domain, circumventing any breakdown in Guggenheim's relation. The dipole moments were calculated from the slopes of the fitted lines in Figure 2.3, by using the right-hand side of Equation 2.1 The calculated dipole moments for 1-octanol and TBP are shown in Table 2.2 along with their literature values[70, 71, 72, 73].

Concentration (mol/m^3) (±0.1%)	C_x (pF)	ϵ	n (±0.00005)
	1-octanol		
93.14	426 ± 3	1.95 ± 0.03	1.3979
13.61	428 ± 2	1.95 ± 0.02	1.3981
21.78	435 ± 2	1.99 ± 0.02	1.3983
28.02	439 ± 2	2.00 ± 0.02	1.3985
	TBP		
36.6	431 ± 2	1.97 ± 0.02	1.3886
53.9	436 ± 2	1.99 ± 0.02	1.3887
72.8	439 ± 2	2.00 ± 0.02	1.3888
109.7	450 ± 2	2.05 ± 0.02	1.3892
	HDBP		
48.5	412 ± 2	1.88 ± 0.02	1.3886
74.1	416 ± 2	1.90 ± 0.02	1.3887
98.6	419 ± 3	1.91 ± 0.03	1.3887
145.7	429 ± 2	1.96 ± 0.02	1.3892
186.8	434 ± 2	1.98 ± 0.02	1.3895
	CMPO		
6.22	425 ± 2	1.94 ± 0.02	1.3887
12.33	428 ± 2	1.95 ± 0.02	1.3891
18.44	432 ± 2	1.97 ± 0.02	1.3896
24.32	435 ± 2	1.99 ± 0.02	1.3897
31.29	438 ± 2	2.00 ± 0.02	1.3901

Table 2.1: Experimentally determined measurements

Substance	Experimental Dipole moment (D)	Literature	DFT
1-octanol	1.71 ± 0.04	1.60-1.80 [70]	2.03
	1.72 ± 0.02	1.649 [71]	
TBP	3.21 ± 0.03	3.05-3.35 [70]	3.39
		3.28-3.32 [72]	
		3.32 [73]	
HDBP	2.62 ± 0.07		2.62
CMPO	4.56 ± 0.10		4.36

Table 2.2: Experimentally determined dipole moments at 20 ± 1 ° C, comparative literature values and values calculated by DFT.

The measurements of 1-octanol and TBP provide dipole moment values that fall within accepted literature values, indicating that the precision of this setup with the

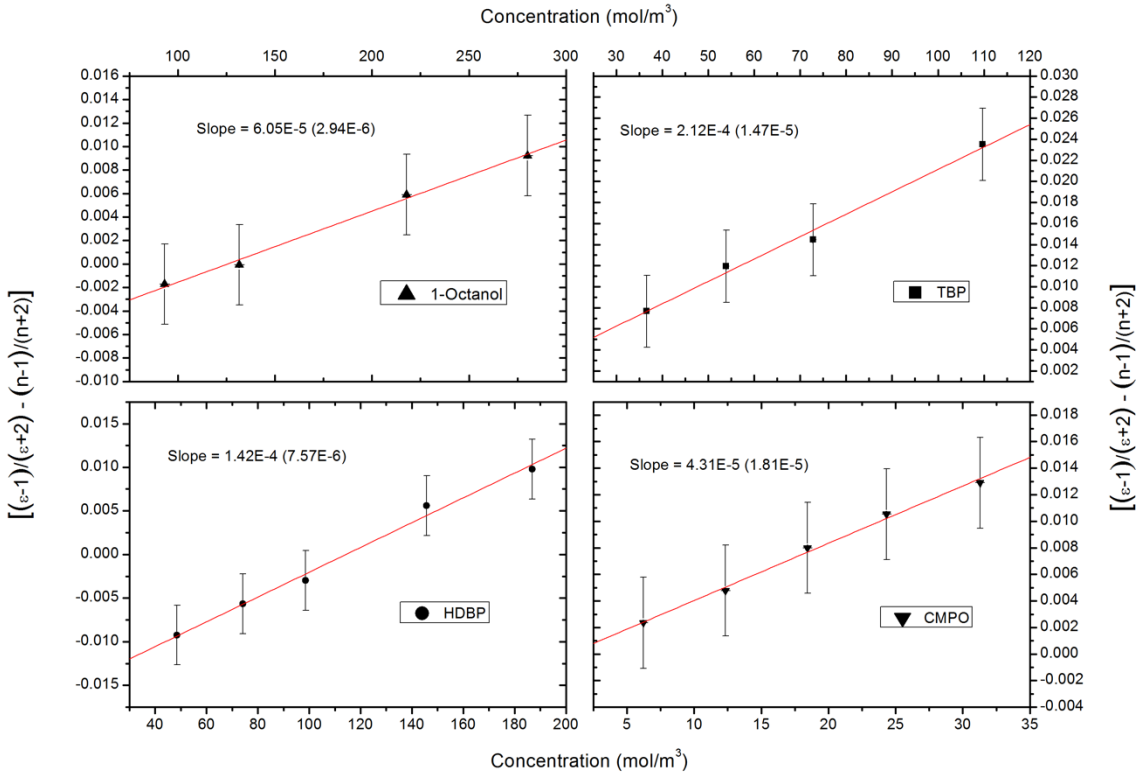

Figure 2.3: Linear relationship described by Equation 2.1 and used to calculate the dipole moment. The slopes for the fitted lines are included and the uncertainties of the slopes are shown in parenthesis. Each data-point is the average of four separate measurements. Note that the concentrations are given in mol$*m^{-3}$ to simplify for SI units to be used in the subsequent calculations

LCC and the multi-meter is adequate. The dipole moments for HDBP and CMPO were determined as 2.62 and 4.56 D, respectively, with errors between 2 and 3%.

Based on the measurements, CMPO has the highest dipole moment, followed by TBP and HDBP, and 1-octanol having the lowest value. The permanent dipole moment of a molecule is based on the uneven spatial distribution of electronic charges across the molecule. It is not surprising that CMPO displays the largest dipole moment considering the unsymmetrical nature of the molecule, see Figure 2.1. The difference between HDBP and TBP may be explained by the orientation of the hydrocarbon chains. For HDBP, the two chains may extend in opposite directions increasing the symmetry of the molecule, as

compared to TBP having three chains. The 1-octanol, while unsymmetrical, is the smallest molecule with only one oxygen atom as the electronegative contributor.

The values from the DFT calculations are shown in Table 2.2 and provide a similar trend as the experimental values with 1-octanol as the lowest and CMPO having the highest value. The DFT calculations were done with the primary purpose to provide a set of values from a single technique to compare the trend in the dipole moment across the different substances. The values found by DFT were not intended to be used as a direct comparison with experimental or literature values. However, a plot based on the limited amount of data presented here for measured versus calculated (by DFT) dipole moments, see Figure 2.4, show a reasonable trend.

It is possible that differences between the values measured from the LCC and from DFT may be attributed to experimental errors and conformation sampling. Inclusion of additional substances would provide a better trend and indicate the source of the discrepancy between calculated and experimental data. While experimental errors might be reduced by higher quality instruments, the individual errors in the experimental values are reasonable and our values are within known dipole moment values. The DFT calculations appear to overestimate low values and underestimate high values, causing a slope of < 1 and a cutoff well above 0, as seen in Figure 2.4.

The ab initio calculations may be improved by sampling multiple conformations and performing an ensemble average. In the most ideal case, gas phase conformations will be representative of the average behavior of the molecule in a solvent[57]. In practice, this will not be true, and molecules should be expected to deviate from ideality by varying degrees. Particularly, for the case of 1-octanol, this amphiphile's ability to form hydrogen bonds complicates its behavior in solution[78]. Multiple samplings of conformations may address this somewhat. However, there are no standard methods for this as these ab initio calculations rely on some assumption regarding favorable and realistic conformations.

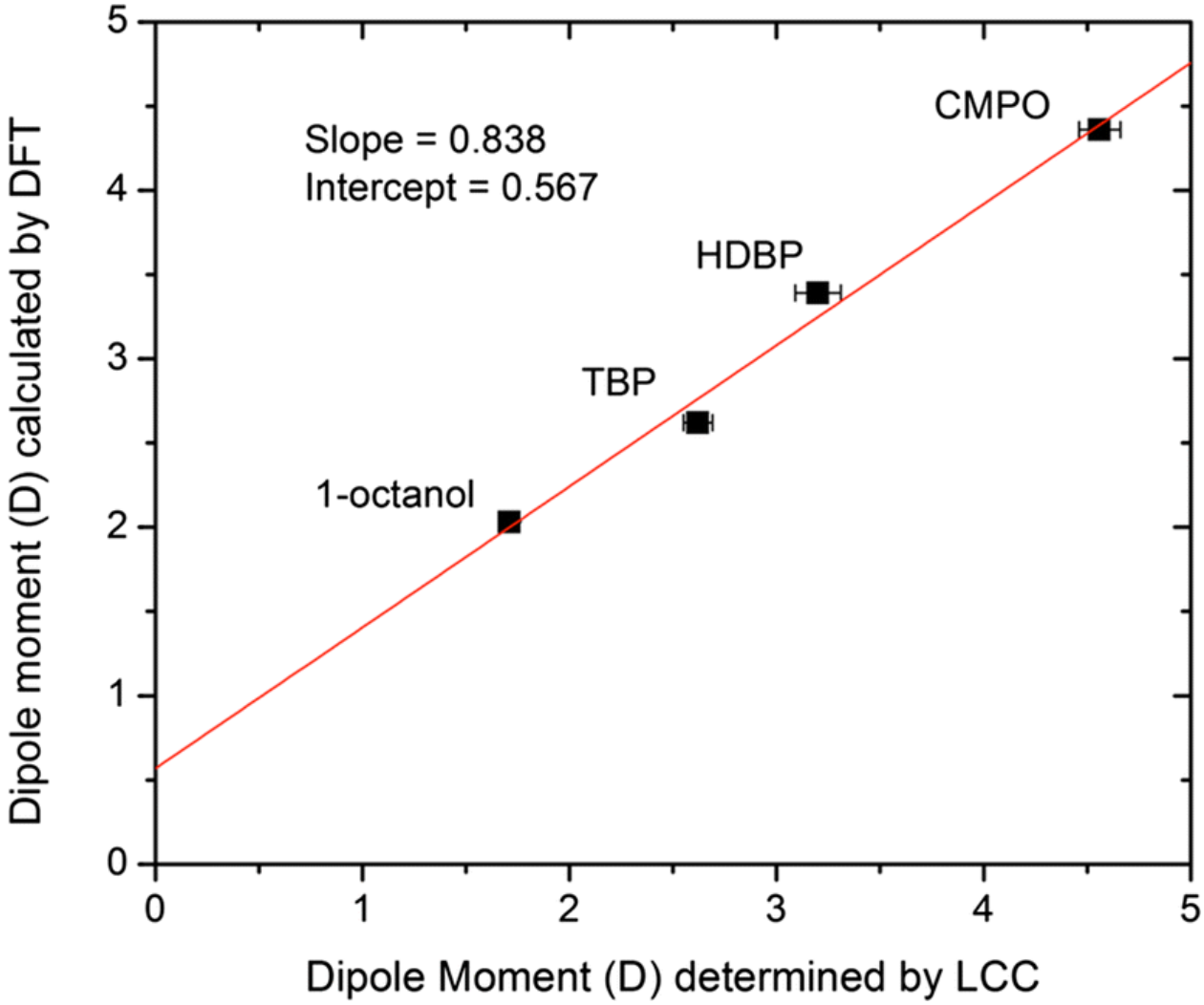

Figure 2.4: A comparison between calculated values from DFT and experimental data obtained in this study using the LCC. The red line is the fit of the data collected from the LCC. Based on the four data points, the two techniques (DFT and the LCC measurements) follow the same trend

Future studies using this instrument will benefit from a more in-depth investigation into this topic.

It was found that this device was not sensitive to temperature fluctuations of 1 or 2 ° C. For this reason, the temperature was not precisely controlled. In cases where temperature control is required, redesigning the cell with a thermostatted jacket would be recommended. Because the LCC is not enclosed, immersion into a liquid bath is not be suggested. Aside from the need to keep the bath liquid away from the sample, it is

possible that vapor may condense into the LCC, potentially contaminating the sample.

Many ligands of interest in the solvent extraction of metal ions are still without known dipole moments. Because of the low concentrations required, this method lends itself well to study these, sometimes expensive, compounds. Although further verification would be beneficial, and most likely necessary, Figure 2.4 suggest that it may be possible to rely on simulations for determination of dipole moments across a range of values. However, more work is required to ensure this correlation. The experimental technique used here should be valid so long as the solvent is non-polar, and solutions remain in the low concentration limit. Breakdowns in Guggenheim's equations will likely result in non-linear behavior in the left-hand side term of Equation 2.1. This puts obvious limitations on the type of chemicals that can be used for this cell. Solubility limitations of certain extraction reagent in non-polar solvents may also present a challenge although this method should be useful for solutions of low concentration, so this should be less of an issue.

2.4 Conclusions

A liquid capacitance cell was designed and fabricated and has been shown to provide accurate measurements of the dielectric constant of solutions of low polarity. The apparatus was tested by determining the dipole moments of 1-octanol and TBP, and was found to give results in good agreement with literature values. The dipole moment of HDBP and CMPO were reported for the first time with a degree of precision comparable to previous studies of other compounds. These experimental insights, as well as the new values of dipole moment, will be of value for further studies, both experimental and theoretical, of liquid-liquid extraction processes for metal ions relevant to used nuclear fuel.

Chapter 3

Parameterization and Examination of Dibutyl-phosphoric Acid Dimers

3.1 Introduction and Background

A stable energy supply is a requirement for advanced economies to maintain their standard of living and for developing countries to improve their human development index and reduce poverty.[1] Furthermore, there is a push to increase utilization of clean and sustainable energy sources. Nuclear energy is the largest source of non-CO_2 emitting energy and could make an impact toward a sustainable energy strategy. The abundance of fuel and the round-the-clock operation of a nuclear power plant simplify the task of increasing power grid capacity.[22] However, the production of high-level radioactive waste is one of the barriers to the widespread adoption of nuclear power. Advanced nuclear fuel cycles can directly address this issue. Recycling spent fuel greatly increases uranium economy and reduces the volume of high-level waste. Solvent extraction (SX) is a common and scalable process for reclaiming uranium and plutonium from used fuel to incorporate and reuse it in mixed oxide fuel.[28]

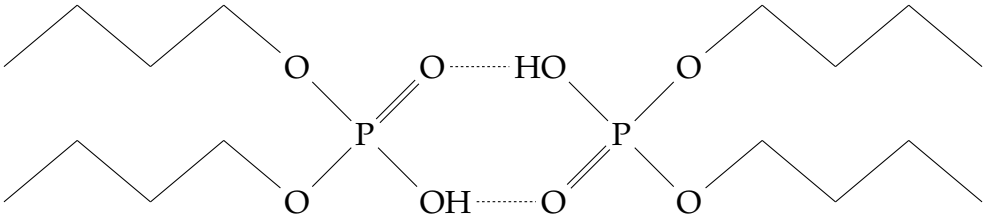

Figure 3.1: Chemical structure of the dibutyl-phosphoric acid (HDBP) dimer, with an eight-membered ring formed via the hydrogen-bonded oxygens and including the phosphorus atoms.

Tributyl phosphate (TBP) is a common reagent in many industrial SX schemes such as the plutonium uranium reduction extraction (PUREX) process.[79] However, during PUREX operation, radiolytic degradation of the solvent will result in the formation of dibutyl phosphate (HDBP), which causes coextraction of certain unwanted elements such as zirconium and plutonium(III).[32, 80] Existing literature suggests that HDBP exists predominantly as a cyclic dimer in dilute nonpolar organic solutions.[33] In this conformation, hydrogen bonds form between two molecules to create an eight-membered ring,

as shown in Figure 3.1. However, under certain conditions, it may contribute to the existence of a larger structural hierarchy.[37, 38, 39, 40, 41] The sizes range from small dimers to large reverse micelles, which can eventually lead to a third phase. Such large aggregates may cause process disruptions and criticality events as fissile materials concentrate within the third phase.[42, 43, 44, 45, 46] Beyond this, what aggregate formation means for synergism, ion selectivity, and extraction efficiency is not yet fully understood.[47]

Molecular dynamics (MD) is a useful tool for studying the molecular-level behavior that drives aggregate formation . While usefulness of visualization has been demonstrated in many previous works regarding TBP,[51, 52] HDBP has seen less attention. This is perhaps due to a lack of an accurate force field (FF) for HDBP. A useful model should provide in silico predictions and elucidations of in vitro observations with a high degree of confidence. The conjunction of these two techniques will yield greater insight than the sum of either technique used alone.

In this work, reparameterizing the FF of HDBP is described using the general Amber FF (GAFF) as a starting point. In previous work from our research group, we have carefully characterized TBP[60] but the acidic proton of HDBP presents new challenges. In addition, less experimental data are available for HDBP compared to TBP, forcing us to estimate certain parameters based on empirical correlations. Finally, a potential mean force (PMF) study probing the ideal geometry of the HDBP dimer was performed using the reparameterized FFs. The provided insights into the role of hydrogen bonding between HDBP dimers will be discussed.

3.2 Methods and Experiments

3.2.1 Evaluation of Physical Properties

Reparameterization is the process of modifying an existing molecule's force field so that the chemical properties in-silica resemble that of in-vitro. Three critical properties are typically considered: density (ρ), heat of vaporization (ΔH_v), and dipole moment (μ)[61]. Once these properties were matched, the FF was tested by comparing the self-diffusion coefficient (SDC) with a known experimental value. HDBP is commercially available and thus the density is well known. For verification, a tensiometer (Sigma 700, Biolin Scientific) was used to measure the density in-house. Dipole moments were measured using an in-house dipole meter as described elsewhere.[81] The simulated dipole moment is defined as the average of all instantaneous dipole moments of molecules in solution

$$\mu = \left\langle \left\| \sum_a q_a(\bar{r}_a - \bar{R}_n) \right\| \right\rangle_n \tag{3.1}$$

where q, is the atomic charge; r, position; and R, center of mass. The subscript a represents the atoms of molecule n.

Measurements of the heat of vaporization of HDBP do not exist, and experiments that characterize it require significant instrumentation[82, 83]. In lieu of experimental data, the heat of vaporization was calculated from the solubility parameter and was estimated

to be 17.5 kcal/mol. The solubility parameter is defined as

$$\delta = \sqrt{\frac{\Delta H_v - RT}{V_m}} \tag{3.2}$$

where R, is the ideal gas constant; T, temperature in Kelvin; and V_m, molar volume[84].

The heat of vaporization was calculated by applying Equation 3.2 after a group contribution method was used to estimate the cohesive energy density (used to calculate the solubility parameter)[85]. The same group contribution technique was used by Lumetta et al. to successfully estimate the solubility parameter of bis-(2-ethylhexyl)phosphoric acid (HDEHP)[86], a molecule similar to HDBP.

A reliable method to calculate the heat of vaporization from simulations is to take the difference in potential energy from gas phase and neat liquid phase.[87]. This is shown in the equation below

$$\Delta H_{vap}(T) = U_{gas} - U_{liquid} + RT \tag{3.3}$$

where U is the potential energy. Accurate calculations of the internal energy require all nonbonded interactions to be captured. For example, ionic liquids are known to vaporize as their ion pairs[88]. The electrostatic interactions between them are a significant contribution to their internal energy. Thus, gas-phase simulations must include both ion pairs.[89]. Similarly, it is possible that HDBP may exist as hydrogen-bonded dimers in gas phase. If so, then their hydrogen-bonding interactions are a critical component of the gas-phase energy.

Although there are no direct measurements proving the existence of HDBP dimers in gas phase, evidence exists for a variety of similar compounds. Fourier transform infrared (FTIR) spectroscopy studies have shown that various organo-phosphorus acids exist as hydrogen-bonded dimers in the gas phase[90, 91, 92]. These compounds form the same type of eight-membered ring as HDBP. A sharp, free OH stretch peak occurs at temperatures beyond 400 K, which signifies monomer production. This phenomenon has been well documented. The spectra of HDEHP is missing the free OH stretch[93], which suggests that no monomers exist in the gas phase at room temperature. HDEHP has bulkier carbon chains compared to HDBP but the molecules share similarities in the PO_3OH core affecting the strength of the dimer. It is thus likely that HDBP should also exist as a dimer in gas phase.

Moreover, the measured values from an experimental study characterizing the solubility parameter of HDEHP, specifically in the dimer form[94], closely match estimates given by the group contribution method used in our work. This further suggests that the heat of vaporization related to the solubility parameter and thus the volatile unit for HDBP and HDEHP are dimers. Again, the structural similarity between HDEHP and HDBP is the only basis for assuming their similar behavior. For comparison, both monomer and dimer gas phase were examined.

The final parameter, the SDC, is an important test of the bulk properties and can be calculated via Einstein's relation

$$D_s = \frac{1}{2d} \lim_{t\to\infty} \frac{d}{dt} \left\langle \sum_n |r(t) - r(0)|^2 \right\rangle \tag{3.4}$$

where d is the dimensions of the system, in this case three. The atomic positions, r, are

summed over all molecules, n. In short, the squared displacement of particles is linearly related to time. Simulations that have been extended out to the long-time limit will exhibit this linear behavior. The experimental value for D_s was taken from Pochylski et al.,[95] who used pulsed field gradient NMR.

3.2.2 Simulation Setup

The simulations were run using Amber14[77] on a local cluster. Neat phase and umbrella sampling simulations were both run on GPUs using PMEMDCUDA[96, 97]. A truncated octahedron with periodic boundary conditions was used. Gas phase simulations ran on CPUs with SANDER. All simulations use a time step of 1 fs. The electrostatic cutoff was set at 10 Å. Atomic hydrogens were restrained via SHAKE to a tolerance of 10^{-7} . The center of mass movements were removed every 1 ps. Pure liquid-phase and gas-phase simulations were performed in triplicate. The reported values and uncertainties are the averages and standard deviation of the three runs, respectively.

For pure liquid-phase simulations, initial structures were generated using PACKMOL[98] as a large sphere of 500 HDBP molecules. Once the system equilibrated, a cyclic HDBP dimer was selected from the liquid phase for use as the initial gas- phase structure. This was done manually using visual MD (VMD)[99].

The liquid-phase simulations utilized periodic octahedral boundary conditions. This was to alleviate any potential self- interactions of large aggregates across the periodic boundary. The truncated octahedron has a larger inscribing sphere than the cube. Thus, the truncated octahedron can contain a larger molecule than the cube while occupying the same volume, reducing the likelihood of self-interaction. Given the strength of phosphate hydrogen bonds as well as the concentration of HDBP molecules, it is plausible that aggregates large enough to self-interact may form. Although these percolation issues were

not expected, the precautionary measure was taken nonethe- less. The initial structure was first initialized as a sphere, which approximates a truncated octahedron but leaves void bubbles in the corners. This effect becomes more pronounced as the system volume increases. Thus, once bad contacts were removed through energy minimization, a 1 ns volume pre- equilibration stage was run. It is recommended to split this 1 ns into many short runs, as PMEMDCUDA fixes the Ewald grid size once the simulation begins. This effectively allows the grid size to remain dynamic over the pre-equilibration stage. An annealing stage was performed over isometric conditions where the temperature of the solution was increased linearly starting from 0 to 500 K over 1 ns and then cooled to 300 K over another 1 ns. This slow heating and cooling lets the system jump over any kinetic traps that might exist.[35] Unlike large proteins, the nature of pure substance simulations is such that the heat-induced breakdown of hydrogen bonds is not important, as they can easily reform during cooldown.

For the equilibration stage, the system was allowed to sit in the isothermal-isobaric (NPT) ensemble at the desired temperature and pressure, which were 300 K and 1 atm, respectively. A Langevin thermostat and a Berendsen barostat were applied. The density, temperature, and internal energy were evaluated every 10 ps and then averaged over 1 ns. Equilibrium was declared when the 1 ns average of the last 50% of the total simulation time fell to within 1% of the average of the values in the last 10% of the total simulation time. A minimum run time of 15 ns was enforced and found to be sufficient in all cases. Finally, the systems were run for an additional 20 ns. This was the sampling stage where all reported data were collected.

Gas-phase simulations do not require volume equilibration as the behavior is assumed to be ideal. In addition, the maximum temperature during the annealing stage was only 370 K as HDBP dimers will begin to break down beyond this temperature. Total breakdown was observed around 400 K. It is interesting to note that experimental FTIR

data provided by Asfin et al. showed that 400 K was required before any monomer was observed.[90]

Trajectory analysis was done with the aid of AmberTools14.[77, 100, 101] Analysis and generation of free-energy diagrams were done using PyMBAR[102, 103] which is the Python implementation of the multistate Bennett acceptance ratio. The available tools were scripted together in-house using Python.[104, 105] Visualization was done through tools supplied in VMD[99, 105].

3.2.3 Parameterization of HDBP

The program Avogadro[106] was used to perform molecular mechanics optimization using the GAFF. As a secondary check, Gaussian09[75] was used for quantum mechanical optimization at the HF/6-31G* level. Both methods yielded near-identical structures, likely due to the simple shape and symmetry of the molecule. Then, partial charges were assigned via the program Antechamber[107], using the AM1-BCC method[108, 109]. Thus, the initial FF was generated from GAFF[110].

The general parameterization procedure is adapted from our previous work on TBP reported by Vo et al.[60], but with some modifications based on the work of Dang and Chang[61], which describes the process of manually scaling Lennard-Jones (L-J) parameters to better match the experimental density and heat of vaporization in the simulation. Before matching the density and heat of vaporization, the dipole moment was matched by finding a uniform scaling factor for all partial charges. Once this scaling factor had been applied to all charges, the L-J parameters were modified in an automated fashion using the Nelder-Mead simplex algorithm[111]. Although the algorithm attempted to minimize the squared sum error of the three critical properties, its purpose was not explicitly for FF development. Rather, it was used to identify atoms which were particularly impactful

to the three critical properties. These atoms were then manually modified. This strategy was devised to minimize both the parameter space and the deviation from default GAFF parameters.

GAFF defines no L-J parameters for the hydroxyl hydrogen (H_o). The typical assumption is that the radius of the hydroxyl oxygen (O_h) is large enough to encompass the H_o atom, preventing it from overlapping with other atoms. In practice, this regularly caused Coulomb catastrophes in the bulk HDBP system. A possible culprit is the P atom. Its large size and high partial charge may complicate intermolecular dihedral interactions. It is speculated that atoms forming a dihedral with the O_h and H_o atoms may collapse into each other because neighbor and second neighbor non-bonded intra-molecular interactions (1-2 and 1-3 interactions) are excluded in MD[112]. This was remedied by adopting H_o parameters from the updated GLYCAM06-h FF. These modified H_o parameters were fitted such that its van der Waals contribution to methanol-methanol hydrogen bonds were insignificant[113]. Further, it prevented overlap in implicitly solvated iduronic acid, which is heavily involved in O_h and H_o contributing dihedral interactions[113]. For these reasons, the H_o correction was deemed to be minor, and thus appropriate for this work. Most importantly, no Coulomb catastrophes were observed after this change. It is to be understood that the "unoptimized" HDBP FF includes this H_o correction. Furthermore, the new H_o atom was excluded from the parameter space.

For each incremental change to the FF, using methods described above, the system was simulated in triplicate. The final values of the simulated properties are the ensemble averages across the triplicate simulations. The dipole moment was calculated from liquid-phase simulations, using Equation 3.3, and heat of vaporization from Equation 3.3. All relevant information regarding these calculations was taken from AmberTools[77]. Changes were made until the three properties matched to within 5% of target values, which are the experimentally determined or empirically estimated values.

3.2.4 Umbrella Sampling

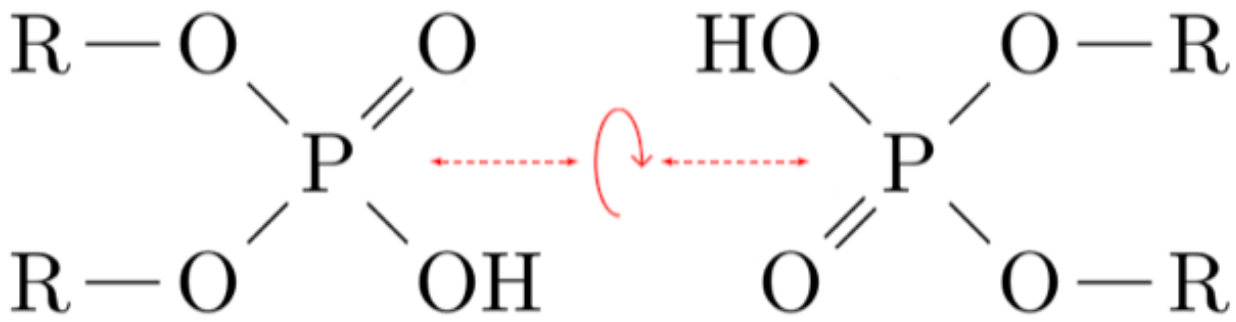

Figure 3.2: Relative movement of the HDBP molecules during the umbrella sampling scheme.

As mentioned previously, HDBP is suggested to exist in a dimer in nonpolar solvents by forming two hydrogen bonds. It is therefore of interest to determine accurate hydrogen-bonding criteria for the purpose of future studies. Umbrella sampling was performed to generate a two-dimensional PMF, which was generated using MBAR[102]. Analysis of low free-energy conformations provides information regarding optimal geometries of the HDBP dimer. The reaction coordinates are the distance between the two phosphorus atoms and the pseudodihedral angle between the two P=O groups. The term pseudodihedral, which will be denoted as the OPPO pseudodihedral, is coined for the fact that the phosphorus atoms of the two dimers are not bonded. The dihedral angle is calculated by projecting the P=O vectors onto a plane normal to the P-P vector. The lack of bonded terms along the P-P vector affords the dihedral angle additional conformal flexibility. These reaction coordinates can be interpreted as the action of pulling apart the dimer symmetrically and twisting about the molecule central axis, as shown schematically in Figure 3.2. The distance between the phosphorus atoms was varied from 3.25 to 4.60 Å in 0.15 Å increments. As it is drawn in Figure 3.2, the OPPO pseudodihedral rests at 180° . This angle was varied from 90° to 270° in 6° increments. The same run parameters and procedures used in the pure HDBP simulations were used in the umbrella sampling. The

initial structure of the HDBP cyclic dimer was taken from the sampling stage of gas-phase simulations. No further structure minimization was necessary. One hundred and fifty n dodecane molecules were solvated around the dimer as a sphere with a radius of 21 Å. This radius was twice the maximum radius of gyration of the HDBP dimer as calculated from the gas phase and is more than twice the electrostatic cutoff. The n-dodecane FF was taken from previous work.[60] This initial structure was first equilibrated using the same procedure outlined for parameterization, Section 3.2.2 Each umbrella was simulated for 30 ns and was sampled every 10 ps. Center of mass restraints were added to keep the dimer together during equilibration. These restraints persisted until the sampling stage, where the PMF constraints take over. The tail end of one of the butyl chains was pinned to the center of the octahedron at all times. All applied umbrella potentials were harmonic. The force constants for the pseudodihedral and distance restraints are 100 kcal/(mol*rad^2) and 50 kcal/(mol*Å^2), respectively. The harmonic response regions are ±3° and ±0.5 Å, respectively, about the reference point.

3.3 Results and Discussion

3.3.1 Parameterization Results

The final FF is described in Table 3.1 and depicted in Figure 3.3. The asterisks denote parameters that have been altered from default values. The physical properties before and after optimization are listed in Table 3.2. As mentioned previously, the dipole moment was the first property to be matched and was done so via charge scaling. The original GAFF overstated the dipole moment. The final partial charges were scaled down by a factor of 0.73, representing a 27% reduction from the original. This resulted in a P atom whose charge was comparable to that of other studies which utilized charge scaling[114].

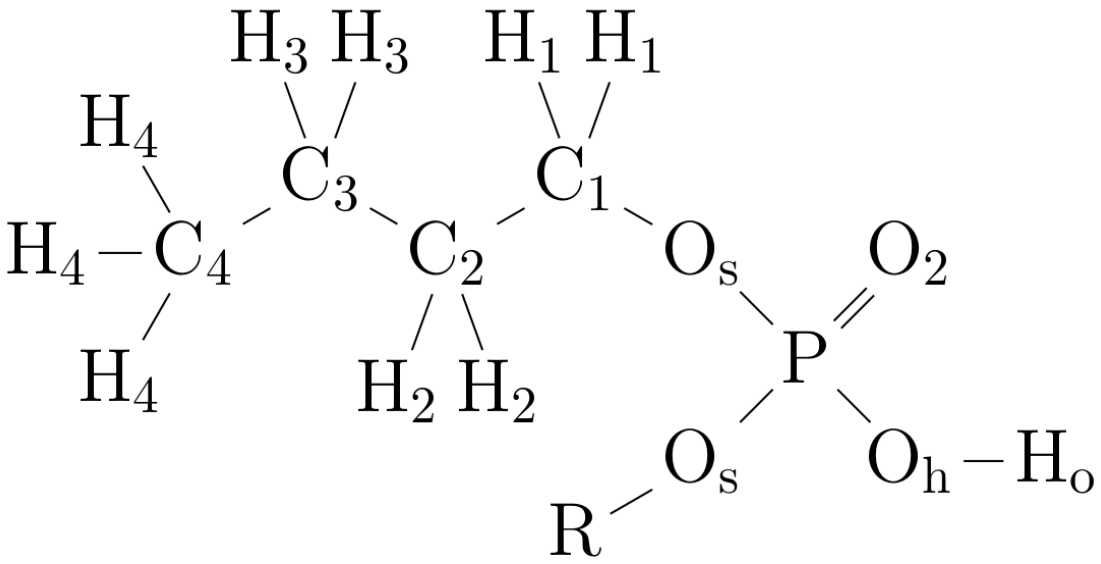

Figure 3.3: Schematic depicting the atom types of the HDBP molecule. The van der Waals parameters of O_h and H_o were modified. The partial charges of all atoms were uniformly reduced.

atom	amber type	partial charge (q)	r_0 (Å)	ϵ (kcal/mol)
P	p5	1.184425*	2.1000	0.2000
O_2	o	−0.584949*	1.6612	0.1750*
O_s	os	−0.430116*	1.6837	0.1700
O_h	oh	−0.538302*	1.7210	0.1750*
H_o	ho	0.353320*	0.2000*	0.0300*
C_1	c3	0.122567*	1.9080	0.1094
C_2	c3	−0.074387*	1.9080	0.1094
C_3	c3	−0.057962*	1.9080	0.1094
C_4	c3	−0.067233*	1.9080	0.1094
H_1	h1	0.041938*	1.3870	0.0157
H_2	hc	0.030624*	1.4870	0.0157
H_3	hc	0.030624*	1.4870	0.0157
H_4	hc	0.025696*	1.4870	0.0157

Table 3.1: Optimized parameters for HDBP
Asterisks denote parameters that have been altered from default values

Although charge scaling did reduce the error in the heat of vaporization somewhat, further correction was found to be necessary by modifying the L-J parameters. The changes to the van der Waals parameters did not greatly affect the dipole moment and

	ρ (g/mL)	ΔH_v(kcal/ mol)	μ (D)
GAFF	1.08 ± 0.002	19.3 ± 0.7	3.31 ± 0.05
optimized FF	1.06 ± 0.001	18.2 ± 0.5	2.72 ± 0.02
target value	1.06 ± 0.005	17.5[85]	2.62± 0.07 [115]
% Difference	0.0	3.8	3.7

Table 3.2: Comparison of critical properties

no additional tuning of the charge scaling was necessary as L-J parameters were being modified. Using the Nelder-Mead simplex minimizer[111], it was found that changes in donor-acceptor (D-A) oxygens yielded the greatest changes in the FF. These are defined as O_h and O_2. Thus, the heat of vaporization and density were parameterized around these atoms. It is likely that these atoms are sensitive because they are the ones involved in hydrogen bonding interaction, which, as mentioned previously, is the primary aggregation mechanism for HDBP.

Density was already well matched; however, parameterization brought the density to a very close match to the literature value. This small change was likely due to diminished electrostatic interactions. The L-J depths (ϵ) were modified to reduce interaction energies and therefore heat of vaporization. Default GAFF parameters define this as 0.2000 and 0.2104 kcal/mol for O_2 and O_h, respectively. Each was reduced to 0.1750 kcal/mol.

It is possible that the reduction in the interaction strength is necessitated by the addition of the GLYCAM06-h parameter for the H_o atom. However, the FFs before and after the H_o correction cannot be compared. Because of the previously discussed Coulomb catastrophes, the bulk HDBP system cannot be simulated without the H_o parameters. Regardless, it is unlikely the H_o correction introduces significant changes to behavior beyond inhibiting catastrophe. It was previously discussed that the H_o parameters contribute little additional L-J forces to hydrogen bond interactions in methanol[116]. This is important as hydrogen bonding in AMBER is governed by electrostatics and L-J interactions of the D-A oxygens. The changes in our optimized FF is likely rooted in an overstatement of the

original hydrogen bond strength.

MD simulations using our optimized FF produce three critical properties such as density, heat of vaporization, and dipole moment that match closely with measured values from experiments or estimated values from semiempirical correlations, as discussed in Section 3.2.1 above. Table 3.2 compares the critical properties with those found using the initial GAFF and parameterized values of HDBP calculated as discussed above. The final row in Table 3.2 shows the difference between the optimized and target values. The optimized parameters all fall within 4% of the target values.

model	U (kcal/mol of HDBP)
monomer	-41.74 ± 0.11
dimer	-48.61 ± 0.32
ΔU	6.87 ± 0.43

Table 3.3: HDBP Monomer vs Dimer Gas-Phase Potential Energy from MD Simulations Using the Optimized FF

The heat of vaporization calculations assume that the volatile unit for HDBP is a dimer. Table 3.3 shows the difference in energy between the gas-phase monomer and dimer, which can be attributed to hydrogen bonds. The numbers are reported as per mol of HDBP (monomer), which means that the net interaction energy of the cyclic dimer compared to two free monomers averages 13.74 kcal/mol dimer in the gas phase. As discussed previously, factoring in this energy is critical to calculations. As per Equation 3.3, this unaccounted energy in the gas phase will directly affect the final value for heat of vaporization. Given the strength of PO_3OH hydrogen bonds, this omission should be considered significant. When considering the gas phase to be a monomer, this difference in energy was uncorrectable.

Although the three critical properties are well matched, it is known that charge scaling affects viscosity[114]. Thus, the optimized FF was validated against the experimental SDC, which is inversely related to the viscosity. Figure 3.4 shows the mean square dis-

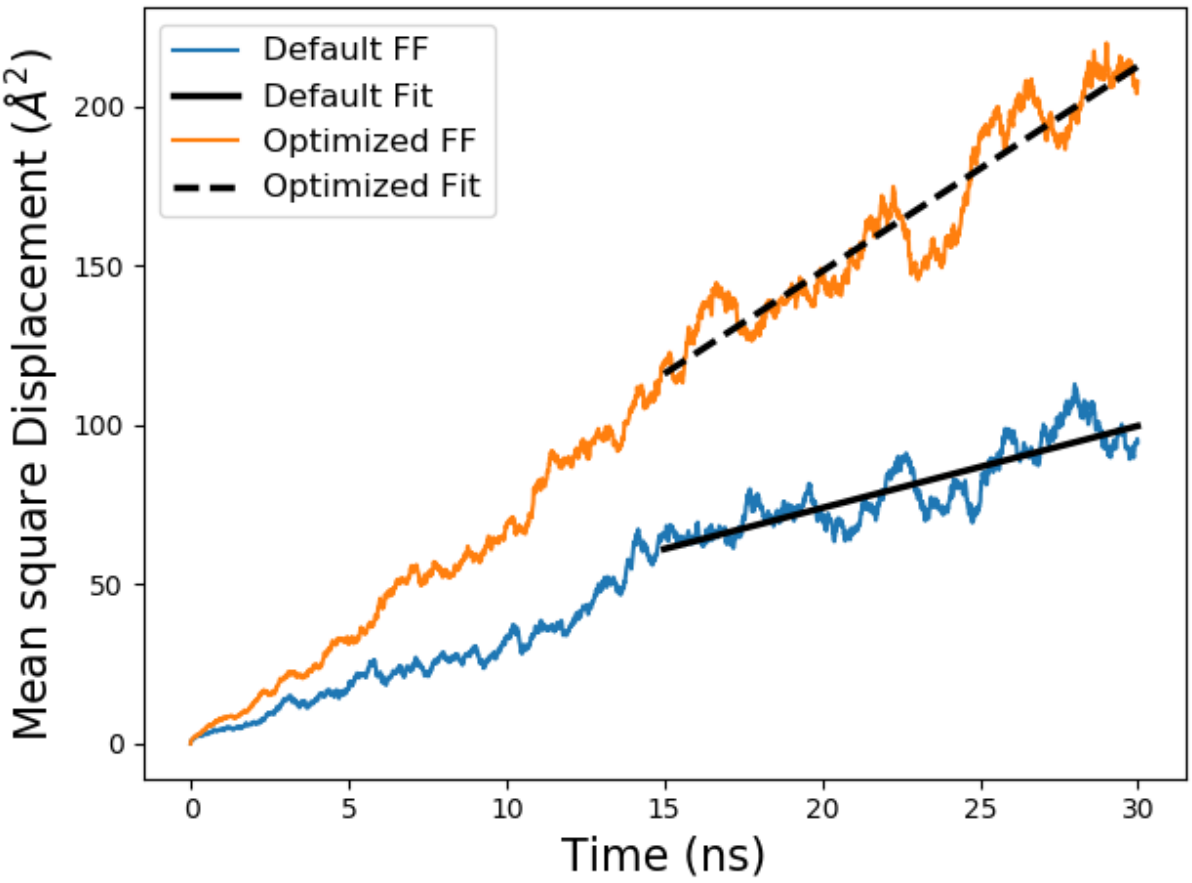

Figure 3.4: Mean square displacement of HDBP molecules in simulation as a function of time. The diffusion within the default and optimized FF is compared. The latter 15 ns of each simulation was used to find the SDC.

placement of the unoptimized and optimized FF. For this calculation, the first 15 ns was discarded. The diffusion coefficient was calculated from the fit of the proceeding half of the simulation, as per Equation 3.4. These coefficients can be found in Table 3.4. The diffusion constant in the optimized FF deviated from the literature values by 18.3%. This is comparable to previous work on TBP[51], which saw a deviation of 17% in the final FF. The unoptimized FF understated the value by 63.7%. The original GAFF parameters overstated the dipole moment which likely resulted in a more viscous fluid. Further, it is possible that the reduction on the L-J potential, ϵ, on the D-A oxygen, which effectively weakens hydrogen bond interactions, allows for a more fluid medium. The optimized

FF represents a significant improvement in this metric, despite not having been explicitly parameterized for it.

	D_s ($\times 10^{-7}$cm^2/s)	% difference from literature
default + H_o	0.429	67.3
optimized	1.07	18.3
literature	1.31	

Table 3.4: SDC of HDBP at 300 K

Although the exact speciation of aggregates in bulk HDBP is not known, FTIR studies of HDEHP have shown no absorption bands for free OH. This signals that strong hydrogen bonds are prevalent throughout the liquid[95]. This is also seen in the simulation. Hydrogen bonds in the bulk were quantified in the following manner. First, an arbitrarily high cutoff was set as a first pass to identify potential hydrogen bonds. Then, the distribution of D-A angles and distances were plotted in histograms. The point which represents 95% of the distribution was taken to be the cutoff for distance and D-A angles for hydrogen bonds. These were found to be 3.4 Åand 53° , respectively. This can be compared to CPPTRAJ which provides a standard distance and D-A angle cutoff for hydrogen bonds at 3 Åand 35° , respectively. Analysis of the bulk simulations shows that nearly all HDBP molecules are hydrogen-bonded to one another in some fashion, acting as donor, acceptor, or both, at all times. On average, in the unoptimized FF, 96.1 ± 0.9% of all OH atoms is engaged in hydrogen bonds. For the optimized FF, it is 95.4 ± 1.1%. In both cases, the majority of OH atoms are involved in hydrogen bonds, as expected from FTIR studies. Additional details regarding the determination of hydrogen bonds and the difference between the optimized and unoptimized FF are provided in the appendix.

3.3.2 PMF Insights into Hydrogen Bonding

As mentioned previously, the existing literature studies suggest that HDBP dissolved in a nonpolar solvent prefers to exist in a cyclic dimer. One molecule is flipped head to tail which facilitates the formation of two hydrogen bonds, as seen in Figure 3.1. Thus, the purpose of this PMF calculation is to examine the optimal geometry in this conformation. The two umbrella constraints pulled apart the dimer and twisted the molecules about the P-P axis to sample all possible conformations, which were fed into PyMBAR for analysis. The generated PMF can be seen in Figure 3.5.

The lowest free-energy region occurs between 3.25 and 3.75 Åfor the P-P distance and around 120-160° for the pseudodihedral angle. This region corresponds to a cyclic dimer, as shown in Figure 3.1. This suggests that the cyclic dimer is a stable state at the dilute limit. Hydrogen bonds greatly influence the optimal P-P distance, as they themselves have an optimal distance that is expressed through the FF. Although the strength of these interactions keeps the optimal P-P distance between a narrow range, the pseudodihedral shows roughly 40° of conformal flexibility. This can be attributed to the nature of the constraints. Though the phosphorus atoms are part of the umbrella constraints, they are not bonded and thus not subject to intramolecular forces. Consequently, these pseudodihedral angles can be satisfied by twisting about the P-P axis, as described in Figure 3.2, or by an out-of-plane (OoP) bend of the POOH heads. In fact, low-energy conformations almost entirely correspond to an OoP bend. This can be attributed to electrostatic attraction between the ether oxygens and the phosphorus atoms, the latter of which has a large partial charge. Because the donor hydrogen can swivel, this bend does not inhibit the formation of hydrogen bonds.

Two kinds of OoP bends are seen in the lowest free-energy region. These are shown in Figure 3.6. Figure 3.6B,D shows the molecular surfaces of both conformations, respec-

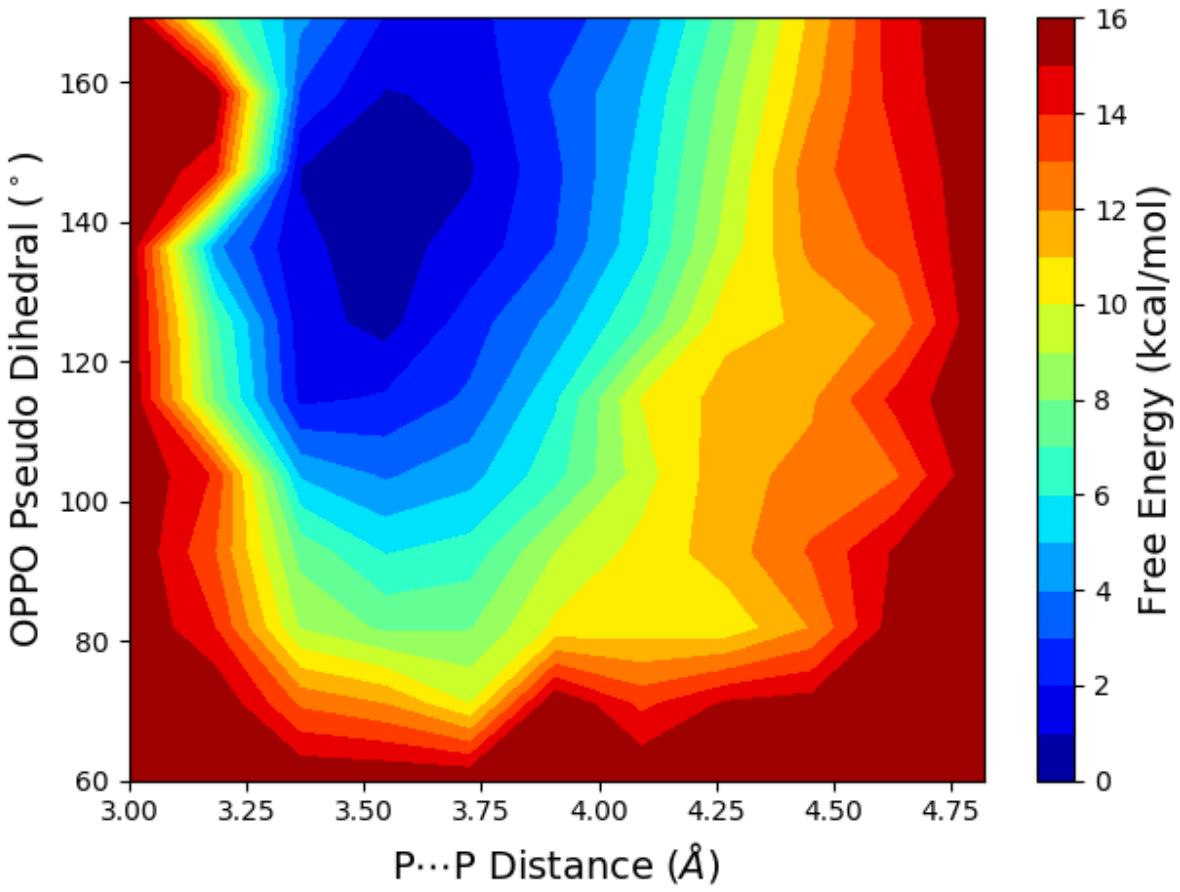

Figure 3.5: Plots A and B represent histograms of the D-A angle and distance, respectively. Conformations were taken from the 0-3 kcal/ mol free-energy region, and both D-A pairs were considered. The dashed lines represent the hydrogen bond cutoffs, which were determined by locating the point that represents 95% of the total integral of the curve. Histogram C shows the same data on two dimensions.

tively. In Figure 3.6C,D, more of the PO_3OH head becomes exposed to the solvent. This open-face conformation could possibly lead to the formation of higher-order aggregates, such as trimers. The additional exposed surface area may be conducive for another HDBP molecule to insert itself into the aggregate. This potential pathway may warrant future study that will examine thermodynamics and kinetics of spontaneous dimerization at different concentrations to determine if the dimerization process leads to a metastable state or not.

Appropriate hydrogen bonding criteria were found by making histograms of the

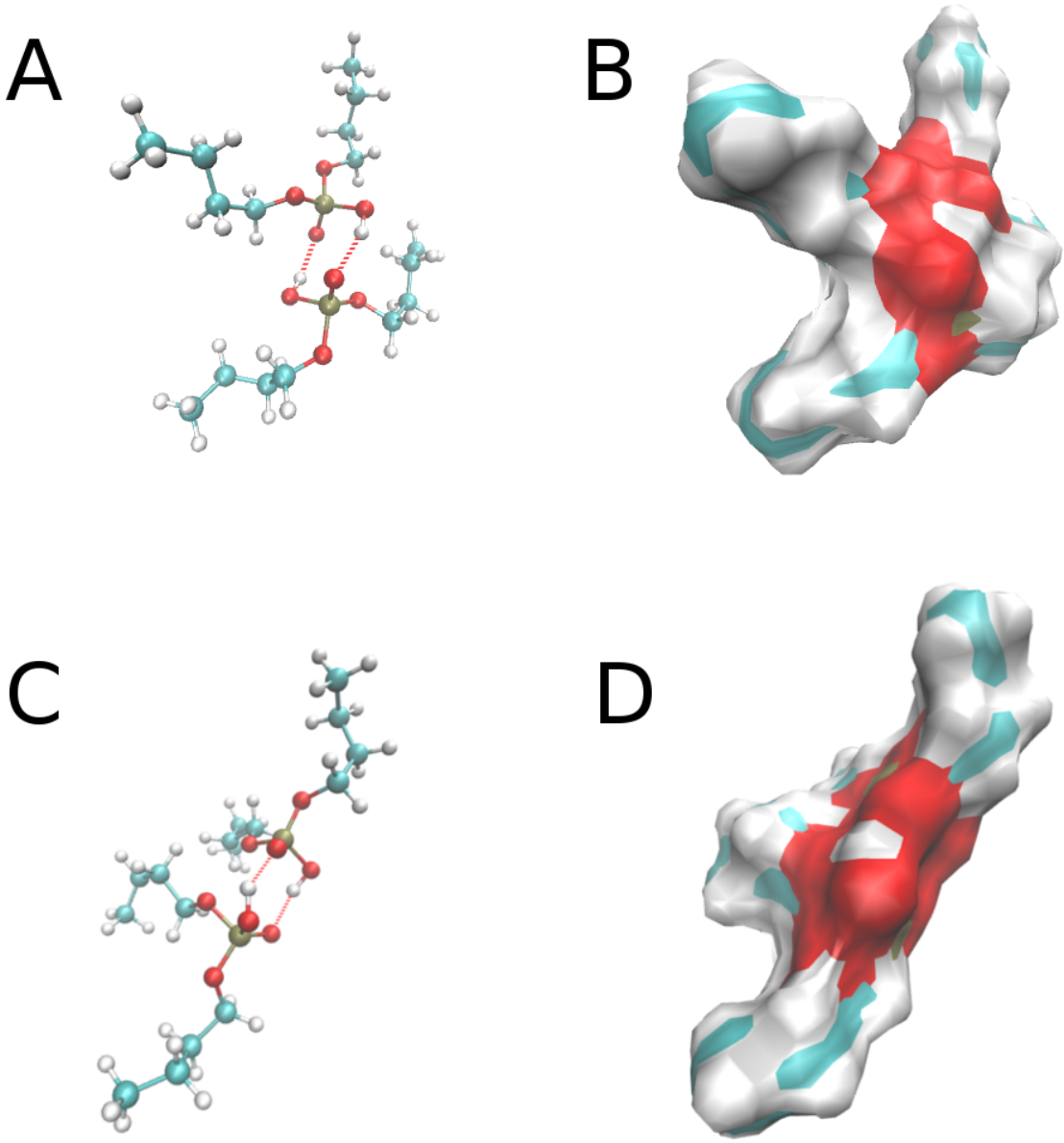

Figure 3.6: Two conformations are seen in the lowest free-energy region. (A) Represents OoP bending in opposite directions. (C) represents bending of the phosphorus atoms toward each other. (B,D) Are the molecular surfaces of the two conformations, respectively

D-A distance and angle, shown as continuous plots in Figure 3.7A,B. Analyzed onformations come from the lowest 3 kcal/mol free-energy region, and both D-A pairs have been considered. The point that represents 95% of the total integral of the histogram is chosen to be the cutoff. This shows a maximum D-A distance of 3.0 Åand a maximum

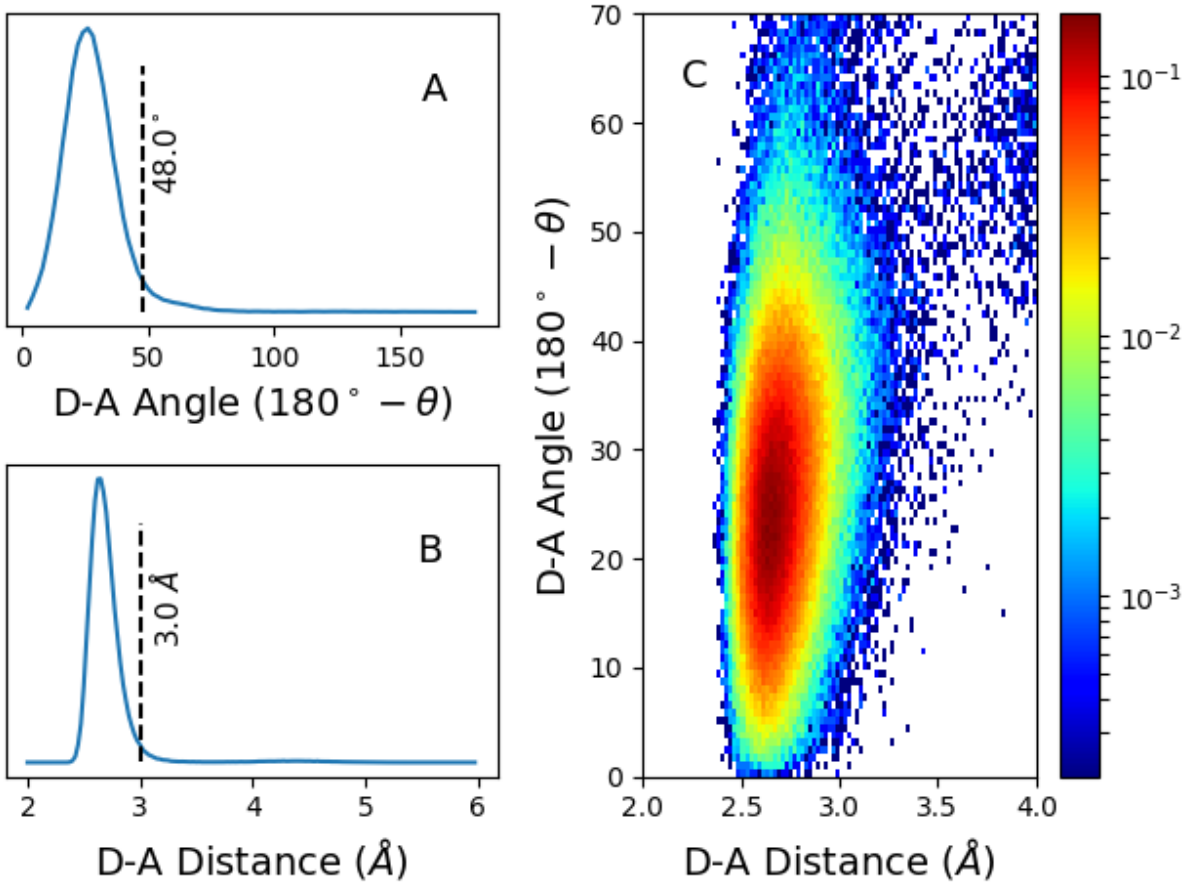

Figure 3.7: Plots A and B represent histograms of the D-A angle and distance, respectively. Conformations were taken from the 0-3 kcal/ mol free-energy region, and both D-A pairs were considered. The dashed lines represent the hydrogen bond cutoffs, which were determined by locating the point that represents 95% of the total integral of the curve. Histogram C shows the same data on two dimensions.

angle offset of 48.0° away from 180° . These values are close to what is typically used for protein studies, where programs such as CPPTRAJ typically assign default cutoffs of 45° offset and a distance of 3.0 Å[100]. The peaks of the histograms occur at 26° and 2.675 Å. Existing calculations using density functional theory (DFT) predict a D-A distance of 2.576 Å[34], which is a 3.7% difference from what is found using our FF.

It is interesting to note that there is no region within the PMF which corresponds to two monomers. As discussed in Section 3.3.1 and Table 3.3, the strength of hydrogen bonds is high, at around 6.87 or 13.74 kcal/mol dimer. When applying the hydrogen bond

criteria to all regions of the PMF, it is seen that the two molecules are always engaged in at least one hydrogen bond.

The distance and D-A angle distribution for hydrogen bonds in the pure HDBP solution can be compared to those of the PMF plot, which may be considered as a dilute system. Figure A.2 in the Supporting Information shows the side-by- side comparison between the histograms. It was observed that the hydrogen bonding angles are shallower in the bulk, while the distance still remains within the narrow band of around 2.5-3.25 Å. The close proximity of other HDBP molecules in the case of pure HDBP increases the chance that both donor and acceptor sites of each HDBP are occupied. Further, it may be more likely that OH atoms can find a straighter and therefore more energetically favorable, hydrogen bond in bulk compared to the dilute case. This means that the system has the energetic freedom to adopt more favorable angles. Whether this logic follows in the continuum between pure HDBP and the dilute limit is yet to be seen.

While this work demonstrates that the eight-membered ring, as seen in Figure 3.1, is the lowest free-energy conformation, the classical way in which it is drawn is misleading. Figures 3.1 and 3.3 show an idealized version of the cyclic HDBP dimer, where the OPPO pseudodihedral angle would be 180° . However molecular geometries assure that this exact conformation is impossible. The tetrahedral angle is 109.5° , which would mean that the P-O-H angle shown must be 125.25° . However, this angle in phosphates generally ranges from 90-110° . This makes it impossible for the O-H-O angle between two HDBP molecules to be 180° without suffering severe penalties to the conformational energy. To accommodate both the bond angles and the eight-membered ring, the hydrogen bond angle deviates by 26° from the “perfect” 180° conformation suggested in Figure 3.3.

3.4 Conclusions

The FF for HDBP has been successfully reparameterized, and simulations using this FF closely match experimentally determined values of density, dipole moment, and an estimated value for heat of vaporization. These properties were matched to a maximum error of 3.8%. The simulated values of density and dipole moment fall within the uncertainty of known experimental values. This represents a significant improvement over the default GAFF parameters for HDBP, which possessed a mean percentage error of 10.39% and a maximum of 20.85%. The new FF was then validated against the SDC and saw high improvement. Default parameters understated the diffusion by 67%. The optimized FF deviates by 18%, which is a significant improvement compared to using the default parameters.

In addition, hydrogen bond criteria have been determined for the purposes of quantifying aggregate formation of HDBP in solution for future works. These criteria were found through the calculation of a PMF of a HDBP dimer using PyMBAR. Analysis of low-energy conformations has shown that a D-A angle of 154° and distance 2.68 Åbest capture the behavior of both hydrogen bonds. Further, it was found that the optimal D-A distance matches to within 3.7% predictions made by previous DFT studies. Finally, a deviation of the angle more than 48° from the "straight" 180° angle and/or a distance between the donor and acceptor atoms above 3.0 Åindicate that the hydrogen bond is broken. This gives some confidence that the behavior of HDBP can now be accurately simulated and its aggregate formation can be properly quantifiable.

Chapter 4

Simulating and Observing the Behavior of HDBP in Non-polar Solvent

4.1 Introduction

Tributyl phosphate (TBP) is well known for its use in many industrial solvent extraction processes. One such important process is the PUREX process[79], which separates uranium and plutonium from fission products in used nuclear fuel. However, the acidic and radioactive conditions of the PUREX process will degrade TBP to dibutyl-phosphate (HDBP). The production of HDBP, with its hydroxyl group, greatly changes the extractive properties of the solution. What exactly that means is context specific. For example, in the PUREX process, this results in the unwanted coextraction of elements such as zirconium and plutonium(III)[32, 80]. In a another case, HDBP and TBP work together to synergistically extract trivalent lanthanides[40].

The complexity added by the presence of HDBP is owed to its hydroxyl group. Not only will HDBP involve itself in the complexation of extraction agents to metal ions, it will also contribute to a structural hierarchy of aggregates even before contact with any metals[37, 38]. Such ordered aggregates are formed via strong phosphate hydrogen bonds (HB). Interestingly, these aggregates themselves may greatly influence extraction. A chemically similar molecule, bis-2-ethylhexyl phosphoric acid (HDEHP), will become selective to different first row transition metals depending on temperature.[39]. In another example, depolymerizing agents reduced the extractive power of HDEHP for trivalent lanthanides by four orders of magnitude[50].

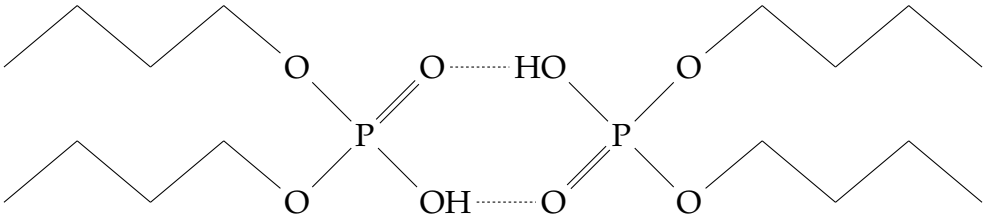

Figure 4.1: Chemical structure of the dibutyl-phosphoric acid (HDBP) dimer, with an eight-membered ring formed via the hydrogen-bonded oxygens and including the phosphorus atoms.

It is currently understood that HDBP exists mostly as cyclic dimers in dilute solutions with non-polar organic solvents[33]. Two molecules form HBs to create an eight-membered ring, as shown in Figure 3.1. However, under certain conditions, HDBP may be part of a larger structural hierarchy, which could include chains and reverse micelles[37, 38, 39, 40, 41]. Additionally, positron annihilation studies have strongly suggested that HDEHP, will form close aggregates at concentrations between 200 - 1000 mM[117].

This work utilizes a previously developed force field for HDBP[118] to examine its particular role in the formation of close aggregates. First, a PMF study was undertaken to better understand how exactly HBs contribute to aggregation. Second, solutions of HDBP was simulated across a range of concentrations where close aggregate formation is likely. These studies lead to new insights into the nature of HDBP.

4.2 Methods

4.2.1 Simulation Setup

Simulations were performed with Amber14[77] using PMEMDCUDA[96, 97]. Computational resources consisted of GPUs on a local cluster. Electrostatic cutoffs were 10 Å. SHAKE restrained hydrogens with a tolerance of 10^{-7}. Center of mass movements were dampened every 1 ps. All simulations were sampled at 300 K and 1 atm.

Packmol[98] was used to generate initial structures. All structures underwent energy minimization to remove bad contacts. A short 1 ns NPT volume pre-equilibration phase then followed. This was to alleviate the effects of the overestimated box size. Systems then underwent an extended annealing phase under isometric conditions in order to avoid any

kinetic traps[119]. The temperature was linearly ramped from 300 K to 600 K over 1 ns. This max temperature is significantly higher than 400 K, which is the point at where FTIR studies show monomer production in gas phase[90]. The system was kept hot for another 1 ns to allow for thorough mixing, then ramped down linearly to 300 K over another 1 ns. The system was then left to equilibrate over 15 ns in the isothermal-isobaric ensemble at 300 K and 1 atm. Sampling directly followed, with 20 ns in the micro-canonical ensemble.

Analysis was performed predominately with Python[104, 105] and various Pythonic tools. Pytraj[101] which is the Python implementation of CPPTRAJ[100] was used for trajectory analysis. Free energy calculations were performed using PyMBAR[103, 102]. Visualizations of molecules were created using VMD[99]. The criteria for HB distance and angle cutoffs were 3.0 Å and 48.0° respectively. The process for defining these were discussed in Section 3.3.2. All systems used n-dodecane as the solvent. The force fields for the solvent[60] and solute[118] have been described in previous works as well.

4.2.2 O-O Umbrella Sampling

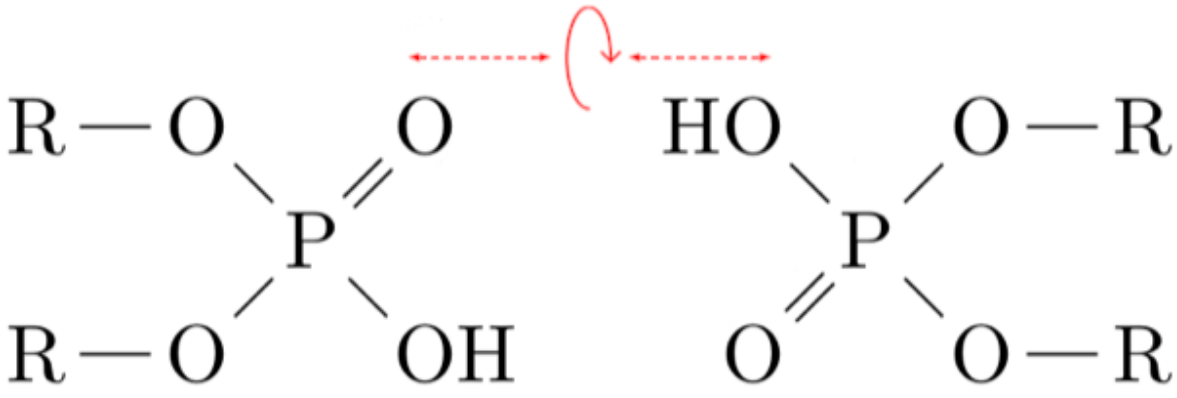

Figure 4.2: The O-O umbrella sampling schematic. Starting with the standard cyclic dimer as the base, one pair of DA atoms are stretched apart and twisted along their h-bond axis. This serves to regulate the characteristics of one h-bond while leaving the other free.

The O-O PMF is named for the two atoms which are primarily involved in the

umbrella sampling schematic. The dimer was pulled and twisted along the h-bond axis of one pair of DA atoms. The atoms were stretched between 2.35 - 4 Å and in increments of 0.15 Å. The PDA made by the phosphorus, acceptor, donor, phosphorus atoms were swept across 0 - 180° in 6° increments. A visual representation of the schematic can be seen in Figure 4.2.

For the initial structure, a cyclic HDBP dimer was spherically solvated with 150 n-dodecane molecules. The radius of the sphere is 21 Å, more than double the electrostatic cutoff and the radius of gyration of the dimer. Periodic truncated octahedral boundary conditions were imposed. Center of mass restraints were added to keep the dimer intact during equilibration. This was replaced with the umbrella restraints after equilibration. The end of one butyl tail was pinned to the center of the sphere at all times in order to prevent wrapping of the solute. This was to avoid complications with the umbrella constraints which do not account for wrapping. The harmonic force constants for the PDA and DA distance were 100 kcal/(mol rad^2) and 50 kcal/(mol Å^2) respectively. Harmonic response regions are ±3° and ±0.5 Å respectively.

4.2.3 Dry Organic Phase Simulations

Solutions consisted of 100 randomly arranged HDBP molecules. N-dodecane was similarly distributed, with their exact number corresponding to desired concentrations as calculated from molar volumes. Concentrations were 200 mM to 1000 mM, in 200 mM increments. This corresponds to 2115, 1015, 648, 464, and 354 molecules respectively. Initial box sizes were set at, 64, 50, 44, 40, and 37 Å to a side. These were set slightly larger than the true volume of the system in order to allow Packmol to find a packing solution. Periodic box boundary conditions were used. Solution simulations used a cubic box and were performed in triplicate with a 2 fs time step. Reported data represents ensemble

averages across each run. Errors are the standard deviation.

Sampling was done sparsely with 40 ps between each snapshot of the trajectory. This was to account for slow rates of interaction between aggregates at low concentrations. HB criteria were applied to each snapshot and the network of bonds was mapped out. Individual graphs represents a single aggregate and were singled out of the trajectory, creating a repository of aggregate species and all of their observed conformations. In order to directly compare aggregates of different n, calculated energies were normalized on a per molecule of HDBP basis.

4.3 Results and Discussion

4.3.1 O-O Potential of Mean Force and Insights into Hydrogen Bonding

To reiterate, the P-P PMF from previous studies was designed to examine a conformation of HDBP which is understood to be a likely metastable state[118]. The O-O PMF differs in that it is designed explicitly to break apart the HB interactions which are characteristic of HDBP aggregates. The PMF calculation can be seen in Figure 4.3. Within this figure lies numbers which correspond to regions of particular interest. Typical and representative conformations found within these regions are shown in Figure 4.4. The average number of HBs found across all conformations within a particular reaction coordinate bin is seen in Figure 4.5. The reaction coordinate bins are identical to the ones used for the PMF, as are the numbered regions.

The lowest free energy region show a wide variation in pseudo-dihedral angle. This is related to the to the out of plane bend which the HDBP dimer exhibits[118]. AMBER, nor nature, subjects HBs to the same forces as molecular bonds. This allows much greater

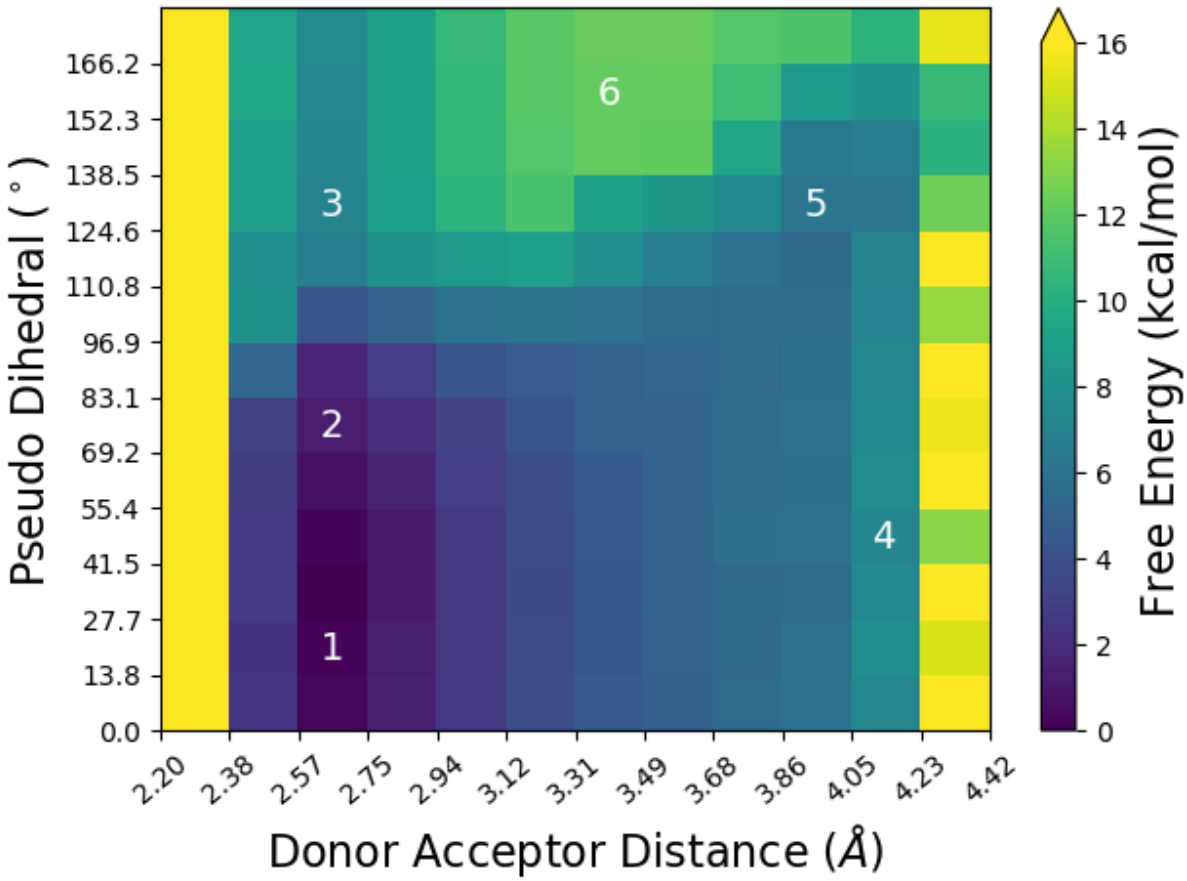

Figure 4.3: The O-O PMF. Six regions of interest are enumerated. Representative conformations within this area are seen in Figure4.4.

conformal freedom. As the two HDBP molecules bend back and forth, the geometry of the PDA can fluctuate greatly without much affecting the overall orientation of the molecules with respect to each other. This is not so for the DA distance, which has a preferred equilibrium distance that is determined by the non-bonded force parameters.

Between DA distances of 2.38 to 2.94, we see a column like region which has been enumerated from 1 to 3, and illustrated in Figure 4.4. The shape is more obvious in the HB diagram, Figure 4.5. This column sweeps the PDA through the full 180° , while the regulated DA distance is kept in a range such that they are bonded. Since the PMF rotates about the bonding axis of the regulated DA pair, the PDA reaction coordinate does not

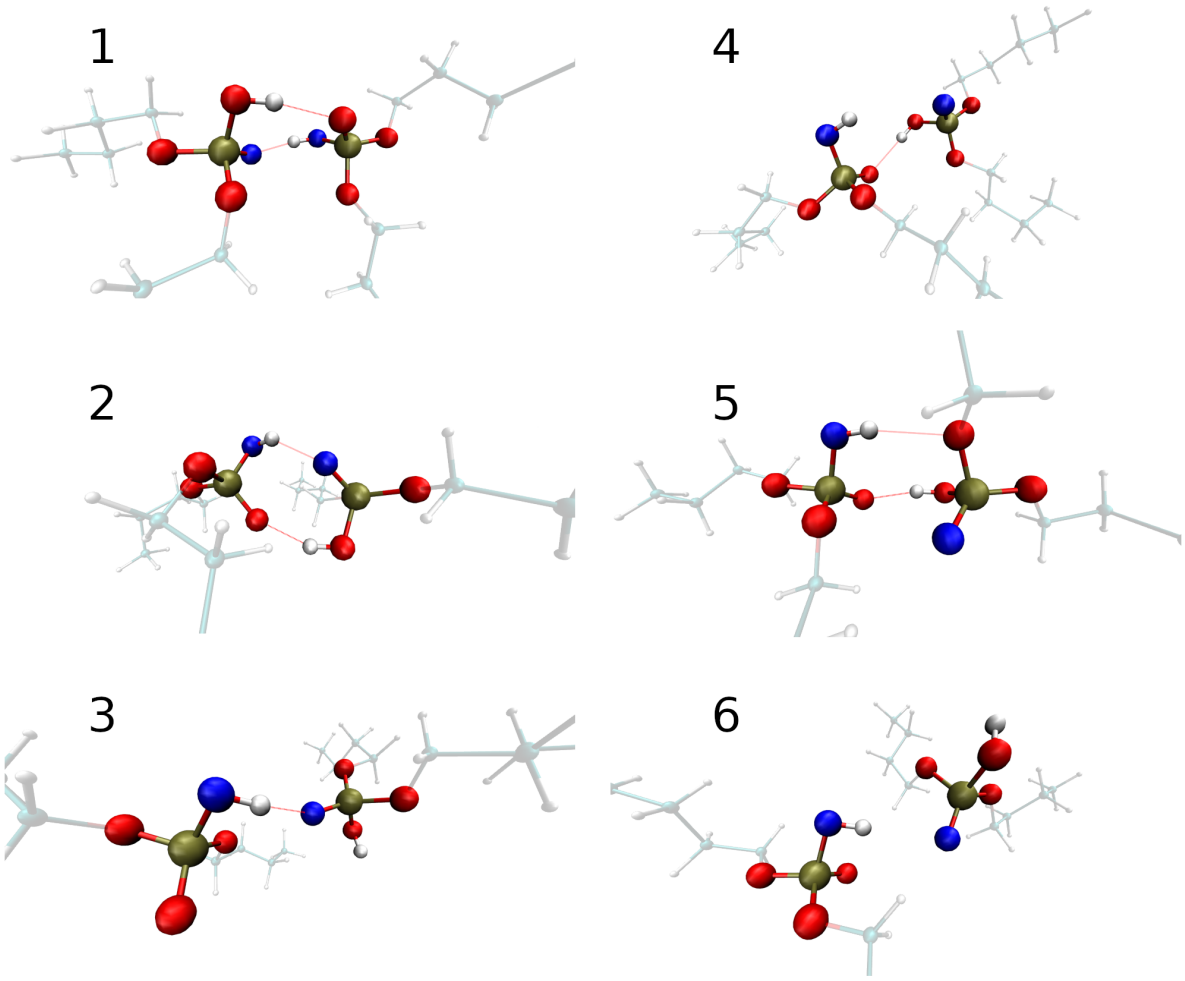

Figure 4.4: Typical conformations from the numbered regions of interest from the PMF shown in Figure 4.3. Blue atoms represents the umbrella constraint regulated DA pair. A red line represents a HB interaction. Only the PO_3OH core has been highlighted for clarity.

directly affect HB in the regulated pair. Directly left of this column shows an area of high free energy. This is attributed to VDW forces preventing close contact of atoms, prohibiting any sampling. Beyond 3 Å, an abrupt decrease in HBs is seen, as that is the HB cutoff.

The lowest free energy region of the PMF is contained within the column. This is sensible, as regions 1 and 2 are the only areas where the geometry of the umbrella

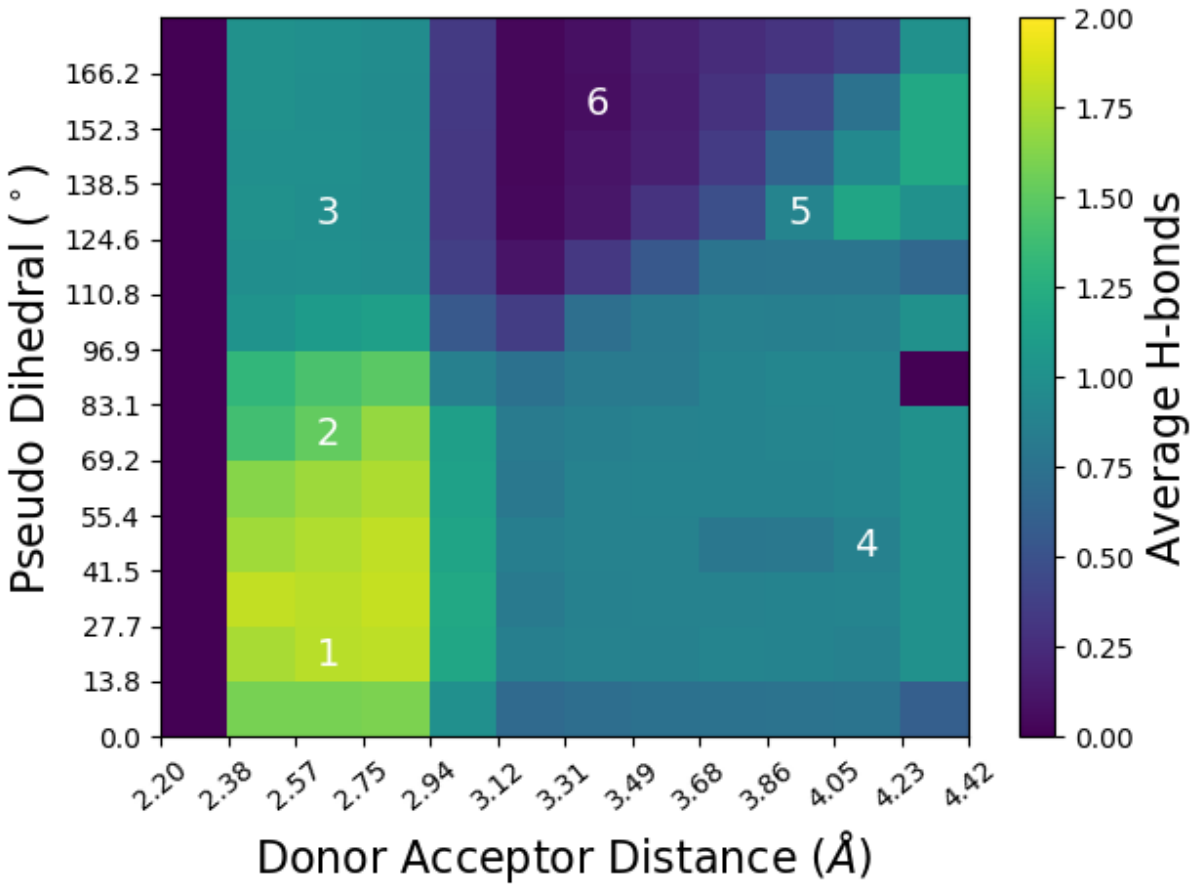

Figure 4.5: This heat map shows the average number of hydrogen bonds of sampled conformations as a function of reaction coordinate. The bins are identical to that of the PMF shown in Figure 4.3. The enumerated regions are also identical, and are provided for reference.

constraints allows for two HBs. However, the HB map in Figure 4.5 shows that the lowest free energy bins does not align with bins close to 2 HBs. Instead, it can be perceived that the center of mass of this centroid is shifted rightward compared to the low free energy region. While relaxing the HB distance and angle cutoffs captures more HBs within the column, it does not change the apparent center of the centroid. This suggests that the conformal geometry is by a small measure at odds with HB formation. Reasons for this will be discussed in Section 4.3.2, as the full scope of this cannot be understood without discussing solution simulations.

As the PDA increases within this column, so too does the DA distance of the unregulated pair. At 96.9° , the geometry completely disallows h-bonding. The free energy then levels off at 8 kcal/mol, which is coincidentally about the energy of one HB. An example of this geometry can be found in region 3. This leveling suggests that the pseudo dihedral angle itself matters less when it plays no role in HB formation.

Region 4 represents the furthest edge. The regulated DA pair is too far to h-bond, yet close enough to still interact electrically. The conformation here attempts to preserve the HB in the unregulated pair. In reference to the schematic diagram, Figure 4.2, each HDBP molecule rotates about the phosphorus atom in order to accommodate the proper distance. The bonding vector of the regulated phosphonyl and hydroxide become more parallel. This creates an unfavorable dipole-dipole interaction, and is thus slightly higher in free energy than region 3. The push back from the dipoles is likely also responsible for slightly diminished HB formation. If umbrella restraints were to be removed, there should be a reasonable expectation that the classic cyclic dimer would form. Further to the right of region 4 is an area of poor sampling. Umbrella restraints simulated this system only to 4 Å.

Region 5 represents a peculiar peninsula of moderately elevated stability. This conformation is similar to that of region 4 in that the regulated DA pair is too far away to be bound. But the PDA has flipped around until the regulated acceptor now interacts with the unregulated donor. Further, the regulated donor faces an ester oxygen. While this is energetically less favorable than two traditional HBs, it allows for both donors to interact, which is more favorable than leaving it free. Indeed, if only the phosphate core is viewed, without considerations of regulated pairs nor the alkyl tails, this conformation is not unlike that of low free energy states.

Region 6 is the only part of the PMF where both HBs are broken. It is also the highest free energy region with reliable sampling. The regulated DA distance is set too far to be h-

bonded. The PDA is similarly too high. The corresponding geometry prohibits h-bonding in the unregulated DA pair. The snapshot shown in Figure 4.4 may be representative of how two monomers begin dimerize when first coming into contact.

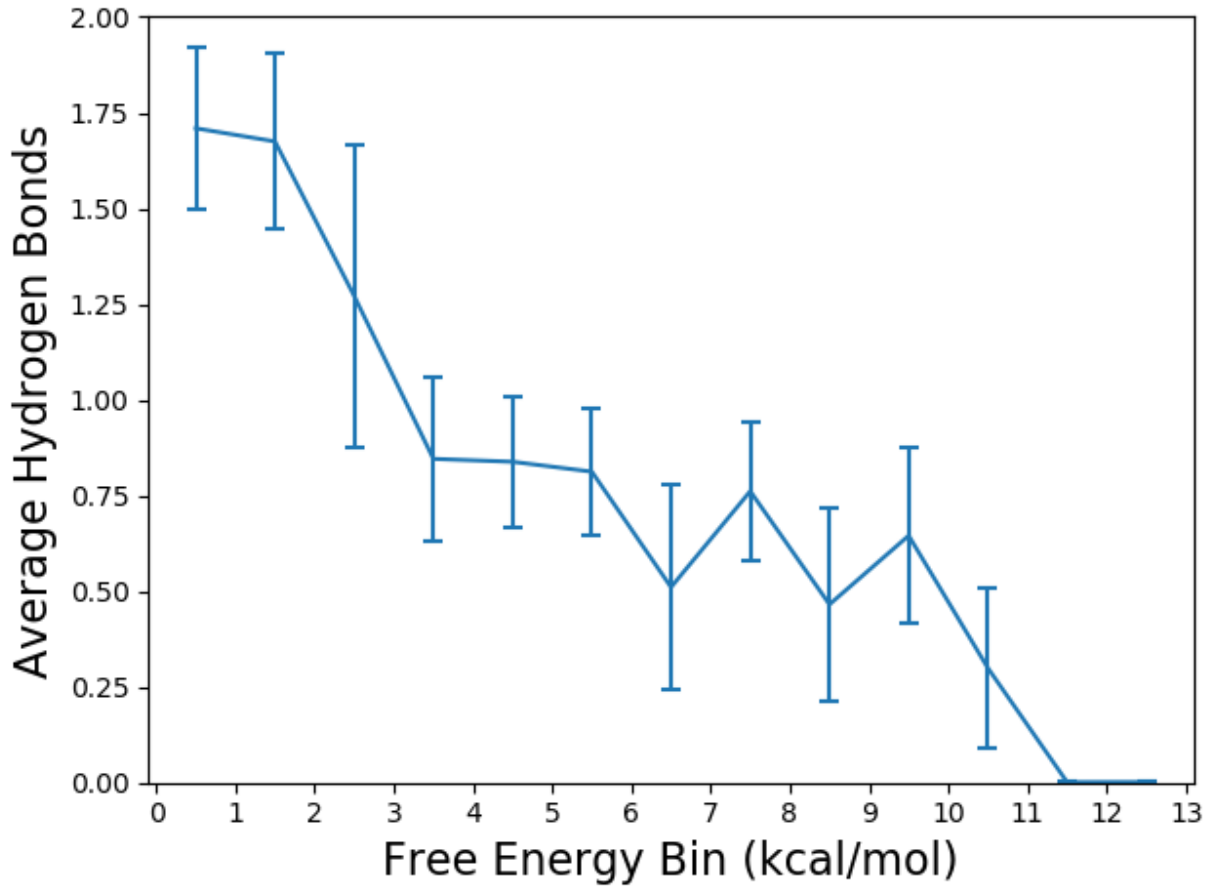

Figure 4.6: Shown is the average number of HBs formed across conformations within 1 kcal/mol increments. Three sections can be seen. Between 0 - 3 kcal/mol is a high negative slope. Then there is a flatter region between 3 - 9 kcal/mol. Finally, another steep slope between 9 - 13 kcal/mol, after which where HB formation breaks down completely.

Figure 4.6 shows the average HB formation across all conformations as a function of free energy, as calculated by the PMF. Three regions with distinct slopes can be seen. Between 0 - 3 kcal/mol, there is a steep drop off in HB formation. The length of this drop is slightly less than 1 HB. This is followed by a flatter region between 3 - 9 kcal/mol, where the difference is only 0.25 HBs. Past this is another steep region where HB formation breaks down completely at around 11 - 12 kcal/mol. This is in good agreement with a

previous study where, in the gas phase, the HB energy of a cyclic aggregate was found to be 13.74 kcal/mol[118]. Due to greater entropy, it is expected to be slightly reduced in the presence of solvent. It is worth noting that the previous study examined both monomer and dimer structures separately.

4.3.2 Solutions Simulations

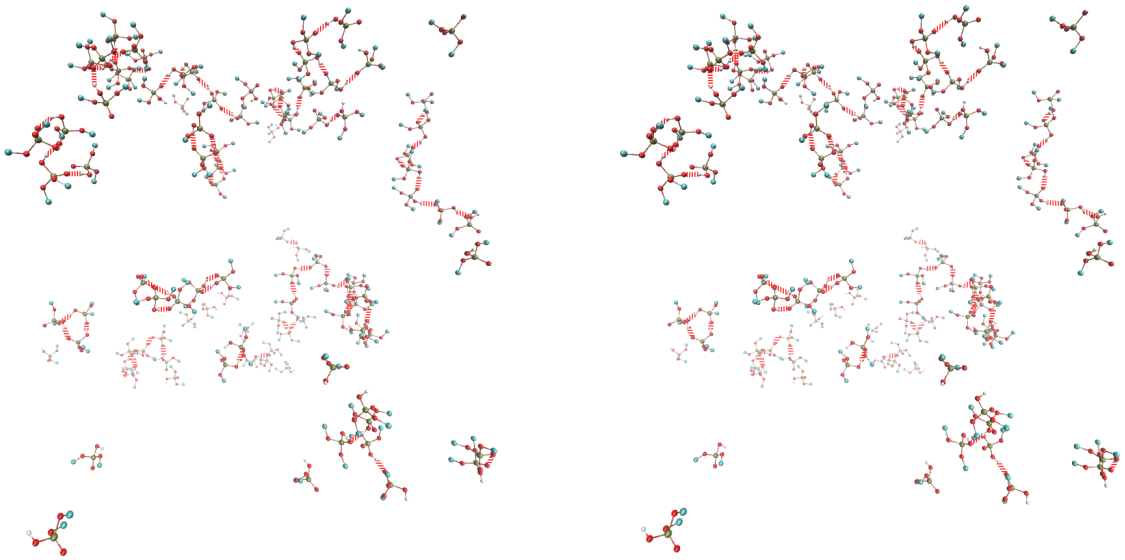

Figure 4.7: A steroscopic snapshot of a trajectory at 1000 mM. For clarity, only the PO_3OH core and the first carbon of the butyl tail has been displayed. HBs are represented as dashed red lines. Of note are the complex networks of HBs that are formed as aggregates diffuse through the bulk.

Shortly after the annealing phase, individual HDBP molecules collide and begin to form HB aggregates. Aggregates tend to remain stable as they diffuse through the bulk until they collide with other aggregates. Contact disrupts existing networks of bonds as DA pairs find new partners. This causes aggregates to combine, fragment, or poach molecules from one another. New HB formation is both hindered and facilitated by entropic forces. Such forces temporarily pop existing HBs off and back on. Occasionally,

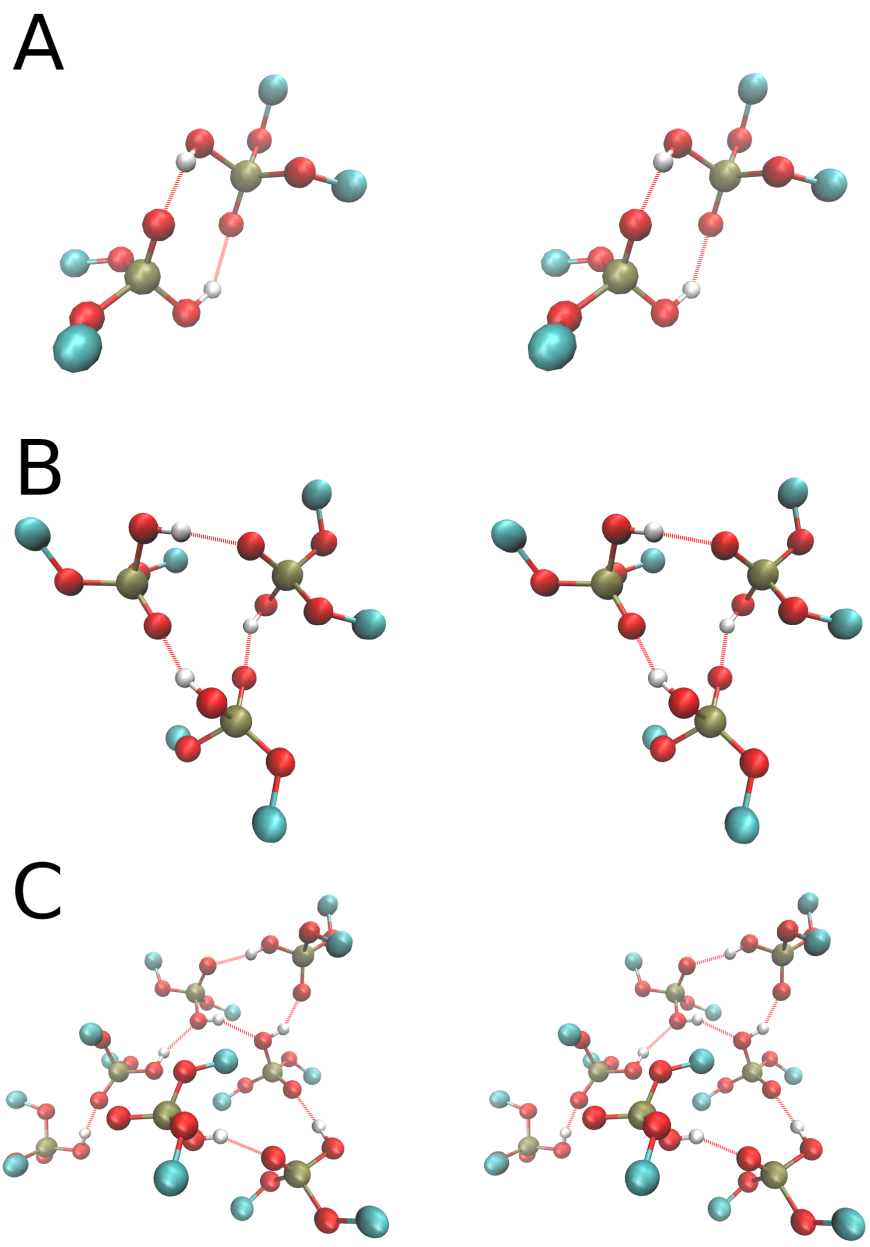

Figure 4.8: Steroscopic snapshots of different HB aggregate species. A shows a cyclic head-to-tail dimer, which is known in literature to be a common conformation. B shows a cyclic trimer, which was commonly observed. C shows a septimer displaying both linear and cyclic network topologies. Such large aggregates are not uncommon at higher concentrations.

it is enough to cause aggregates to fragment on their own. On the other hand, it is also what allows for the complex interactions between aggregates which leads to their growth.

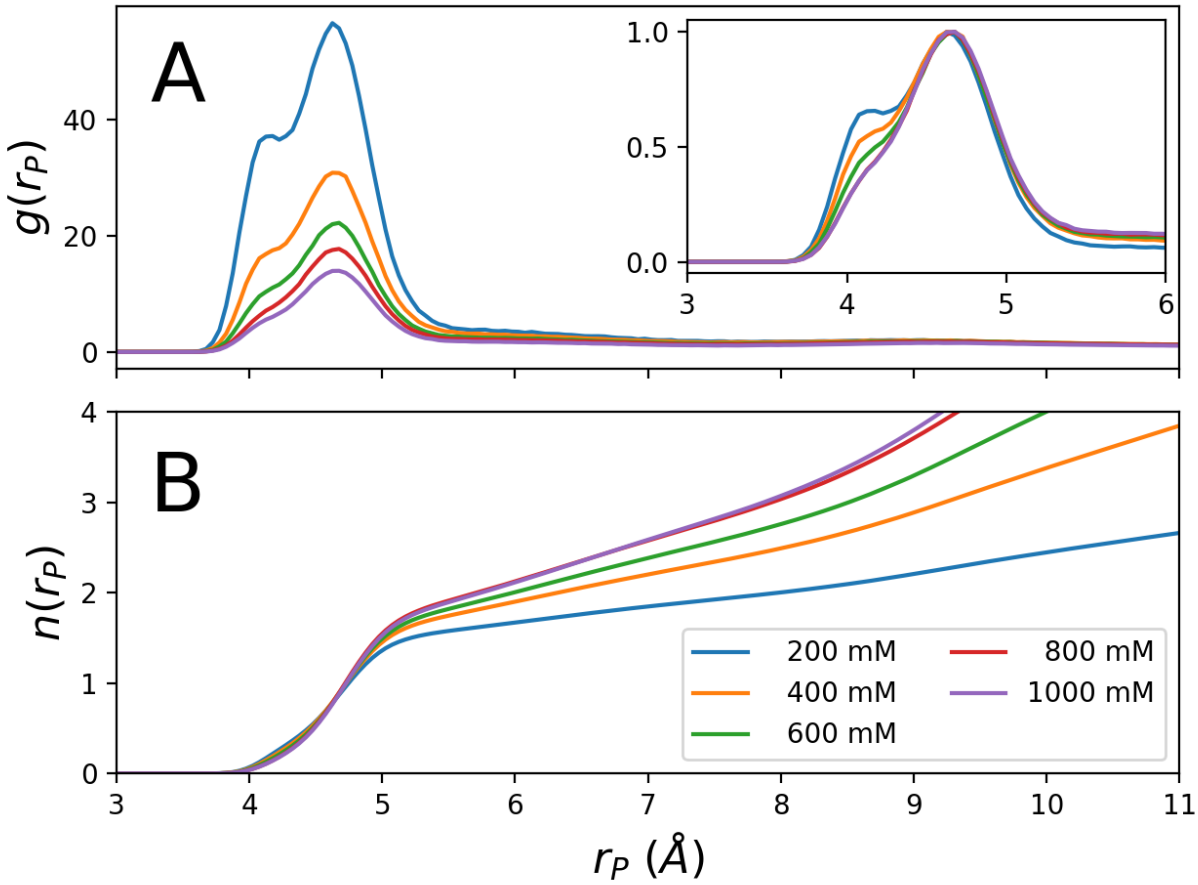

Figure 4.9: Figure A radial distribution function of phosphorus atoms. The inset figure shows the same data, but has been peak normalized. Figure B shows the coordination number as calculated by integrating Figure A. The left most shoulder represents the distance between phosphorus atoms within cyclic dimers. The main peak, centered around 4.6 Å, represents other nearest neighbor interactions.

Figure 4.7 shows a snapshot of this equilibrium state of HDBP in a non-polar solvent, taken at 1000 mM. A variety of structures can be observed. Figure 4.8 shows snapshots of three individual aggregate species. Seen is a mix of HB linear chains and closed loops, These will be discussed in this section.

Figure 4.9A shows radial distribution functions (RDF) as a function of concentration. The overall peak heights here are related to concentration. As individual aggregates become more sparsely distributed, any long range structures become less probable in relation to close aggregates. Thus, at lower concentrations, peaks due to close aggregate

Concentration (mM)	Coordination number
200	1.58
400	1.76
600	1.83
800	1.91
1000	1.92

Table 4.1: Coordination number of HDBP in dodecane

structures will disproportionately dominate the RDF more than the aperiodic oscillations that decay to one, which represents the rest of the bulk. The inset in Figure 4.9A shows the same data peak normalized in order to exaggerate changes in close aggregate structures as a function of concentration. The first peak at 4.1 Å represents head-to-tail cyclic dimers. The second peak at 4.6 Å represents HB nearest neighbors in other conformations. The inset shows that the first peak diminishes as concentration increases. This suggests that cyclic dimers do not survive as the environment becomes more crowded. Aside from this, no significant changes in behavior is seen across this set of concentrations. Further, it is interesting that the cyclic dimer, while prevalent, does not seem to be the dominating conformation in solution across all simulations.

Figure 4.9B shows the distribution of molecules around another as calculated by integrating the RDF. Typically, the coordination number (CN) is considered to be the integral of the first peak, which is the first coordination sphere. This can be considered to extend out to 5.5 Å for these systems, as it is appropriate to include both the left shoulder and the primary peak, since both features are HB structures. The corresponding coordination numbers for each concentrations is shown in Table 4.1.

Notably, the coordination number never goes above 2. This would suggest that any sort of phase transformation phenomenon is impossible in these studied systems. This should make intuitive sense since it is observed that HDBP would form cyclic dimers and linear chains. Molecules in cyclic dimers are 1 coordinated. The average coordination

in linear chains is 2 only at the limit of an infinitely long chain. Since both aggregate species exist in meaningful concentrations, the average coordination should be less than two. Considering HBs with off oxygens as acceptors, such as the ester oxygens, does open up the complexity somewhat. In Figure 4.8C, we see a septimer where an acceptor atom has latched onto the back side of another acceptor. However, recalling discussion from Section 4.3.1, such interactions are 9 kcal/mol more unfavorable than with the classic double bonded oxygen as the acceptor. While observed, these interactions do little to increase the coordination above 2. A CN this low makes it unlikely to form percolating aggregates, discounting the production of highly intraconnected structures such as reverse micelles[55]. Further, it would explain why reverse micelles are only seen in the presence of an aqueous phase

In later analysis, it is assumed that HB is the only mechanism of aggregation. Dipole-dipole interactions may exist, but are expected to be magnitudes less significant. It can be seen that, from the RDF in Figure 4.9, this is predominantly true. This is evidenced by the lack of any structure in the RDF beyond the immediate HB coordination sphere.

Figure 4.10A shows the relative concentration of all molecular species observed in solution. Figure 4.10B is the probability an individual HDBP molecule exists within an aggregate of size n. Figure 4.10C shows the free energy as a function of n. The most notable feature is the high free energy of the monomer, which is off scale at 30 kcal/mol. This is much beyond the energy of two HBs, as discussed in the previous section. Its disproportionately high energy can be owed to both its small probability and its high potential energy due to a lack of any HB interactions. While the concentration of monomers may seem high despite its free energy, it should be noted that most monomers are transient objects induced by entropy. True loners were not readily observed. They are long lived only at 200 mM, as the mean free path of aggregates is large.

On the other end of the spectrum are large scale aggregates which, at higher con-

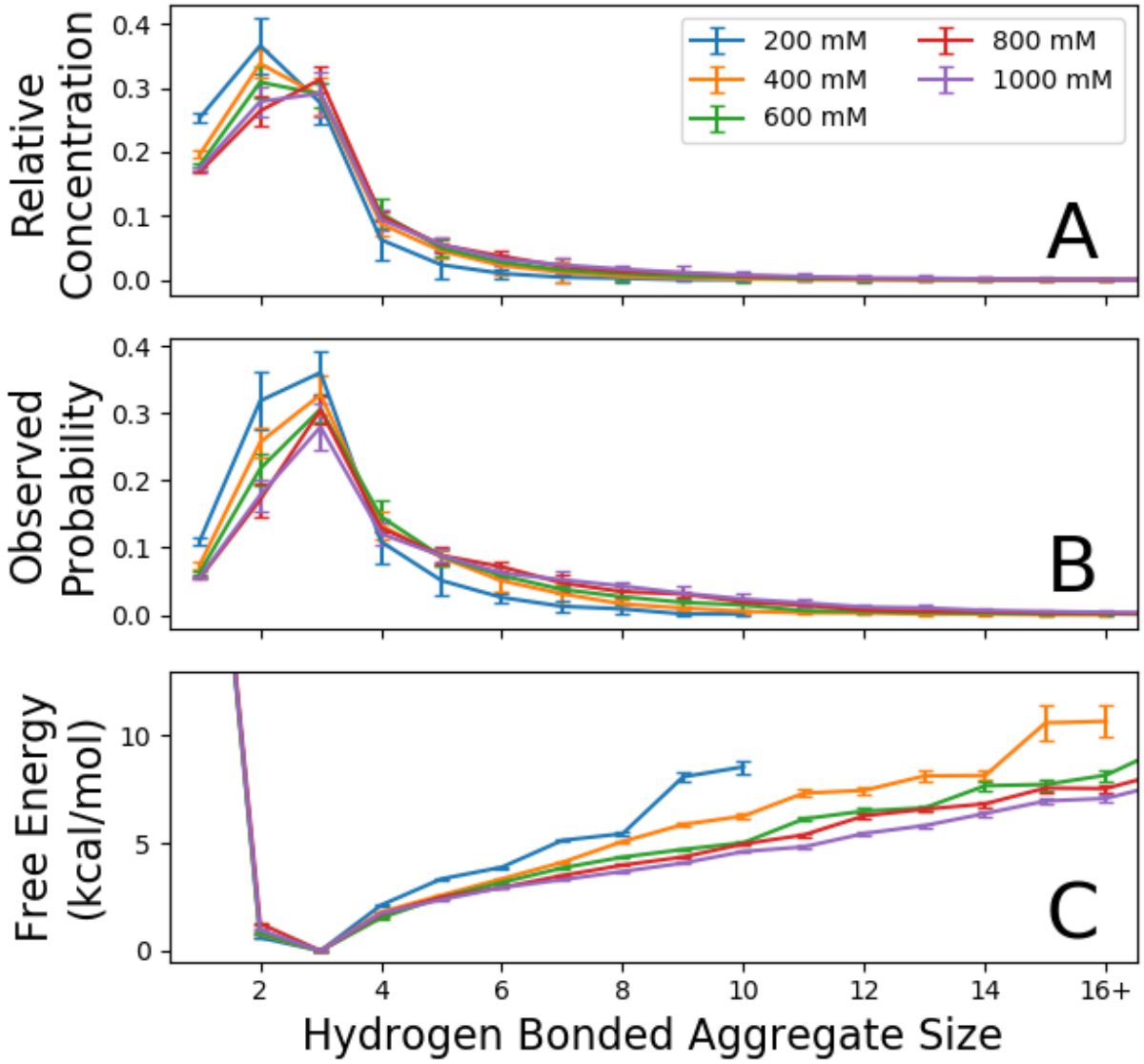

Figure 4.10: Figure A shows the relative concentration of aggregate species. Figure B shows the observed probability that an individual HDBP molecule exists as part of a h-bonded aggregate of size n, as observed in solution. Figure C shows the corresponding free energy as a function of size. The free energy of the monomer, which is off the chart, was measured to be around 30 kcal/mol for all concentrations.

centrations, can be greater than 16 molecules. Their relative instability is owed to their unwieldy nature. Occasionally, large aggregates will fold into themselves. The intra-aggregate contact may cause it to fragment into smaller pieces. Additionally, a large size means a smaller mean free path. While this gives more opportunities for aggregate

growth, it also makes larger aggregates unstable. This effect is more pronounced as the concentration increases.

Of particular interest is the abundance of trimers as opposed to dimers. Across all concentrations, it appears likelier for HDBP molecules to form trimers. This correlates with data shown in Figure4.9A. We also see that the corresponding free energy for the trimer is lower by about 1 kcal/mol. As mentioned in the introduction, various works have suggested that HDBP in a non-polar solvent should exist as a cyclic dimer. The reasoning is that the cyclic structure minimizes the potential energy by creating the maximum theoretical amount of HBS possible. It is technically true that, at below 800mM, dimers are the most populous of aggregate species. This study also agrees that the free energy of the cyclic dimer is lower than the linear dimer. However, the story does seem to complicate somewhat in solution.

There are several clues as to why trimers are more favorable than dimers. Figure 4.11 shows the measure of average HBs formed per molecule as a function of n. Aggregates that are linear chains would have one fewer HB than is the theoretical maximum of one per molecule. If all aggregates were perfectly linear, then this graph would follow a $(n-1)/n$ trend. However, at all values of n, the true values are above this. This is because the HB network topologies of aggregates often possess circuits. Either the entire aggregate itself is a ring, or there is a ring structure with a linear chain branching off of it. Structures such as this often have free donors and no free acceptors, or vice versa. This inflates the average HBs per molecule above $(n-1)/n$.

At $n = 3$, there is an up-tick in HB formation that goes beyond the greater trend. This is because trimers particularly favor the cyclic conformation as opposed to linear ones. Figure 4.12 shows that this is indeed the case. Displayed here is the fraction of aggregates of size n which was observed to exist in the cyclic conformation. Interestingly, the classic head-to-tail cyclic conformation is less than 50% of observed dimers. The presence of

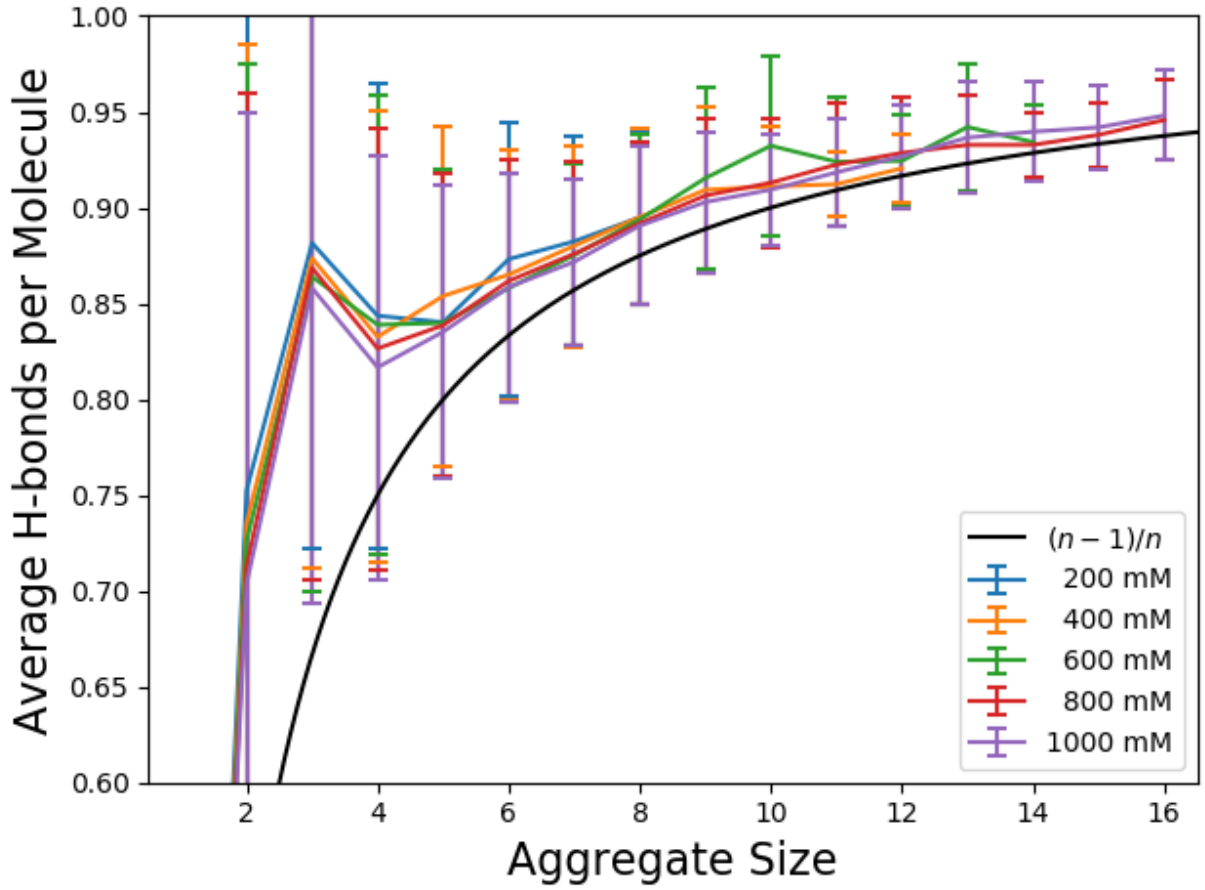

Figure 4.11: Average HBs per molecule is plotted as a function of aggregate size. A value of 1 would mean that all theoretically possible HBs are formed. If no ring structures were present, this trend should follow $(n-1)/n$, which is also shown. However, the true values are instead elevated. The spike at $n = 3$ shows a particular preference for trimers to be in a cyclic conformation. High uncertainties are expected at lower values of n, as a difference of 1 represents a significant fraction of a small number.

cyclic dimers further diminishes as the concentration increases. Since the concentration of all dimers is already decreasing with increasing HDBP concentration, the effect of on cyclic dimers is quite pronounced. Meanwhile, the cyclic trimer is slightly less sensitive to this. With increasing HDBP concentration, it diminishes by around 5%, while also the total population of trimers is increasing. All this suggests that the HB network in the cyclic trimer is somehow more resilient to entropic degradation than other aggregate types.

Figure 4.13 gives insight as to why this is so. Shown are a series of two dimensional

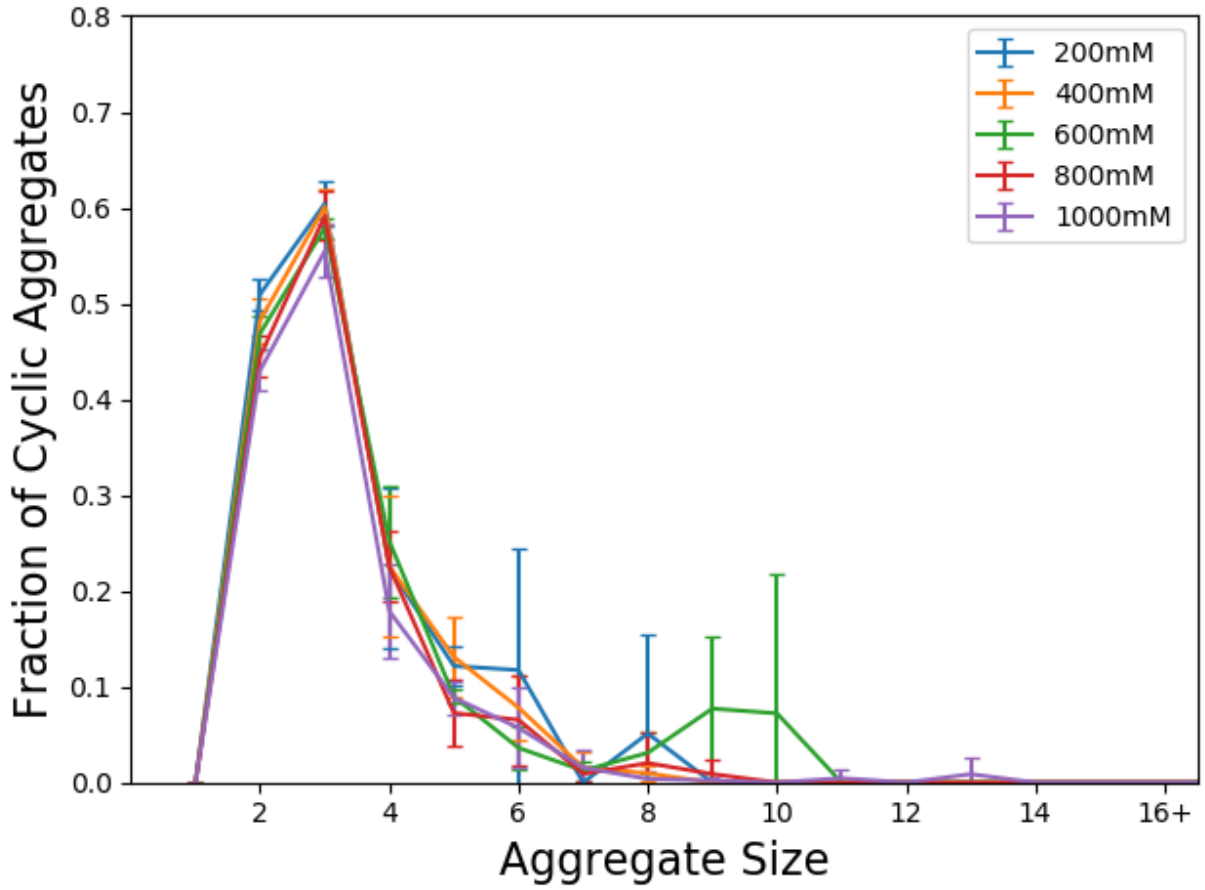

Figure 4.12: Shown is the fraction of aggregates of size n that are cyclic. A value of 1 would mean that all aggregates form a single ring made up of n HDBP molecules. Aggregates with ring structures that are merely features of the topology were not considered to be cyclic.

histograms of the DA angles and distances of all DA pairs. They have been separated out from linear and cyclic type aggregates and by size. No differences were observed across concentrations, and thus are summed over. Generally, the centroid of these histograms is centered between 160 and 170 degrees. But cyclic dimers shows a looser grouping, and have their centroid center pushed down by about 5 degrees. The significance here is that DA atoms in the cyclic dimer are less likely to face each other head on, leading to slightly less favorable hydrogen bonds interactions. This strength of this effect would be on the order of tenths of kcal, whereas HBs are about 7. Therefore, dimers will readily sacrifice some favorability in its own geometry to form the cyclic shape.

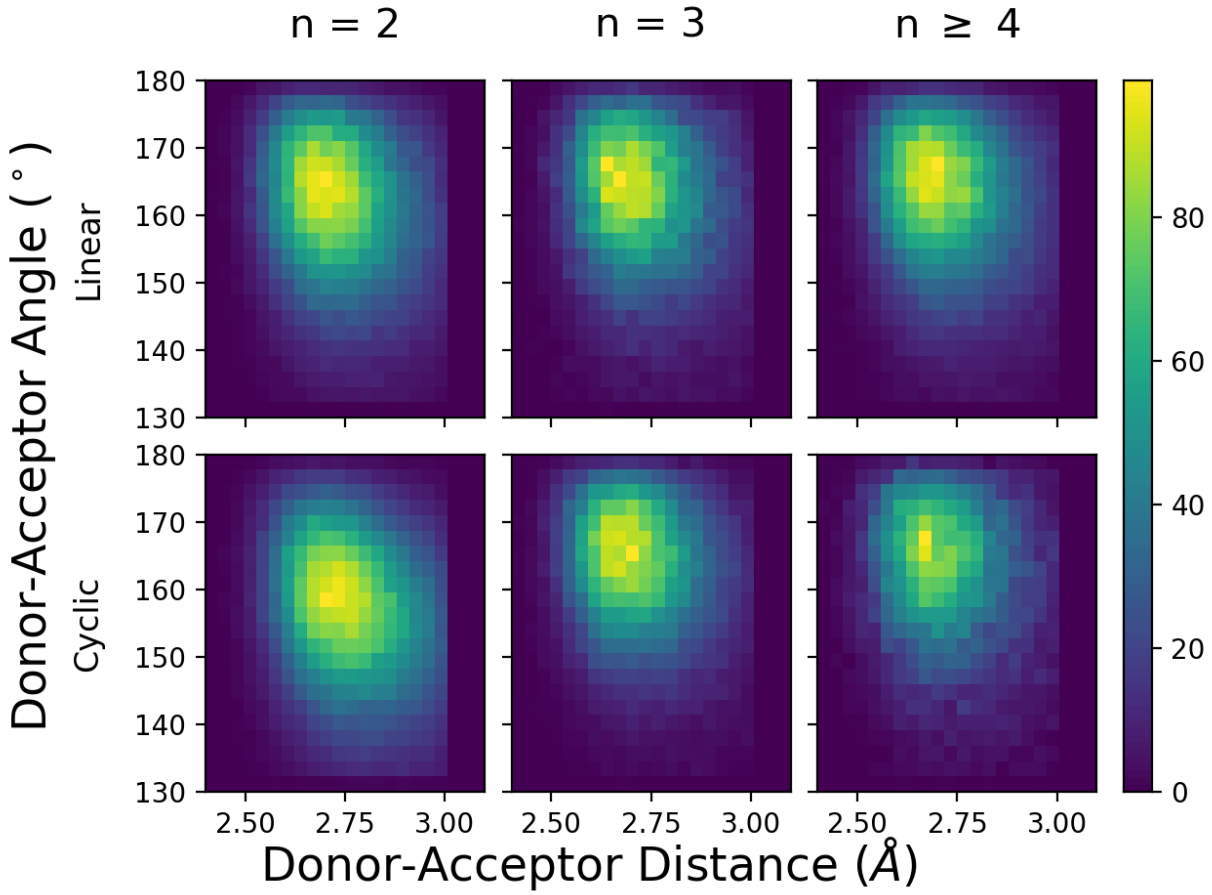

Figure 4.13: Two dimensional histograms of DA angles and distance of all hydrogen bonds within observed aggregates. In most cases, the centroid of the histograms are centered around 160 to 170 degrees, save for $n = 2$ cyclic aggregates. The center of the centroid there is about 5 degrees lower. This means that acceptor oxygens in cyclic dimers are slightly less likely to face their donor head on, leading to a slightly less favorable interaction. No difference is seen across concentrations, and thus have been summed together. The same is true for $n \geq 4$.

This ties back to an idea presented in Section 4.3.1. There it was mentioned that HB formation in the cyclic dimer is by some small measure fighting against its own geometry. It is perhaps because the cyclic dimer is too inflexible. It could be imagined that HBs are swivels which allow HDBP molecules to twist relative to each other about the HB axis. In linear aggregates, these swivels are free to adopt low energy conformations. But two swivels meeting head to toe constrains the geometry. When there are three or more, there is enough flexibility such that the HB that closes the loop does not constrain movement.

There are enough swivels to allow molecules to find favorable bonding angles. However, having more than three bonds may introduce too much flexibility, leaving the structure prone to entropic perturbation.

Flexibility is necessary because the classic head-to-tail dimer, as drawn schematically in Figure 4.2, is somewhat misleading. To reiterate an argument made in a previous work[118], the tetrahedral angle is 109.5° . As it is drawn in Figure 4.2, the P-O-H angle would have to be 125.25° , whereas that angle in phosphates is typically around 90-110° . Cyclic trimers seem to readily take into account all of these geometric considerations while being compact enough to preserve itself from fluctuations. This would explain why trimers are overall lower in free energy than all others.

4.4 Conclusion

A PMF study was undertaken to study the stability and breakdown of HBs in a cyclic HDBP dimer. This study is in good agreement with previous works which describe the cyclic dimer to be a meta-stable state. By tuning umbrella constraints to specifically pull apart both dimers, new insight was gained regarding this meta-stable state. Further, it was calculated that the energy difference between two monomers and a cyclic dimer in solution is around 11-12 kcal/mol, which is also in good agreement with previous works.

Simulations of HDBP in n-dodecane were successfully performed. Concentrations ranged from 200 mM to 1000 mM, in 200 mM increments. HB criteria from a previous work was applied to these simulations in order to study aggregation phenomenon. This work proposes the presence of large scale HDBP aggregates in solution. While such complex networks of HB aggregates were observed, their low coordination number suggests they are not complex enough to form highly intraconnected structures such as reverse micelles.

Aggregate species were characterized by their geometry and relative free energies. This analysis showed that, against conventional wisdom on the topic of HDBP aggregation, it the cyclic trimer is more energetically favorable than the cyclic dimer.

Chapter 5

Phase Transitions in HDBP

5.1 Introduction

Previous discussions have highlighted the presence of large scale close aggregates in a non-polar diluent. It has been shown that, as the local environment surrounding an HDBP molecule becomes more crowded, larger scale aggregates form. However positronium annihilation studies suggest some sort of phase transition occurring at concentrations lower than the ones that have already been simulated[117]. As it is yet unclear what this transition may represent, additional simulations at low concentrations have been performed.

This work can be considered to be a continuation of Chapter 4. This chapter will discuss observations of HDBP at more dilute concentrations. Two new simulations of HDBP at 50 and 100 mM have been performed and analyzed. These are then compared with results from Chapter 4 to get a clearer picture of the effect of concentration on aggregate formation.

5.2 Methods

5.2.1 Simulation Setup

Simulation details are similar to that of previous works[118]. But in brief, all simulations were performed on a local computing cluster with Amber14[77] using PMEMDCUDA[96, 97]. Electrostatic cutoffs were set to 10 Å with SHAKE restrained hydrogens with a tolerance set to 10^{-7}. Center of mass dampening occurred every 1 ps. Similar to simulations in Chapter 4, systems were put through an extended annealing phase before equilibration. Temperature was maintained hot enough to break apart close aggregates. A long equilibration phase then followed. Sampling occurred at STP in the micro-canonical ensemble

at an interval of 40 ps.

Initial structures were generated using Packmol[98] by first initializing with solute, then adding dodecane until the concentration of extractant reached the desired value. The 100 mM simulation used 50 HDBP molecules and 2158 dodecane molecules. The 50 mM simulation used 25, and 2179 HDBP and dodecane molecules respectively. Previous simulations used 100 HDBP molecules across all simulations, but were reduced for these simulation sets to economize available computational resources. Greater uncertainty should be expected when compared to previous simulations, but was offset with a longer sampling time. For the mixed simulations, a total of 100 TBP and HDBP molecules were used for each simulation, adjusting the fraction of each in increments of 25%, for a total of 5 simulation sets. 354, 349, 343, 337, and 331 molecules of solvent were used, from 0% TBP to 100% TBP respectively. FFs for TBP, HDBP, and dodecane were developed in previous works[60, 118]. Analysis was performed using Python[104, 105] and Pytraj[101, 100]. Network analysis code to identify aggregates was described in Chapter 4. Diffusion calculations are described in Chapter 3

5.3 Results

5.3.1 HDBP at low concentrations

Data from Chapter 4 are included in order to aid in direct comparison. But only the 200 and 400 mM simulation sets will be included in order to preserve clarity of figures. In all comparisons shown in this section, trends are generally linearly related to concentration, as will be discussed.

Figure 5.1A shows the radial distribution function of phosphorus atoms in solu-

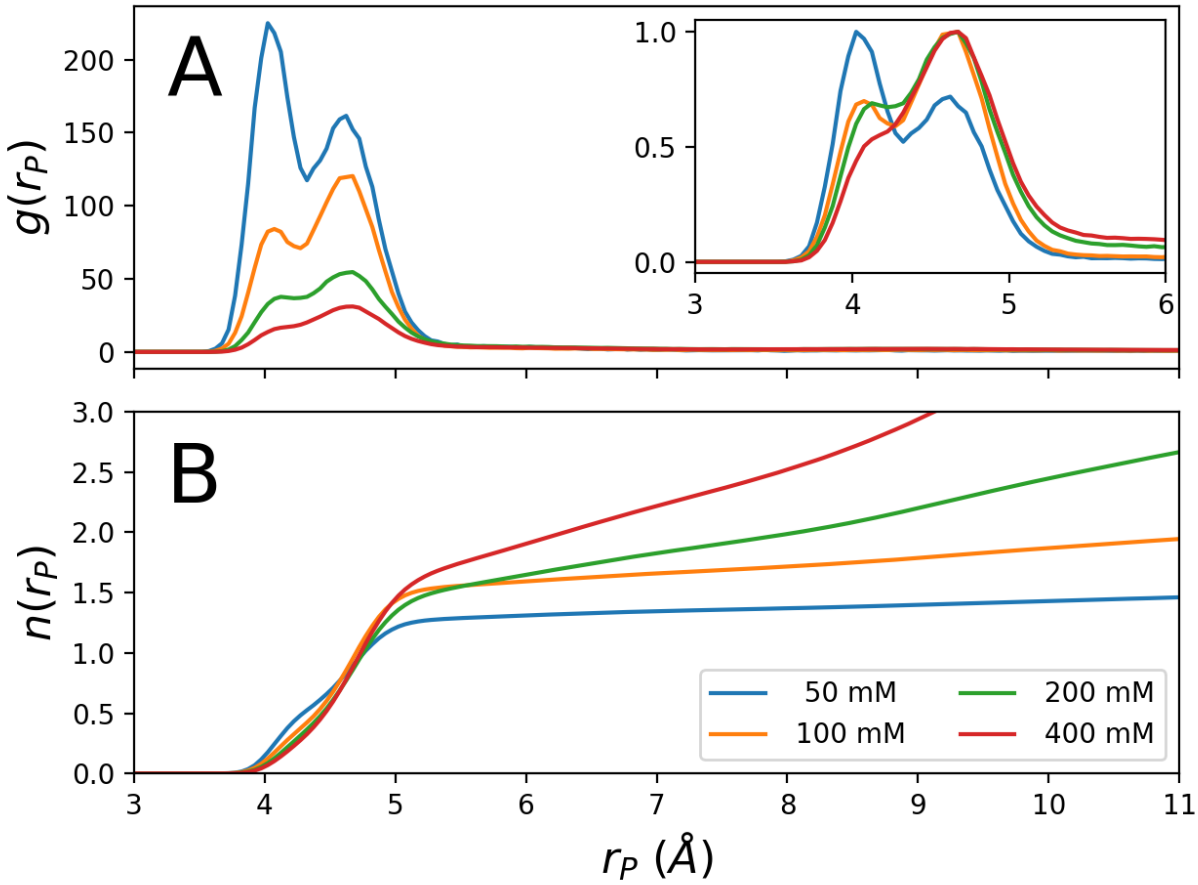

Figure 5.1: Figure A shows the radial distribution function of phosphorus atoms. The inset zooms into the peaks, which have also been peak normalized to exaggerate differences in structure. Figure B shows the coordination as a function of radius as calculated from the RDF.

tion. To reiterate results from Chapter 4, with increasing concentration, the first peak diminishes, and the second peak grows. The first peak represents molecules in the cyclic head-to-tail conformation. The second peak represents all other hydrogen bonded nearest neighbors. The overall height of the peaks is related to the sparseness of HDBP molecules. The significant relation is the growth of the first peak at 50 mM. Across all simulated concentrations, this is the only one which exhibits cyclic dimers as the primary aggregate species. It is then sensible to see that, in Figure 5.1B, the coordination number at 50 mM is well below 2. The most common aggregate species is only 1 coordinated.

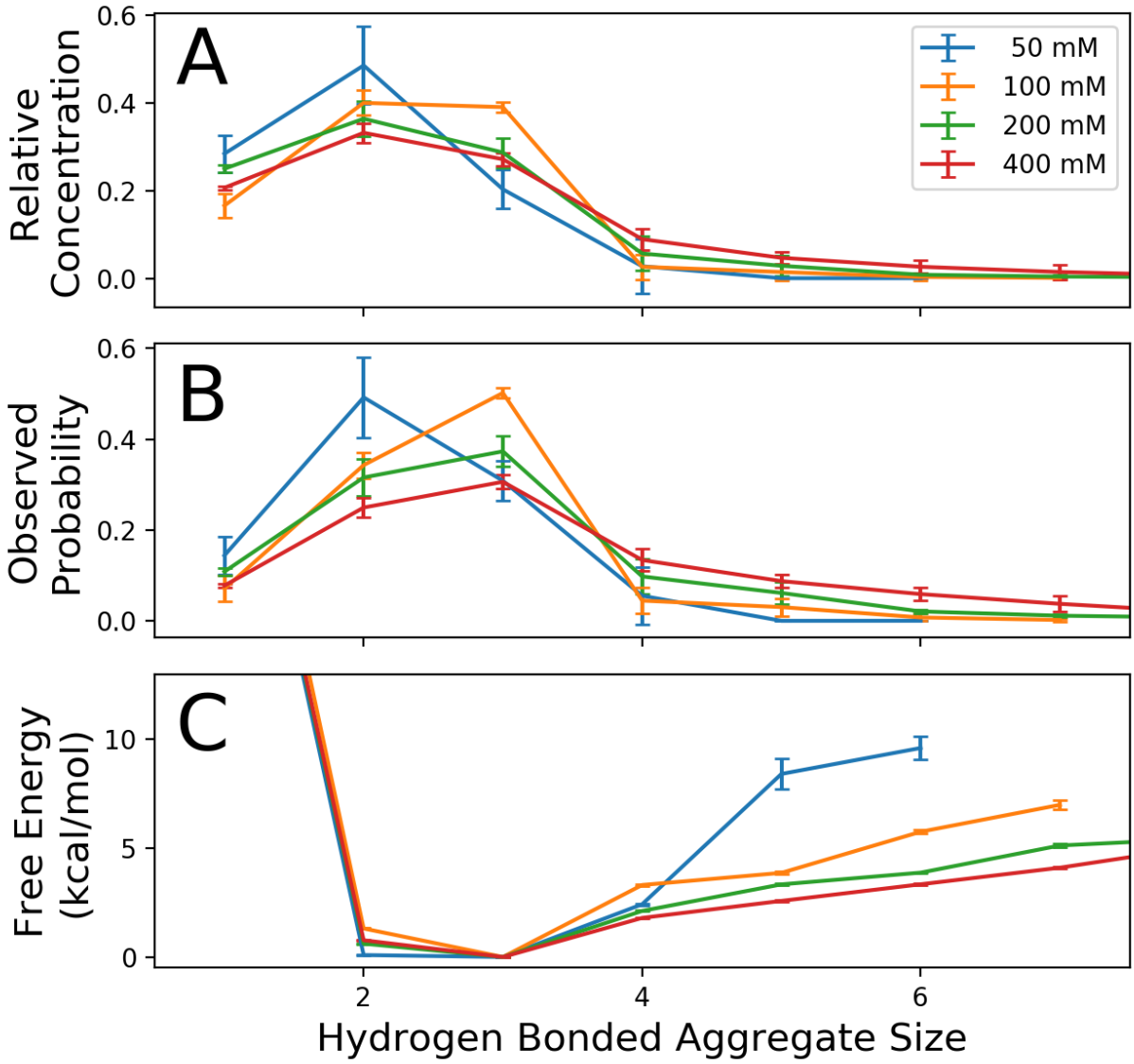

Figure 5.2: Figure A shows the relative concentration of aggregate species as a function of size and concentration. Figure B is the probability that an individual molecule exists in an aggregate of size n. Figure C is the free energy associated with each aggregate species.

HB network analysis confirms this. Figure 5.2A shows the relative concentrations of aggregates in solution. Figure 5.2B shows the probability that an individual molecule of HDBP is part of an HB aggregate of size n. It is worth noting that, across 200 mM to 1000 mM, the overall shape of these curves remained constant, only flattening somewhat to account for large aggregates. But the low concentration solutions show some interesting behavior. At 100 mM, an insignificant number of aggregates of $n > 3$ were observed. At

50 mM, the dimer suddenly becomes the most common species of aggregate. Free energy calculations, which can be seen in 5.2C, show little meaningful changes in trends until 50 mM. Here, the free energy of higher order aggregates increases sharply beyond $n > 4$. Additionally, the free energy of the dimer matches that of the trimer, which, as a reminder, minimizes conformal energy more than the cyclic dimer.

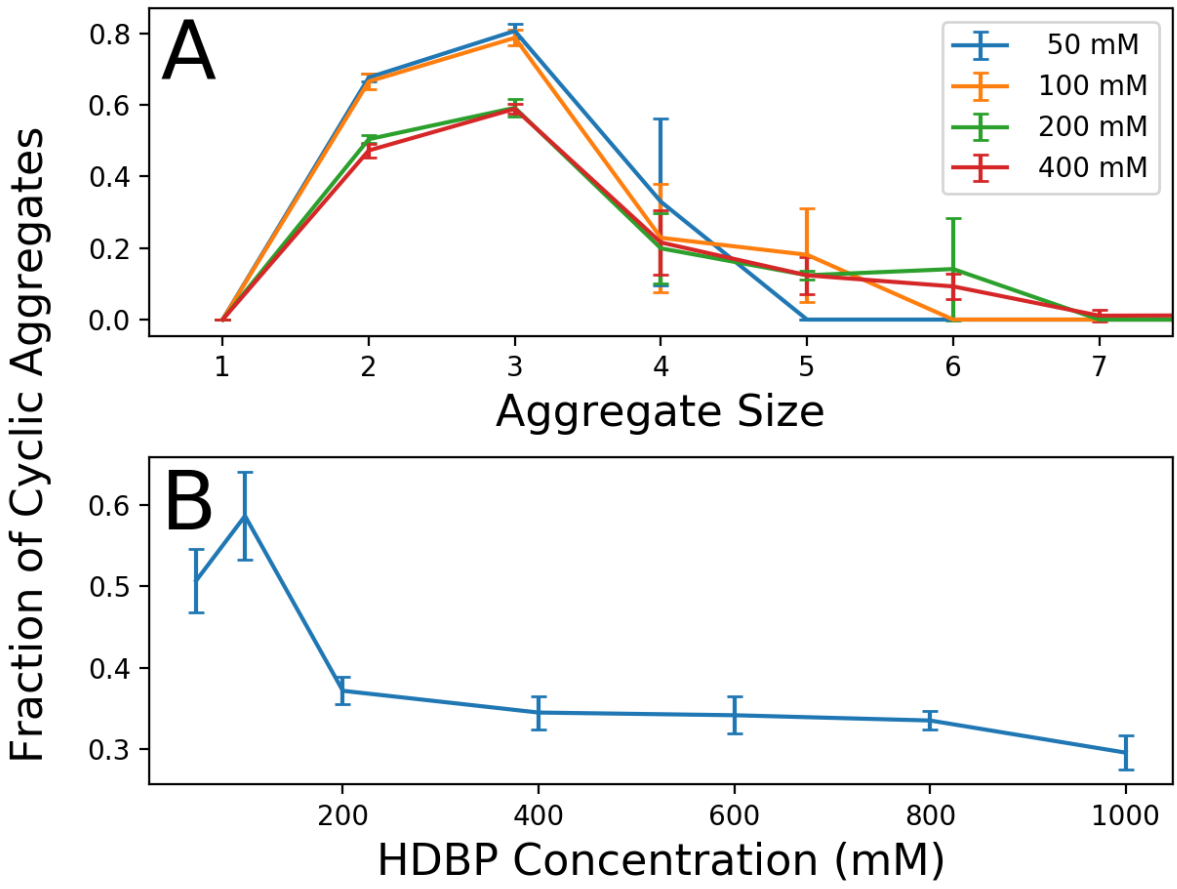

Figure 5.3: Figure A shows the proportion of aggregate species which are cyclic. Figure B shows the total proportion of cyclic aggregates in solution. At concentrations of 50 and 100 mM, greater proportions of aggregates are of the cyclic conformation.

Upon closer examination of the network of HBs at low concentrations, more important distinguishing features arise. Figure 5.3A shows the fraction of aggregate species which are cyclical as a function of size. Figure 5.3B shows this data across all species as a function of concentration. Between 200 - 1000 mM, no particular trend arises. The

amount of cyclic aggregates remains mostly constant, perhaps slightly decreasing as the local environments of aggregates becomes more crowded. But there is an abrupt increase at low concentrations. The relative occurrence of cyclic aggregates are 10% higher at 50 and 100 mM compared to 200 mM and above. This represents a significant change in the behavior of HDBP.

It is possible is that, at low concentrations, the distribution of aggregates is sufficiently sparse as to allow it to relax into low free energy conformations. In Chapter 4, it was seen that higher order aggregates are more likely with increasing concentration. This can be attributed to more collisions between molecules. Increasing concentration creates greater opportunities for aggregates to add to their mass. On the other hand, constant bombardment creates a situation where aggregate species are in flux, prohibiting relaxation into low free energy states. Further, larger aggregates, with their high free energy, are likely to split themselves into smaller ones.

Concentration (mM)	Diffusivity $Å^2$ / ns
50	52.26 ± 4.34
100	48.47 ± 4.67
200	48.82 ± 6.07
400	35.75 ± 3.50
600	40.76 ± 4.11
800	27.71 ± 1.72
1000	28.25 ± 3.15

Table 5.1: Diffusivity of HDBP in dodecane

However, the number of collisions as a function of concentration should be linear in dilute systems. Indeed, this can be seen in Figure 5.4. Figure 5.4 A shows the mean square displacement across all simulated concentrations from 50 to 1000 mM. Figure 5.4 B shows the calculated diffusivity as a function of concentration. This data is also shown in Table 5.1. As expected, the changes in diffusivity is linear across this range. Because all simulations occur at the same temperature, the average thermal velocity of molecules

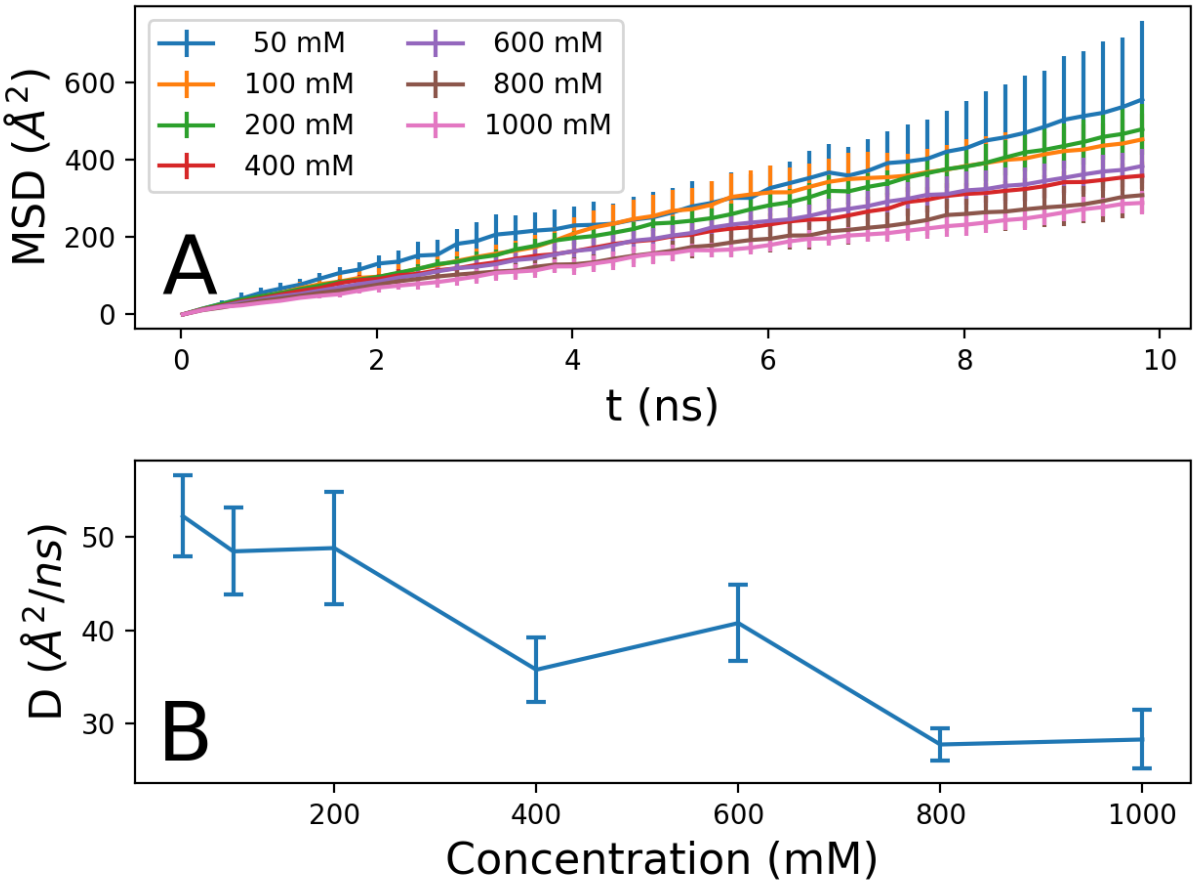

Figure 5.4: Figure A shows mean square displacement of individual HDBP molecules over 10 ns. Figure B shows the calculated diffusivity. All simulated concentrations are shown.

are constant. What must be changing is therefore the mean free path of aggregates, ergo the time between collisions. The assertion is then that somewhere around 100 mM lies a transition point where the mean relaxation time of newly formed aggregates becomes smaller than the time between collisions.

5.4 Conclusion

While HB is a consequence of electrostatics, it is not to say that it is an attractive force between HDBP molecules. Formation of aggregates first requires that molecules come

into close contact with each other, the rate of which will depend on concentration. Across this and the previous chapters, distributions of aggregate species have been profiled as a function of concentration. At 200 mM and above, cyclic trimers were seen to be the most prevalent species. However, below this, prevalent conformations switch to cyclic dimers. This seems to be in line with trends seen in radial distribution functions. Unfortunately, additional study will be required to examine why this is so.

Further, network analysis has shown that, at low concentrations, a higher percentage of all aggregate species are cyclic, compared to that of simulations at higher concentrations. An abrupt jump signifies some fundamental difference between low and high concentrations. Analysis of diffusivity have shown a linear trend in the studied range of concentrations. This signifies that nothing particularly interesting is happening in the movement of HDBP itself. Therefore, the transition must lie within something else. This work proposes that this transition is related to the relaxation time of newly formed aggregates. Additional study may be required for confirmation. The design of such studies will be discussed in Section 6.2.1.

Chapter 6

Concluding Remarks

6.1 Conclusion

Aggregation of extractants are an important factor that effects the selectiveness and efficiency of SX processes. Thus, this dissertation focused itself on the examination of HDBP which, with its OH head, will form hydrogen bonded aggregates.

With this information at hand, the new HDBP FF was developed and validated against several key critical properties. It has been reparameterized to better match density, dipole moment, and an estimated value for heat of vaporization to a maximum error of 3.8%. While the heat of vaporization had to be estimated, all other values fell within experimental uncertainties. This is a significant improvement over the default GAFF parameters for HDBP, which had a maximum error of 20.85%. The new FF was validated against the self diffusion coefficient and matched to within 18% of literature values. This is much improved over the 67% mismatch with the default.

Two PMF studies were undertaken with this new force field. Each served to study the cyclic head-to-tail hydrogen bonded dimer, which is the suggested conformation of HDBP in dilute solutions. One studies this conformation directly, while the other attempted to break both hydrogen bonds in this conformation. Both PMF studies have confirm that this structure is a meta-stable state. Further, specific geometric details regarding this conformation have been obtained.

These geometric details were useful in understanding simulations of solutions of HDBP, and a concentration dependence on the distribution of aggregate types and sizes were found. These solutions ranged from dilute to highly concentrated. At dilute systems, cyclic dimers were indeed found to be a commonly occurring type of aggregate. At concentrations above 200 mM, close aggregate formation was seen. These findings were expected from literature. However, what was unexpected was that the cyclic trimer was found to be lower in free energy than the cyclic dimer.

Finally, this work described a transition in the distribution of aggregates. At concentrations below 200 mM, it was found that cyclic dimers were more prevalent than cyclic trimers, despite the trimer structure being more energetically favorable. This is because aggregate formation is dependent on the rate of collision between HDBP molecules as they diffuse through the solution, and the relaxation time of newly formed aggregates to arrange itself into low energy structures.

Altogether, these new findings represent a better understanding of the behavior of HDBP. Not only has groundwork been laid to generate more accurate simulations of extractants, novel concepts have been found, and new experimental data has been generated. These insights may be small step forward in better understanding and exploiting aggregation phenomenon to produce more efficient SX schemes.

6.2 Future Works

6.2.1 Relaxation Time of HDBP Aggregates

It has been observed in Chapters 4 and 5 that aggregates form through collisions of HDBP molecules. Each collision gives the opportunity for HB formation to occur, generating larger aggregates as concentration increases. However, it takes time for bonded aggregates to actually assemble into low free energy structures. What influences this relaxation time could potentially give insights into the behavior of other extractants. Understanding these effects may be beneficial for systems utilizing multiple extractants, and perhaps might even affect synergism.

The factors affecting relaxation time are likely not straight forward. HDEHP, which is similar to HDBP, replaces the linear butyl chains with a bulkier ethylhexyl tail. This

would decrease the diffusivity of HDEHP when compared to HDBP. Across the same concentrations, fewer collisions of molecular aggregates per unit time should therefore be expected. However, by the same reasoning, the relaxation time of HDEHP aggregates may increase. Altogether, this makes it unclear how differences in the alkyl-tail bulk would change where the transition between dilute systems and that of close aggregate formation lies.

Two types of simulations are proposed. The first type would attempt to directly measure relaxation time. Unfavorable conformations of HDBP dimers and trimers would be gathered from existing simulations. Unfavorability would be defined by isolating aggregate species, measuring their internal energies, then calculating how many standard deviations away from average each structure is. These structures would then be simulated in solvent by themselves for a short time. HB formation would then be analyzed across numerous short simulations running in parallel.

The second type of simulation would attempt to collide two aggregate species already in favorable conformations into each other. This would be accomplished by imposing via weak harmonic potentials between each aggregate. The intention here is to witness the formation and subsequent relaxation of aggregates as they grow larger.

6.2.2 Electronic Structure Calculations of HDBP Aggregates

In positron annihilation analysis, it is known that positronium response is influenced by the local electronic environment, with some particular effect pronounced by HB[120]. While a transition was described in Chapter 5, it is confirming that relaxation time and positronium formation are related phenomenon.

Proposed calculations would run various energetically favorable or unfavorable

structures of HDBP aggregates into software capable of electronic structure calculations. Favorability would be determined by the same criteria as unfavorability, mentioned previously. Direct calculation of electronic structure and witnessing how it changes with shape may give clues as to how aggregation directly affects positronium response.

6.2.3 X-ray Scattering Experiments of Structures of HDBP

Simulation reaches its highest potential when it can accurately predict behavior in novel systems. To be able to say that a model achieves this to an acceptable degree requires vast amounts of data that it can first be validated against. To that end, small angle x-ray scattering is a useful tool that is already being used to study aggregation phenomenon of extractants[121].

To augment existing simulations, solutions of HDBP in dodecane would be prepared in concentrations of 50 to 1000 mM, which are the same concentrations that were simulated in Chapters 4 and 5. Further, in order to support the previously mentioned work on relaxation time of aggregates, it would be worth running solutions with molecules of every growing tails. Scattering data on this array of solutions varying across concentrations and molecular bulkiness would be collected and compared with existing and future molecular dynamics studies.

6.2.4 Polarizable HDBP Force Field

The end goal of these simulations is to aid in designing more efficient extractants and procedures. To said end, it is important to examine through simulation the interaction of HDBP as it meets the metal loaded aqueous phase. However, as metals are highly polar atoms, such simulations would be wildly inaccurate without using polarizable FFs[53]. It

has been shown in Chapter 3 that the default GAFF parameters required tweaking, and it is likely going to be the case when polarizability is turned on. Therefore, it is important to develop a polarizable model of HDBP. The procedure to do so has already been established in works by peers.

6.2.5 Monte Carlo Models of Aggregation

The lessons learned in the development of simple theoretical models can potentially lead to useful insights for the system at large. Therefore, it may be useful to develop a simple model of aggregation for mono-acids via hydrogen bonding. Monte Carlo methods are commonly used in the study of clusters and their formation. Since such simulations merely fill points on a graph, it is a far cry from the $O(n^2)$ complexity that is molecular dynamics simulation. It is then perhaps worth giving the development of such models some attention. Further, it is already known that the HB networks reverse micelles begin to form is akin to percolation transitions[55].

A rudimentary idea is as follows. Points on a graph are filled with some given filling probability, which will be determined by concentration. Adjacent points may then be considered to be coordinated with each other at some probability. This probability represents the energy behind hydrogen bonding. It is possible that tuning the filling and coordinating probabilities may yield a distribution of clusters that resembles that seen in this dissertation. Potentially, such work might be accomplished by a sufficiently bright undergraduate student.

Bibliography

[1] Sustainable Development Goals. http://www.un.org/sustainabledevelopment/sustainable-development-goals/.

[2] Transforming our world: the 2030 Agenda for Sustainable Development. https://sustainabledevelopment.un.org/post2015/transformingourworld.

[3] Inventory of U.S. Greenhouse Gas Emissions and Sinks. https://www.epa.gov/sites/production/files/2019-04/documents/us-ghg-inventory-2019-main-text.pdf.

[4] Dlugokencky, E.; Hall, B.; Montzka, S.; Dutton, G.; Mühle, J.; Elkins, J. Atmospheric composition [in state of the climate in 2017]. *Bull Am Meteorol Soc* **2018**, *99*, S46–9.

[5] Lüthi, D.; Le Floch, M.; Bereiter, B.; Blunier, T.; Barnola, J.-M.; Siegenthaler, U.; Raynaud, D.; Jouzel, J.; Fischer, H.; Kawamura, K. , et al. High-resolution carbon dioxide concentration record 650,000–800,000 years before present. *Nature* **2008**, *453*, 379.

[6] Collins, M.; Knutti, R.; Arblaster, J.; Dufresne, J.-L.; Fichefet, T.; Friedlingstein, P.; Gao, X.; Gutowski, W. J.; Johns, T.; Krinner, G. , et al. Long-term climate change: projections, commitments and irreversibility. **2013**,

[7] Lindsey, R. Climate Change: Atmospheric Carbon Dioxide. https://www.climate.gov/news-features/understanding-climate/climate-change-atmospheric-carbon-dioxide.

[8] Hoegh-Guldberg, O.; Mumby, P. J.; Hooten, A. J.; Steneck, R. S.; Greenfield, P.; Gomez, E.; Harvell, C. D.; Sale, P. F.; Edwards, A. J.; Caldeira, K. , et al. Coral reefs under rapid climate change and ocean acidification. *science* **2007**, *318*, 1737–1742.

[9] Gaston, K. *Biodiversity : an introduction*; Blackwell Pub: Malden, MA, 2004.

[10] Wei, F. et al. The Value of Ecosystem Services from Giant Panda Reserves. *Current Biology* **2018**, *28*, 2174–2180.e7.

[11] Easterling, D. R.; Evans, J.; Groisman, P. Y.; Karl, T. R.; Kunkel, K. E.; Ambenje, P. Observed variability and trends in extreme climate events: a brief review. *Bulletin of the American Meteorological Society* **2000**, *81*, 417–426.

[12] Meehl, G. A.; Karl, T.; Easterling, D. R.; Changnon, S.; Pielke Jr, R.; Changnon, D.; Evans, J.; Groisman, P. Y.; Knutson, T. R.; Kunkel, K. E. , et al. An introduction to trends in extreme weather and climate events: observations, socioeconomic impacts, terrestrial ecological impacts, and model projections. *Bulletin of the American Meteorological Society* **2000**, *81*, 413–416.

[13] Kovats, R. S.; Hajat, S. Heat stress and public health: a critical review. *Annu. Rev. Public Health* **2008**, *29*, 41–55.

[14] It's so hot in Australia that bats' brains are frying. https://www.washingtonpost.com/news/worldviews/wp/2018/01/09/its-so-hot-in-australia-that-bats-brains-are-frying/?noredirect=on&utm_term=.38be5c526198.

[15] Space heating and water heating account for nearly two thirds of U.S. home energy use. https://www.eia.gov/todayinenergy/detail.php?id=37433.

[16] Kahl, C. H. *States, scarcity, and civil strife in the developing world*; Princeton University Press, 2018.

[17] Salehyan, I. Climate change and conflict: Making sense of disparate findings. *Political Geography* **2014**, *43*, 1 – 5, Special Issue: Climate Change and Conflict.

[18] Hsiang, S. M.; Burke, M.; Miguel, E. Quantifying the Influence of Climate on Human Conflict. *Science* **2013**, *341*.

[19] Reuveny, R. Climate change-induced migration and violent conflict. *Political Geography* **2007**, *26*, 656 – 673, Climate Change and Conflict.

[20] Nett, K.; Rüttinger, L. Insurgency, Terrorism and Organized Crime in a Warming Climate. **2016**,

[21] Report on Effects of a Changing Climate to the Department of Defense. https://climateandsecurity.files.wordpress.com/2019/01/sec_335_ndaa-report_effects_of_a_changing_climate_to_dod.pdf.

[22] *Nuclear Power and Sustainable Development*; International Atomic Energy Agency, 2016.

[23] Conca, J. The 'Deathprint' Of Energy Grapples With The Powers Of Regulation. 2016; https://www.forbes.com/sites/jamesconca/2016/09/30/the-deathprint-of-energy-grapples-with-the-powers-of-regulation/#6aafc1b62c6b.

[24] McBride, J.; Moore, R.; Witherspoon, J.; Blanco, R. Radiological impact of airborne effluents of coal and nuclear plants. *Science* **1978**, *202*, 1045–1050.

[25] Koplitz, S. N.; Jacob, D. J.; Sulprizio, M. P.; Myllyvirta, L.; Reid, C. Burden of disease from rising coal-fired power plant emissions in Southeast Asia. *Environmental science & technology* **2017**, *51*, 1467–1476.

[26] Kharecha, P. A.; Hansen, J. E. Prevented Mortality and Greenhouse Gas Emissions from Historical and Projected Nuclear Power. *Environmental Science & Technology* **2013**, *47*, 4889–4895, PMID: 23495839.

[27] Disposal of High-Level Nuclear Waste. https://www.gao.gov/key_issues/disposal_of_highlevel_nuclear_waste/issue_summary.

[28] Mathur, J. N.; Murali, M. S.; Nash, K. L. ACTINIDE PARTITIONING—A REVIEW. *Solvent Extraction and Ion Exchange* **2001**, *19*, 357–390.

[29] Blue Rubbon Commission on America's Nuclear Future. 2012; https://www.prnewswire.com/news-releases/blue-ribbon-commission-on-americas-nuclear-future-issues-final-report-to-secreta
html.

[30] Baird, M. *Handbook of solvent extraction*; Krieger Pub. Co: Malabar, Fla, 1991.

[31] Choppin, G. *Radiochemistry and nuclear chemistry*; Butterworth-Heinemann: Woburn, MA, 2002.

[32] Mincher, B. J.; Modolo, G.; Mezyk, S. P. The effects of radiation chemistry on solvent extraction: 1. Conditions in acidic solution and a review of TBP radiolysis. *Solvent Extraction and Ion Exchange* **2009**, *27*, 1–25.

[33] Peppard, D.; Ferraro, J.; Mason, G. Hydrogen bonding in organophosphoric acids. *Journal of Inorganic and Nuclear Chemistry* **1958**, *7*, 231–244.

[34] Luo, J.; Wang, C.-Z.; Lan, J.-H.; Wu, Q.-Y.; Zhao, Y.-L.; Chai, Z.-F.; Nie, C.-M.; Shi, W.-Q. Theoretical studies on the AnO_2^{n+} (An = U, Np; n = 1, 2) complexes with di-(2-ethylhexyl)phosphoric acid. *Dalton Trans.* **2015**, *44*, 3227–3236.

[35] Qiao, B.; Demars, T.; Olvera de la Cruz, M.; Ellis, R. J. How hydrogen bonds affect the growth of reverse micelles around coordinating metal ions. *The journal of physical chemistry letters* **2014**, *5*, 1440–1444.

[36] Kolarik, Z. Review: Dissociation, Self-Association, and Partition of Monoacidic Organophosphorus Extractants. *Solvent Extraction and Ion Exchange* **2010**, *28*, 707–763.

[37] Marcus, Y.; Kolarik, Z. The enthalpies of mixing of organophosphate esters with hydrocarbons. *Journal of Solution Chemistry* **1977**, *6*, 39–56.

[38] Dourdain, S.; Hofmeister, I.; Pecheur, O.; Dufreche, J.; Turgis, R.; Leydier, A.; Jestin, J.; Testard, F.; Pellet-Rostaing, S.; Zemb, T. Synergism by coassembly at the origin of ion selectivity in liquid–liquid extraction. *Langmuir* **2012**, *28*, 11319–11328.

[39] Barnes, J. E.; Setchfield, J. H.; Williams, G. Solvent extraction with di (2-ethylhexyl) phosphoric acid; A correlation between selectivity and the structure of the complex. *Journal of Inorganic and Nuclear Chemistry* **1976**, *38*, 1065–1067.

[40] Anderson, T. L.; Braatz, A.; Ellis, R. J.; Antonio, M. R.; Nilsson, M. Synergistic extraction of dysprosium and aggregate formation in solvent extraction systems combining TBP and HDBP. *Solvent Extraction and Ion Exchange* **2013**, *31*, 617–633.

[41] Ellis, R. J.; Anderson, T. L.; Antonio, M. R.; Braatz, A.; Nilsson, M. A SAXS Study of Aggregation in the Synergistic TBP–HDBP Solvent Extraction System. *The Journal of Physical Chemistry B* **2013**, *117*, 5916–5924.

[42] Zilberman, B. Y.; Fedorov, Y. S.; Kopyrin, A. A.; Arkhipov, S. A.; Blazheva, I. V.; Glekov, R. G. *Radiochemistry* **2001**, *43*, 172–176.

[43] Chiarizia, R.; Nash, K. L.; Jensen, M. P.; Thiyagarajan, P.; Littrell, K. C. Application of the Baxter Model for Hard Spheres with Surface Adhesion to SANS Data for the U(VI)-HNO3, TBP-n-Dodecane System. *Langmuir* **2003**, *19*, 9592–9599.

[44] Chiarizia, R.; Jensen, M. P.; Borkowski, M.; Ferraro, J. R.; Thiyagarajan, P.; Littrell, K. C. Third Phase Formation Revisited: The U(VI), HNO3–TBP, n-Dodecane System. *Solvent Extraction and Ion Exchange* **2003**, *21*, 1–27.

[45] Chiarizia, R.; Jensen, M. P.; Rickert, P. G.; Kolarik, Z.; Borkowski, M.; Thiyagarajan, P. Extraction of Zirconium Nitrate by TBP inn-Octane: Influence of Cation Type on Third Phase Formation According to the "Sticky Spheres" Model. *Langmuir* **2004**, *20*, 10798–10808.

[46] Plaue, J.; Gelis, A.; Czerwinski, K.; Thiyagarajan, P.; Chiarizia, R. Small-Angle Neutron Scattering Study of Plutonium Third Phase Formation in 30% TBP/HNO3/Alkane Diluent Systems. *Solvent Extraction and Ion Exchange* **2006**, *24*, 283–298.

[47] Nilsson, M.; Zalupski, P.; Antonio, M. *Ion Exchange and Solvent Extraction: Volume 21, Supramolecular Aspects of Solvent Extraction, 6.4.1 (Ion Exchange and Solvent Extraction Series)*; CRC Press, 2013.

[48] Marcus, Y.; Kolarik, Z. The enthalpies of mixing of organophosphate esters with hydrocarbons. *Journal of Solution Chemistry* **1977**, *6*, 39–56.

[49] Jensen, M. P.; Bond, A. H. Influence of aggregation on the extraction of trivalent lanthanide and actinide cations by purified Cyanex 272, Cyanex 301, and Cyanex 302. *Radiochimica Acta* **2002**, *90*, 205–209.

[50] Mason, G.; Lewey, S.; Peppard, D. Extraction of metallic cations by mono-acidic orthophosphate esters in a monomerizing diluent. *Journal of Inorganic and Nuclear Chemistry* **1964**, *26*, 2271–2284.

[51] Vo, Q. N.; Dang, L. X.; Nilsson, M.; Nguyen, H. D. Quantifying Dimer and Trimer Formation by Tri-n-butyl Phosphates inn-Dodecane: Molecular Dynamics Simulations. *The Journal of Physical Chemistry B* **2016**, *120*, 6985–6994.

[52] Cui, S.; de Almeida, V. F.; Khomami, B. Molecular Dynamics Simulations of Tri-n-butyl-phosphate/n-Dodecane Mixture: Thermophysical Properties and Molecular Structure. *The Journal of Physical Chemistry B* **2014**, *118*, 10750–10760.

[53] Vo, Q. N.; Dang, L. X.; Nguyen, H. D.; Nilsson, M. Microscopic Behaviors of Tri-n-Butyl Phosphate, n-Dodecane, and Their Mixtures at Air/Liquid and Liquid/Liquid Interfaces: An AMBER Polarizable Force Field Study. *The Journal of Physical Chemistry B* **2018**, *123*, 655–665.

[54] Cocalia, V. A.; Gutowski, K. E.; Rogers, R. D. The coordination chemistry of actinides in ionic liquids: A review of experiment and simulation. *Coordination Chemistry Reviews* **2006**, *250*, 755–764.

[55] Servis, M. J.; Tormey, C. A.; Wu, D. T.; Braley, J. C. A Molecular Dynamics Study of Tributyl Phosphate and Diamyl Amyl Phosphonate Self-Aggregation in Dodecane and Octane. *The Journal of Physical Chemistry B* **2016**, *120*, 2796–2806.

[56] Bapat, D. U.; Dalvi, V. H. Molecular Insights into Water Clusters Formed in Tributylphosphate–Di-(2-ethylhexyl) phosphoric Acid Extractant Systems from Experiments and Molecular Dynamics Simulations. *The Journal of Physical Chemistry B* **2019**,

[57] Debye, P. *Polar Molecules*; Dover, 1929.

[58] Jafari, H.; Danaee, I.; Eskandari, H.; RashvandAvei, M. Electrochemical and Theoretical Studies of Adsorption and Corrosion Inhibition of N,N-Bis(2-hydroxyethoxyacetophenone)-2,2-dimethyl-1,2-propanediimine on Low Carbon Steel (API 5L Grade B) in Acidic Solution. *Industrial & Engineering Chemistry Research* **2013**, *52*, 6617–6632.

[59] Dominik, A.; Chapman, W. G.; Kleiner, M.; Sadowski, G. Modeling of Polar Systems with the Perturbed-Chain SAFT Equation of State. Investigation of the Performance of Two Polar Terms. *Industrial & Engineering Chemistry Research* **2005**, *44*, 6928–6938.

[60] Vo, Q. N.; Hawkins, C. A.; Dang, L. X.; Nilsson, M.; Nguyen, H. D. Computational Study of Molecular Structure and Self-Association of Tri-n-butyl Phosphates inn-Dodecane. *The Journal of Physical Chemistry B* **2015**, *119*, 1588–1597.

[61] Dang, L. X.; Chang, T.-M. Molecular dynamics study of water clusters, liquid, and liquid–vapor interface of water with many-body potentials. *The Journal of Chemical Physics* **1997**, *106*, 8149–8159.

[62] Beard, C. I.; Dailey, B. P. The Structure and Dipole Moment of Isothiocyanic Acid. *The Journal of Chemical Physics* **1950**, *18*, 1437–1441.

[63] Boese, D.; Kremer, F. Molecular dynamics in bulk cis-polyisoprene as studied by dielectric spectroscopy. *Macromolecules* **1990**, *23*, 829–835.

[64] Renuka, C.; Shivashankar, K.; Boregowda, P.; Bellad, S.; Muregendrappa, M.; Nadaf, Y. An experimental and computational study of 2-(3-Oxo-3H-benzo [f] chromen-1-ylmethoxy)-benzoic acid methyl ester. *Journal of Solution Chemistry* **2017**, *46*, 1535–1555.

[65] Gilani, A. G.; Mamaghani, M.; Anbir, L. Dipole moments and intermolecular association of some carbonyl compounds in nonpolar solvents. *Journal of solution chemistry* **2003**, *32*, 625–636.

[66] Gilani, A. G.; Ranjkesh, A.; Beevers, M. Dipole moments of flourobenzene and its mesogenic derivative in 1, 4-dioxane and 1-butanol solutions. *Journal of solution chemistry* **2009**, *38*, 557–570.

[67] Guggenheim, E. A. A proposed simplification in the procedure for computing electric dipole moments. *Transactions of the Faraday Society* **1949**, *45*, 714.

[68] Janini, G. M.; Katrib, A. H. Determination of the dipole moment of polar compounds in nonpolar solvents. *Journal of Chemical Education* **1983**, *60*, 1087.

[69] Buckingham, A. D. Electric dipole moments of solutes in non-polar solvents. *Transactions of the Faraday Society* **1956**, *52*, 1551.

[70] McClellan, A. L. *Tables of Experimental Dipole Moments*; W. H. Freeman and Company, 1963.

[71] Yaws, C. L. *Yaws' Thermophysical Properties of Chemicals and Hydrocarbons*; Knovel, 2009.

[72] Petkovic, D. M.; Kezele, B.; Rajic, D. Dipole moments of some neutral organic phosphates. *The Journal of Physical Chemistry* **1973**, *77*, 922–924.

[73] Anderson, J.; Berthod, A.; Estévez, V. P.; Stalcup, A. *Analytical separation science*; Wiley-VCH Verlag GmbH & Co. KGaA., 2014.

[74] Valantina, S. R.; Angeline, D. P.; Uma, S.; Prakash, B. J. Estimation of dielectric constant of oil solution in the quality analysis of heated vegetable oil. *Journal of Molecular Liquids* **2017**, *238*, 136–144.

[75] Frisch, M. J. et al. Gaussian 09, Revision B.01. 2009.

[76] Weininger, D. SMILES, a chemical language and information system. 1. Introduction to methodology and encoding rules. *Journal of chemical information and computer sciences* **1988**, *28*, 31–36.

[77] Case, D. A. et al. Amber 14. University of California, San Francisco, 2014.

[78] Radzicka, A.; Wolfenden, R. Comparing the polarities of the amino acids: side-chain distribution coefficients between the vapor phase, cyclohexane, 1-octanol, and neutral aqueous solution. *Biochemistry* **1988**, *27*, 1664–1670.

[79] Lanham, W.; Runion, T. Purex process for uranium and plutonium recovery. *ORNL-479* **1949**,

[80] Herbst, R.; Baron, P.; Nilsson, M. *Advanced separation techniques for nuclear fuel reprocessing and radioactive waste treatment*; Elsevier, 2011; pp 141–175.

[81] Yoo, T. The dipole moments paper. *Journal of Engineering and Imaginary Papers* **2017**, *20*, 3446–3452.

[82] Etzler, F. M.; Conners, J. J. A DSC/TGA method for determination of the heat of vaporization. *Thermochimica Acta* **1991**, *189*, 185–192.

[83] Skene, W. G.; Krzymien, M. E. Vapor Pressure of Tri-n-butyl Phosphate. *Journal of Chemical & Engineering Data* **1995**, *40*, 394–397.

[84] Chernyak, Y. Dielectric Constant, Dipole Moment, and Solubility Parameters of Some Cyclic Acid Esters. *Journal of Chemical & Engineering Data* **2006**, *51*, 416–418.

[85] Barton, A. F. *CRC Handbook of Solubility Parameters and Other Cohesion Parameters, Second Edition*; CRC Press, 1991.

[86] Lumetta, G. J.; Levitskaia, T. G.; Latesky, S. L.; Henderson, R. V.; Edwards, E. A.; Braley, J. C.; Sinkov, S. I. Lipophilic ternary complexes in liquid–liquid extraction of trivalent lanthanides. *Journal of Coordination Chemistry* **2012**, *65*, 741–753.

[87] Dang, L. X. Intermolecular interactions of liquid dichloromethane and equilibrium properties of liquid–vapor and liquid–liquid interfaces: A molecular dynamics study. *The Journal of Chemical Physics* **1999**, *110*, 10113–10122.

[88] Maginn, E. J. Atomistic Simulation of the Thermodynamic and Transport Properties of Ionic Liquids. *Accounts of Chemical Research* **2007**, *40*, 1200–1207.

[89] Sprenger, K. G.; Jaeger, V. W.; Pfaendtner, J. The General AMBER Force Field (GAFF) Can Accurately Predict Thermodynamic and Transport Properties of Many Ionic Liquids. *The Journal of Physical Chemistry B* **2015**, *119*, 5882–5895.

[90] Asfin, R.; Denisov, G.; Poplevchenkov, D.; Tokhadze, K.; Velikanova, T. IR ν (OH) Band and Dimerization of Phosphorus Acids in the Gas Phase and Solid State. *Polish Journal of Chemistry* **2002**, *76*, 1223–1232.

[91] Tokhadze, K.; Denisov, G.; Wierzejewska, M.; Drozd, M. First example of the ABC ν (OH) absorption structure for both gaseous and crystalline phase: infrared studies of dimethylphosphinic acid. *Journal of molecular structure* **1997**, *404*, 55–62.

[92] Asfin, R.; Denisov, G.; Tokhadze, K. The ν(OH/OD) band shape of strong hydrogen bonded dimers of phosphinic acids. Phenomenology and formation models. *Journal of Molecular Structure* **2006**, *790*, 11–17.

[93] S.E. Stein, D. *Infrared Spectra*; NIST Mass Spec Data Center, (Retrieved 26/12/2016).

[94] Gray, M. F.; Zalupski, P.; Nilsson, M. Determination of Activity Coefficients of di-(2-ethylhexyl) Phosphoric Acid Dimer in Select Organic Solvents Using Vapor Phase Osmometry. *Solvent Extraction and Ion Exchange* **2013**, *31*, 550–563.

[95] Pochylski, M.; Rossi, C. O.; Nicotera, I.; Liveri, V. T.; Calandra, P. Nano-demixing as a novel strategy for magnetic field responsive systems: the case of dibutyl phosphate/bis (2-ethylhexyl) amine systems. *RSC Advances* **2016**, *6*, 26696–26708.

[96] Götz, A. W.; Williamson, M. J.; Xu, D.; Poole, D.; Le Grand, S.; Walker, R. C. Routine Microsecond Molecular Dynamics Simulations with AMBER on GPUs. 1. Generalized Born. *Journal of Chemical Theory and Computation* **2012**, *8*, 1542–1555, the first pmemdcuda paper.

[97] Salomon-Ferrer, R.; Götz, A. W.; Poole, D.; Le Grand, S.; Walker, R. C. Routine Microsecond Molecular Dynamics Simulations with AMBER on GPUs. 2. Explicit Solvent Particle Mesh Ewald. *Journal of Chemical Theory and Computation* **2013**, *9*, 3878–3888, Second gfx paper.

[98] Martínez, L.; Andrade, R.; Birgin, E. G.; Martínez, J. M. PACKMOL: A package for building initial configurations for molecular dynamics simulations. *Journal of Computational Chemistry* **2009**, *30*, 2157–2164.

[99] Humphrey, W.; Dalke, A.; Schulten, K. VMD – Visual Molecular Dynamics. *Journal of Molecular Graphics* **1996**, *14*, 33–38.

[100] Roe, D. R.; Cheatham, T. E. PTRAJ and CPPTRAJ: Software for Processing and Analysis of Molecular Dynamics Trajectory Data. *Journal of Chemical Theory and Computation* **2013**, *9*, 3084–3095.

[101] Nguyen, H.; Roe, D. R.; Swails, J.; Case, D. A. PYTRAJ: Interactive data analysis for molecular dynamics simulations. **2016**,

[102] Shirts, M. R.; Chodera, J. D. Statistically optimal analysis of samples from multiple equilibrium states. *The Journal of Chemical Physics* **2008**, *129*, 124105.

[103] Chodera, J. D. A Simple Method for Automated Equilibration Detection in Molecular Simulations. *Journal of Chemical Theory and Computation* **2016**, *12*, 1799–1805.

[104] Jones, E.; Oliphant, T.; Peterson, P. , et al. SciPy: Open source scientific tools for Python. 2001–; `http://www.scipy.org/`.

[105] Hunter, J. D. Matplotlib: A 2D graphics environment. *Computing In Science & Engineering* **2007**, *9*, 90–95.

[106] Hanwell, M. D.; Curtis, D. E.; Lonie, D. C.; Vandermeersch, T.; Zurek, E.; Hutchison, G. R. Avogadro: an advanced semantic chemical editor, visualization, and analysis platform. *Journal of Cheminformatics* **2012**, *4*, 17.

[107] Wang, J.; Wang, W.; Kollman, P. A.; Case, D. A. Automatic atom type and bond type perception in molecular mechanical calculations. *Journal of Molecular Graphics and Modelling* **2006**, *25*, 247–260.

[108] Jakalian, A.; Bush, B. L.; Jack, D. B.; Bayly, C. I. Fast, efficient generation of high-quality atomic charges. AM1-BCC model: I. Method. *Journal of Computational Chemistry* **2000**, *21*, 132–146.

[109] Jakalian, A.; Jack, D. B.; Bayly, C. I. Fast, efficient generation of high-quality atomic charges. AM1-BCC model: II. Parameterization and validation. *Journal of Computational Chemistry* **2002**, *23*, 1623–1641.

[110] Wang, J.; Wolf, R. M.; Caldwell, J. W.; Kollman, P. A.; Case, D. A. Development and testing of a general amber force field. *Journal of Computational Chemistry* **2004**, *25*, 1157–1174.

[111] Vetterling, W. T.; Teukolsky, S. A.; Press, W. H.; Flannery, B. P. *Numerical recipes: the art of scientific computing.*; Cambridge university press Cambridge, 1992; Vol. 2.

[112] Swalis, J. Re: [AMBER] Tutorial B0. 2015; `http://archive.ambermd.org/201503/0162.html`.

[113] Tessier, M. [Amber] HO atom type van der Waals (GLYCAM). 2011; `http://archive.ambermd.org/201110/0119.html`.

[114] Zhang, Y.; Maginn, E. J. A simple AIMD approach to derive atomic charges for condensed phase simulation of ionic liquids. *The Journal of Physical Chemistry B* **2012**, *116*, 10036–10048.

[115] Yoo, T.; Nguyen, H.; Nilsson, M. Determinations of Dipole Moments for Liquid–Liquid Extraction Reagents. *Journal of Solution Chemistry* **2018**, *47*, 1214–1223.

[116] Tessier, M. [AMBER] HO atom type van der Waals (GLYCAM). 2011; `http://archive.ambermd.org/201110/0119.html`.

[117] Ganguly, B. N.; Sen, P. Study of aggregation behaviour in HDEHP—n-heptane system by positron annihilation technique. *International Journal of Radiation Applications and Instrumentation. Part A. Applied Radiation and Isotopes* **1987**, *38*, 681–684.

[118] Yoo, T.; Nguyen, H. D.; Nilsson, M. Molecular Dynamics Investigations of Dibutylphosphoric Acid—Parameterization and Dimerization. *The Journal of Physical Chemistry B* **2018**, *122*, 12040–12048, PMID: 30431277.

[119] Qiao, B.; Demars, T.; Olvera de la Cruz, M.; Ellis, R. J. How hydrogen bonds affect the growth of reverse micelles around coordinating metal ions. *The journal of physical chemistry letters* **2014**, *5*, 1440–1444.

[120] Jean, Y.-C.; Ache, H. J. Study of the micelle formation and the effect of additives on this process in reversed micellar systems by positron annihilation techniques. *Journal of the American Chemical Society* **1978**, *100*, 6320–6327.

[121] Antonio, M. R.; Chiarizia, R.; Gannaz, B.; Berthon, L.; Zorz, N.; Hill, C.; Cote, G. Aggregation in Solvent Extraction Systems Containing a Malonamide, a Dialkylphosphoric Acid and their Mixtures. *Separation Science and Technology* **2008**, *43*, 2572–2605.

Appendix A

Appendix

A.1 Supporting Information for Chapter 3

The bulk HDBP simulations, discussed in Section 3.3.1. were further analyzed for lifetime of the hydrogen bonds. Any free OH that was captured within a simulation frame should be considered transient. However, their behavior is vastly different across the default FF and the optimized FF. Table A.1 shows the average lifetime of free OH in the bulk. Immediately apparent is the massive uncertainty associated with lifetimes in the default FF. The uncertainty was taken to be the standard deviation of the distribution of lifetimes. As such, it is representative of a wide distribution. In Figure A.1A, a lifetime of zero counts the number of OH which have never been free across the entirety of the 20 ns sampling stage. On the opposite end, many others remain free on an order of whole nanoseconds. These lifetimes are well beyond the scale of the plot. Given the crowded nature of pure solution, neither of these situations should be considered realistic. Entropy would favor a more constant exchange of hydrogen bonding partners. It is likely that the overstated hydrogen bond energy by GAFF greatly dampens this effect. The

optimized FF is better behaved in this regard. From Figure A.1B, it is shown that the distribution of lifetimes is far tighter. Overly stable bonds and chronically free OH are notably missing. Lifetimes greater than 40 ps were not observed, and all hydrogen bonds were engaged in exchange. This is a much more physical picture of the close hydrogen bonding environment.

In Figure A.2, the difference in the distribution of D-A angles and distances between the simulation of pure HDBP and the PMF (representing a dilute system) are compared. Figure A.2A represents the distribution from the bulk of pure HDBP as taken from previous discussion in Section 3.3.2. Figure A.2B is the same as Figure 3.7. From these plots, it is seen that the hydrogen bonding angles are shallower in the bulk, while the distance still remains within the narrow band of around 2.5 - 3.25 Å. It is sensible as the distance would not change, as the hydrogen bond distance is given predominately by the Lennard-Jones term of the FF. The difference in angles can be attributed to the different kinds of bonds which form in the bulk. Tracking hydrogen bonds in the sampling stage trajectory shows that 4.4 ± 0.6% of HDBP molecules are in a cyclic conformation. This should be expected in the bulk. The close proximity of other HDBP molecules increases the chance that both donor and acceptor sites of each HDBP are occupied. Further, it is likelier that OH atoms can find a straighter, and therefore more energetically favorable, hydrogen bond. As discussed previously, the hydrogen bond interaction is strong. It then follows that the PMF, which represents the dilute case, would prefer the cyclic dimer. This is exactly because the free energy landscape is built around preserving the two hydrogen bonds necessary to make the cyclic dimer. The bulk does not have to worry about keeping OH atoms hydrogen bonded due to the abundance nearby donors and acceptors. This means the system has the energetic freedom to adopt more favorable angles.

	average free OH per simulation frame (%)	average free OH lifetime (ps)
default + H_o	3.9 ± 0.9	88.4 ± 1000
optimized	4.6 ± 1.1	16.8 ± 4.0

Table A.1: Free OH Population in Bulk HDBP at 300 K

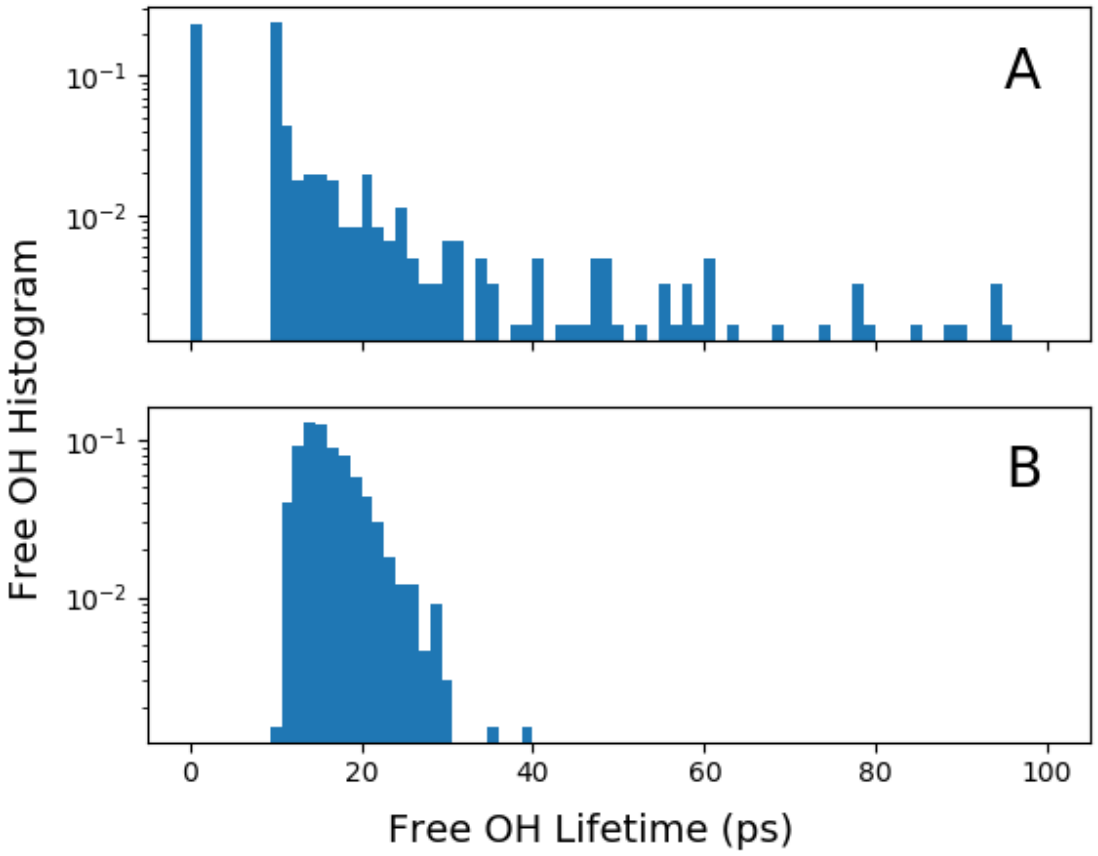

Figure A.1: Shown are histograms of the lifetimes of free OH in bulk phase simulations on a logarithmic scale. A lifetime of zero indicates hydrogen bonds that have remained stable throughout the entire sampling period. Plot A represents the default FF, and B the optimized FF. The distribution of Plot A extends greatly beyond the given scale. This is untrue for Plot B.

A.2 TBP and HDBP Mixtures

Some processes will utilize multiple extractants as opposed to one. This combination often results in greater extractive power than either single extractant working alone. This

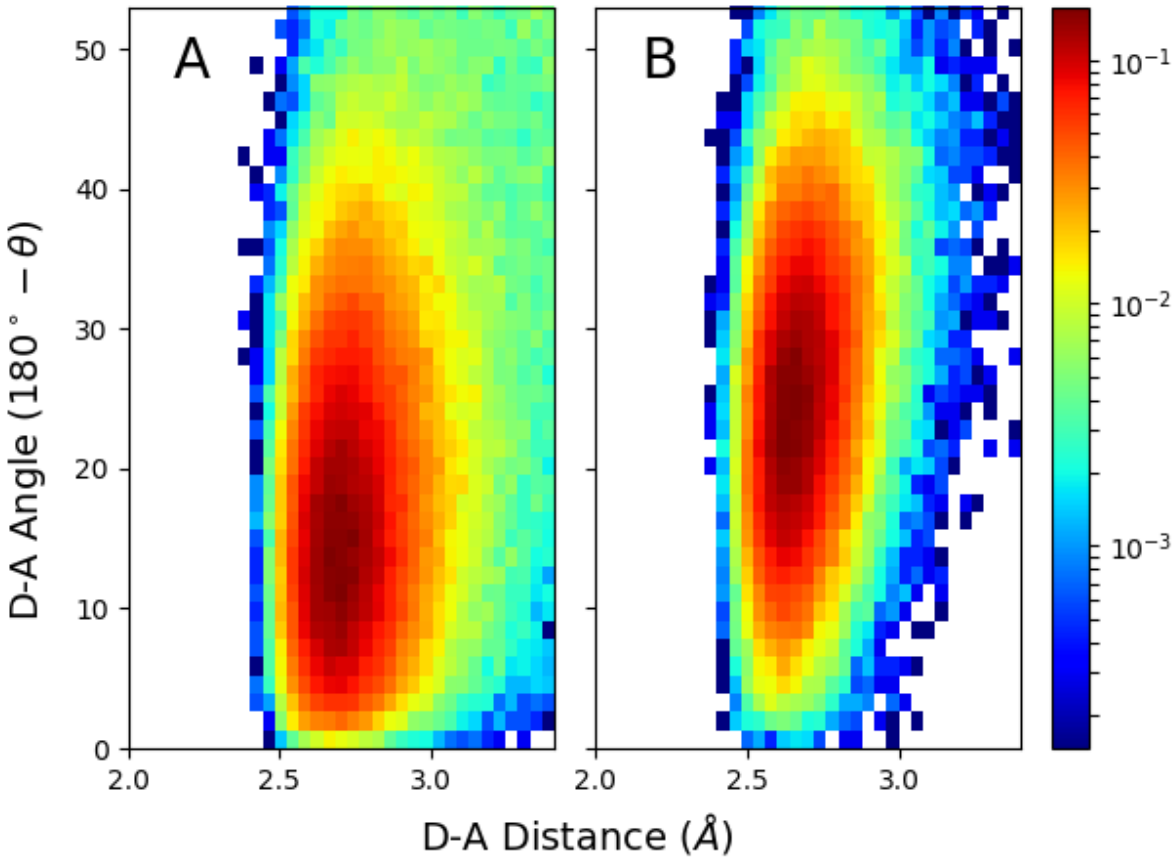

Figure A.2: Plots A and B are two dimensional histograms of the D-A angle and distance. Plot A shows this distribution in the pure HDBP simulations. Plot B shows this for the lowest 0-3 kcal/mol free energy region of the PMF, and was taken directly from the calculated PMF.

possibility of synergism makes mixtures of TBP and HDBP interesting systems to study. Included are the preliminary results of these simulations. Simulation procedure followed that of previous sets. The total concentration of extractant was held constant at 1 M. Their total number in simulation was 100 molecules. The ratio of HDBP to TBP molecules was altered in incriments of 25 molecules, spanning from pure HDBP to pure TBP. These simulations sets emulate existing scattering data taken from Anderson et. al. [40]

Figure A.3 shows preliminary data regarding the radial distribution function of HDBP and TBP mixtures. The overall profile of these curves matches that found through

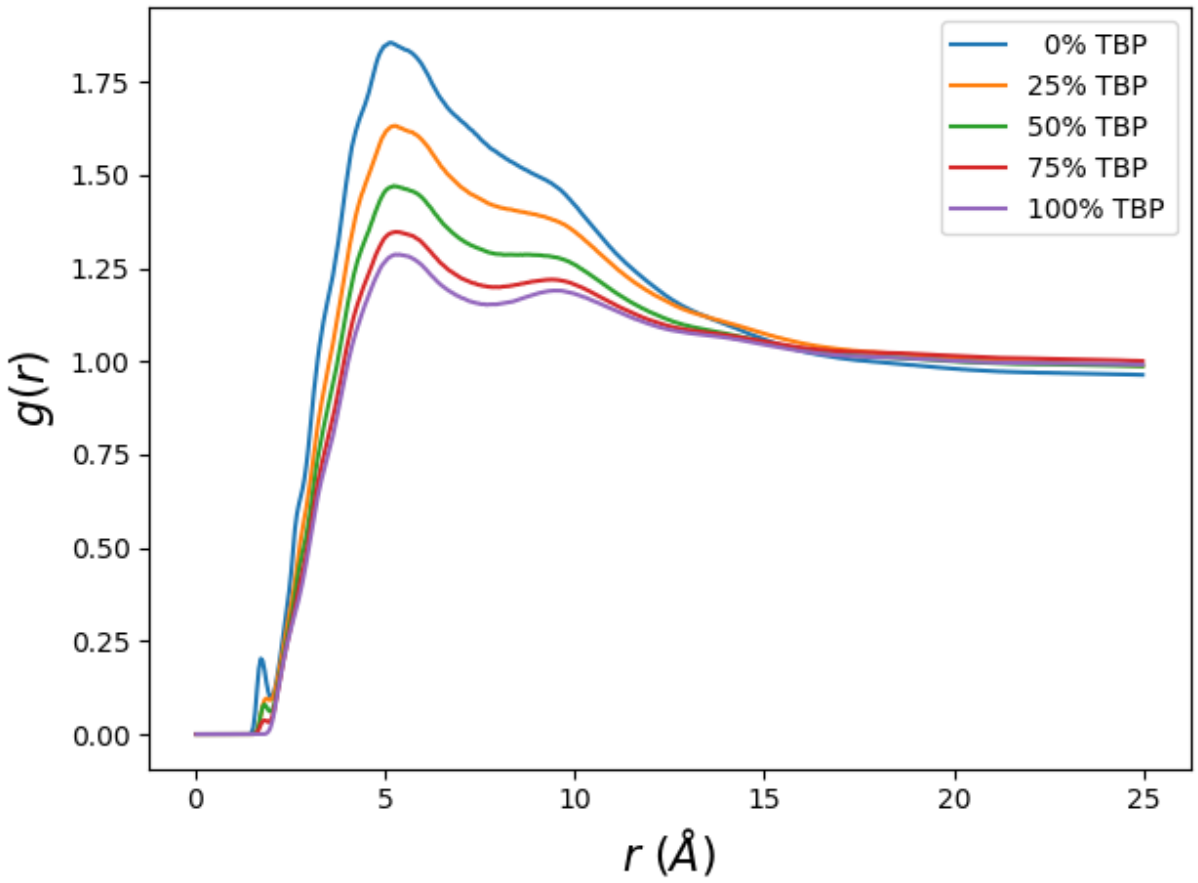

Figure A.3: This particular RDF can be likened to that which would be calculated from scattering experiments. The first minor peak represents oxygens around hydrogen bonds. The following peaks represents the distribution of atoms.

scattering experiments.

Figure A.4 shows the RDF of just the phosphorus atoms, giving a better understanding of the distribution of molecules in solution. The overall height of the peaks decrease with increasing TBP. This shows that the formation of close aggregates is actually diminished. The addition of TBP, which has only a single acceptor, totally extinguishes the cyclid HDBP peak. This may be due to the fact that TBP molecules will cap HDBP chains, prohibiting further growth.

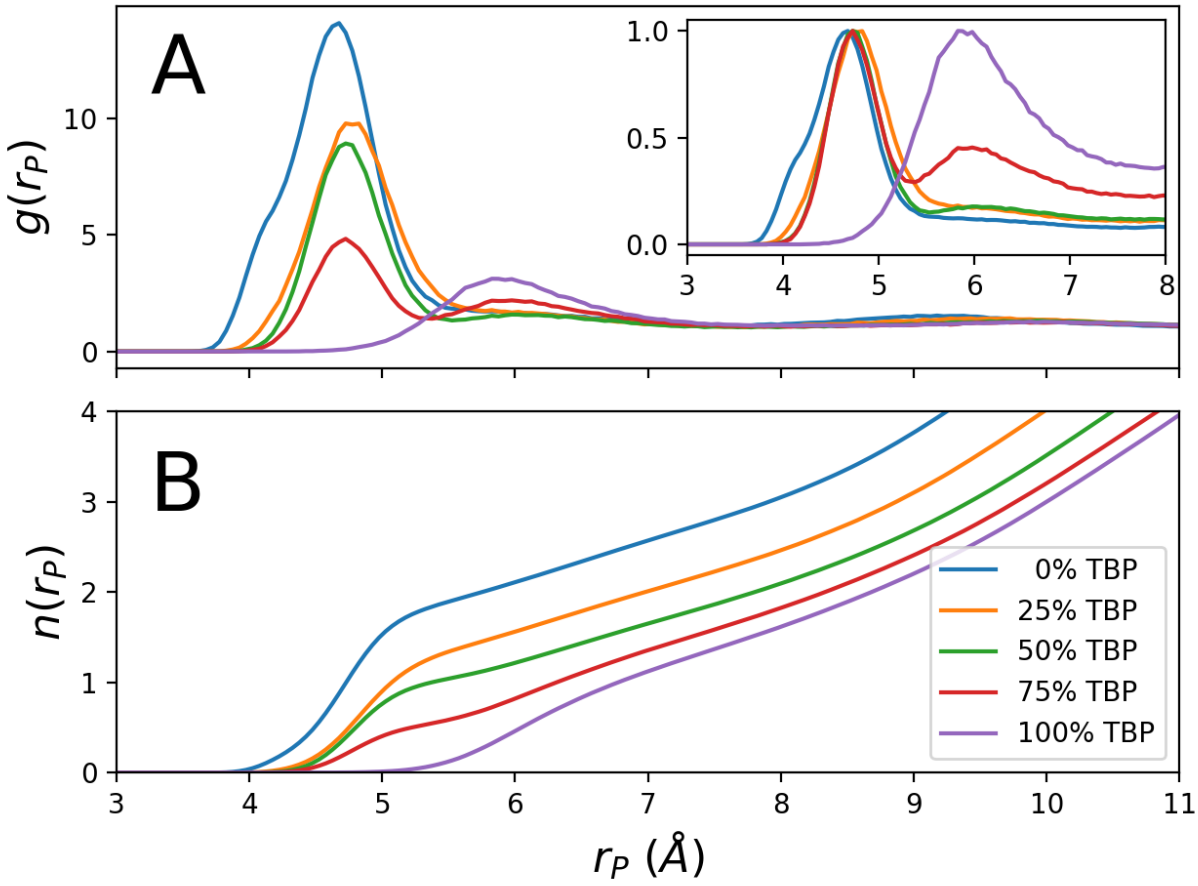

Figure A.4: A shows the RDF of the TBP:HDBP system across different ratios. The inset shows this same data normalized across peaks. The left most shoulder is the cyclic head-to-tail dimer of HDBP. Addition of TBP completely extinguishes this peak. The same is true for the peak at 4.7 Å, which corresponds to closely HB aggregates. B shows the coordination as calculated by integrating the RDF.